Examining Non-Linearities with Screened Fifth Forces

By Ben Thrussell

Thesis submitted to the University of Nottingham
for the degree of Doctor of Philosophy

August 2021

Abstract

Alternative theories of gravity often feature new degrees of freedom in addition to those of the metric tensor that are present in general relativity. One such class of alternative gravitational theories are scalar–tensor theories, which generally predict the existence of a 'fifth force' mediated by a scalar field through a non-minimal coupling to gravity. Such forces are constrained both by laboratory experiments and by observations of our solar system, but 'screening' mechanisms weaken these constraints by suppressing the fifth force in the presence of a high matter density, allowing the dynamics of the scalar field to be relevant on cosmological scales but invisible to our most sensitive experiments.

Nevertheless, many experimental and observational methods for testing screened fifth forces have been proposed. To fully understand their prospects for detecting or constraining new scalar fields, one must ensure that the behaviour of these fields is accurately represented by any approximations that are made in the process of calculating observables. Contributions to this behaviour may include non-linearities in the scalar field's bare potential, the non-minimal coupling between the field and its own stress–energy, and quantum corrections. This thesis will study all three of these effects, both in isolation and in the context of two important scenarios, for two types of screening: the symmetron, in which the strength of the scalar field's coupling to matter varies with the background matter density, and the chameleon, in which it is the Compton wavelength of the scalar field that varies.

The first scenario is black hole superradiance, an astrophysical phenomenon that can be used to probe any bosonic field through the universality of the gravitational interaction. It will be shown that non-linearities are important for screened scalar fields undergoing a superradiant instability, but that previous studies on axion-like particles are not entirely relevant for symmetrons and chameleons; namely, no 'bosenova' is expected to occur for these models.

The second scenario is that of static field profiles around spherical and cylindrical sources, with particular focus being on the limit in which these sources are point-like compared to the field's Compton wavelength. Scaling relationships for the field profiles are obtained, and screening factors are calculated which show that the symmetron model is well approximated by conventional analytical approximations, while a similar chameleon model requires numerical methods to obtain accurate results.

Contents

1 Introduction

For more than one hundred years, the paradigmatic description of gravity has been that of Einstein's general theory of relativity ('general relativity'). In this paradigm, gravity is inertial motion in curved spacetime, the geometry of which is encoded in the metric tensor $g_{\mu\nu}$, and the metric is influenced by the distribution of energy, momentum, and stress of all other ('matter') fields, which are packaged into the stress–energy tensor $T_{\mu\nu}$.

General relativity is the theory in which the coupling between $g_{\mu\nu}$ and the matter fields is in accordance with the Einstein–Hilbert action and the Einstein field equations. With a mostly-plus metric signature (such that the Minkowski metric is $\mathrm{diag}(-1, +1, +1, +1)$) and natural units ($\hbar$, $c = 1$), these are respectively

$$S = \int d^4x \sqrt{-g} \left(\frac{M_\mathrm{P}^2}{2} R + \mathcal{L}_\mathrm{m} \right), \qquad G_{\mu\nu} := R_{\mu\nu} - \frac{1}{2} R g_{\mu\nu} = M_\mathrm{P}^{-2} T_{\mu\nu} \; . \quad (1.1)$$

Here g is the determinant of $g_{\mu\nu}$. The Ricci tensor $R_{\mu\nu} = R_{\mu\sigma\nu}{}^\sigma$ and Ricci scalar $R = g^{\mu\nu} R_{\mu\nu}$ are also obtained from $g_{\mu\nu}$, and its derivatives up to second order, via the Riemann tensor $R_{\mu\nu\sigma\rho}$, itself defined through the commutator of covariant derivatives ∇_μ such that

$$R_{\mu\nu\sigma}{}^\rho w_\rho = [\nabla_\mu, \nabla_\nu] w_\sigma \quad (1.2)$$

for any w_μ [1]. The Ricci tensor and Ricci scalar terms in the field equations can be added together to make the Einstein tensor $G_{\mu\nu}$. $M_\mathrm{P} \approx 2.435 \times 10^{27}$ eV is the reduced Planck mass, such that Newton's gravitational constant $G = 1/8\pi M_\mathrm{P}^2$. Finally, $\mathcal{L}_\mathrm{m}$ is the Lagrangian of the matter fields such that the stress–energy tensor is given by

$$T_{\mu\nu} = \frac{-2}{\sqrt{-g}} \frac{\partial \sqrt{-g} \mathcal{L}_\mathrm{m}}{\partial g^{\mu\nu}} \; . \quad (1.3)$$

One can also add a cosmological constant, as a constant term in the action and a term proportional to $g_{\mu\nu}$ in the equation of motion, but as this is equivalent to a constant term in the matter Lagrangian we will not include it in the gravitational part of the action here.

To introduce this thesis, I shall first explain why we study alternative theories of gravity, in particular ones that have additional fields beyond $g_{\mu\nu}$ (Section 1.1), then describe how such theories generally result in matter

feeling additional gravitational forces (Section 1.2) and how experimental and observational bounds that apply to the most simplistic theories may in reality be avoided through 'screening' (Section 1.3). Finally, I will give an overview of tests that target screening models (Section 1.4).

1.1 New degrees of freedom

Despite successfully describing gravity in laboratory and solar-system tests[1] [2], general relativity has limitations. Fundamentally, it is a classical theory whereas $T_{\mu\nu}$ is in reality sourced by quantum matter. But even on a classical level, cosmology tells us that Eq. (1.1) with known sources of $T_{\mu\nu}$ is insufficient to explain all observations [3]: there also need to exist new degrees of freedom which source gravitational forces in the manner of pressureless dark matter [3, 4], and furthermore explanations are required for the accelerated expansion of our universe both in the present day as dark energy [5] and possibly in the early universe as inflation [6].

To be accurate, as it is the combination of the general theory of relativity with the Standard Model of particle physics that is insufficient to explain cosmological observations, *a priori* either one individually (or both) may be in error. However, the distinction is less important than might initially seem: although at first glance, the addition of new degrees of freedom amounts only to adding new terms to $\mathcal{L}_{\mathrm{m}}$ and sources of $T_{\mu\nu}$ beyond those presently contained within the Standard Model, Lovelock's theorem [7, 8] provides us with an argument that new degrees of freedom are also a fairly general feature of modified theories of gravity.

The argument [7, 9] is that if a theory is described by a local action $S = \int d^4x \sqrt{-g}\mathcal{L}(g_{\mu\nu})$ with a Lorentz scalar density $\mathcal{L}(g_{\mu\nu})$ then the classical equations of motion obtained by extremising the action with respect to $g_{\mu\nu}$ are $E^{\mu\nu} = 0$ for some tensor $E^{\mu\nu}$. Then Lovelock's theorem itself states that, in four spacetime dimensions, the only choices for a divergence-free $E^{\mu\nu}$ that depend only on the metric and its first two derivatives have the form $E^{\mu\nu} = aG^{\mu\nu} + bg^{\mu\nu}$ for constants a, b [8], so the equations of motion are the Einstein field equations with a cosmological constant. For any theory of $g_{\mu\nu}$ to have different equations of motion, as long as it is described by a local action in four spacetime dimensions and its equations of motion are no

---

[1]Examples that are particularly relevant to the topic of this thesis will be brought up in Sections 1.3 and 1.4.

more than second order in derivatives, it must therefore contain additional degrees of freedom [9].

The simplest choice for a model with at least one new degree of freedom is to add a single scalar field φ to the universe. Ignoring couplings to other fields (besides a minimal coupling to the metric), the very simplest choice would be for said field to obey an equation of motion that is linear in φ, whose only free parameter is the mass μ_φ, such that the action and equation of motion are respectively

$$S = \int d^4x \sqrt{-g} \left(-\frac{1}{2} g^{\mu\nu} \nabla_\mu \varphi \nabla_\nu \varphi - \frac{1}{2} \mu_\varphi^2 \varphi^2 \right), \qquad \Box \varphi = \mu_\varphi^2 \varphi \qquad (1.4)$$

where $\Box := g^{\mu\nu} \nabla_\mu \nabla_\nu$. As the equation of motion is linear, it is easy to compute observables with this model to obtain experimental and observational constraints. However, we cannot expect that new physics will be this simple in reality. There are a few features that even a single scalar field could have which would take its description beyond Eq. (1.4):

- A more complicated kinetic structure, that is to say an action where $\nabla \varphi$ appears in terms other than the canonical kinetic term $\frac{1}{2}(\nabla\varphi)^2$ [5]. These theories are not the subject of this thesis.

- Non-linearities from the potential, that is to say an action where the terms *not* containing $\nabla\varphi$ have higher powers of φ than $\frac{1}{2}\mu_\varphi^2\varphi^2$. Indeed, the only known fundamental scalar field, the Higgs, is non-linear in this manner [10–12]. Nonlinear scalar field theories are often invoked in order to explain dark matter [4,13], dark energy [5], and inflation [6].

- When the scalar field is non-linear, quantum corrections will further change its dynamics from that of the classical equation of motion. These will be discussed in Section 2.2.

- Couplings to other fields. This thesis will consider theories in which the scalar field is non-minimally coupled to gravity through changing the gravitational term R in the Einstein–Hilbert action into $A^2(\varphi)R$ for some function $A(\varphi)$, in effect making the Planck scale field-dependent as $M_\mathrm{P} \to A(\varphi)M_\mathrm{P}$. Such couplings are to be expected if they are not forbidden by some symmetry.

The aim of this thesis is ultimately to consider a class of scalar field theories that are somewhat more complicated than Eq. (1.4), to determine under what conditions Eq. (1.4) provides a suitable approximation for deriving experimental and observational constraints on new degrees of freedom, and to examine some consequences that arise when this linear approximation proves to be too simplistic.

The models of scalar fields that we will study here are ones which display some consequences of non-minimal couplings to gravity and non-linear equations of motion that are already well understood, namely fifth forces and the 'screening' of fifth forces. The remainder of the introduction to this thesis will provide an overview of these phenomena, models which experience them, and their implications for searches for new degrees of freedom.

1.2 Scalar fields and fifth forces

A non-minimal coupling to gravity of the form $A^2(\varphi)R$ is equivalent to a coupling to matter. In order to see how this works, we shall begin by looking at two actions with which we might describe a canonically normalised real scalar field and how they are transformed into each other.

Firstly, there is the action in the Jordan frame, in which the scalar field can be non-minimally coupled to the metric through the $A^2(\varphi)R$ term.

$$S = \int d^4x \sqrt{-g}\mathcal{L}_\varphi, \qquad \mathcal{L}_\varphi = \frac{M_{\rm P}^2}{2}A^2(\varphi)R - \frac{1}{2}g^{\mu\nu}\nabla_\mu\varphi\nabla_\nu\varphi - V(\varphi) \quad (1.5)$$

Secondly, there is the action in the Einstein frame, which is defined such that the scalar field is minimally coupled to the metric.

$$S = \int d^4x \sqrt{-\tilde{g}}\mathcal{L}_\phi, \qquad \mathcal{L}_\phi = \frac{M_{\rm P}^2}{2}\tilde{R} - \frac{1}{2}\tilde{g}^{\mu\nu}\tilde{\nabla}_\mu\phi\tilde{\nabla}_\nu\phi - \tilde{V}(\phi) \qquad (1.6)$$

The Einstein-frame and Jordan-frame metrics are to be related through a local rescaling $\tilde{g}_{\mu\nu} = A^2 g_{\mu\nu}$, and other tilded quantities and operators are defined using $\tilde{g}_{\mu\nu}{}^2$; the relationship between φ and ϕ will be explored in Section 2.1.

---

[2]Usually this is a straightforward matter of performing the calculations described after Eq. (1.1) up to Eq. (1.3) with $\tilde{g}_{\mu\nu}$ instead of $g_{\mu\nu}$. For the potential, the relationship is $\tilde{V} = \sqrt{g/\tilde{g}}V$.

Note that the relationship $\tilde{g}_{\mu\nu} = A^2 g_{\mu\nu}$ requires $A(\varphi) \neq 0$ everywhere, as if A were to vanish then the mapping between the two frames would not be invertible. This requirement is illustrated by the fact that many of the calculations that follow, both here and in Sec. 2, will include factors of A^{-1}.

The Weyl transformation $g_{\mu\nu} \to \tilde{g}_{\mu\nu} = A^2 g_{\mu\nu}$ gives [1]

$$\sqrt{-\tilde{g}} = A^4 \sqrt{-g} \tag{1.7a}$$

$$\tilde{R} = A^{-2} \left(R - 6g^{\mu\nu} \nabla_\mu \nabla_\nu \ln A - 6g^{\mu\nu} \nabla_\mu \ln A \nabla_\nu \ln A \right) . \tag{1.7b}$$

$\sqrt{-\tilde{g}}\tilde{R}$ in the Einstein frame outputs the term $\sqrt{-g}A^2 R$ in the Jordan frame as necessary to equate Eqs. (1.5) and (1.6).

A direct coupling to matter is then apparent when we introduce the matter part of the action, $\int d^4x \sqrt{-g} \mathcal{L}_{\mathrm{m}}$, which in the $\tilde{g}$-centric Einstein frame contains a coupling to the scalar field through A's—and thereby g's—dependence on ϕ. The coupling between φ and the curvature sourced by the matter fields has been converted into a direct coupling between ϕ and the matter fields themselves which will mediate a fifth force, as we can see by using the geodesic equation

$$\frac{d^2 x^\mu}{d\tau^2} = -\Gamma^\mu_{\nu\sigma} \frac{dx^\nu}{d\tau} \frac{dx^\sigma}{d\tau} , \tag{1.8}$$

where

$$\Gamma^\mu_{\nu\sigma} = \frac{1}{2} g^{\mu\rho} (g_{\rho\nu,\sigma} + g_{\rho\sigma,\nu} - g_{\nu\sigma,\rho}) \tag{1.9}$$

are the Christoffel symbols of the metric $g_{\mu\nu}$, to give the acceleration of a test particle. Here $g_{\mu\nu}$ is the metric felt by matter fields, and is therefore the metric on whose geodesics matter particles move. Taking the nonrelativistic limit

$$\frac{dx^0}{d\tau} = 1 , \qquad \frac{dx^i}{d\tau} = 0 , \qquad -\tilde{g}_{00} = 1 + 2\Phi , \qquad \Phi \ll 1 , \qquad \tilde{g}_{i0} = 0 , \tag{1.10}$$

where i runs over the spatial indices $\mu \neq 0$ and Φ is the Newtonian gravitational potential, one obtains

$$\frac{d^2 x^i}{d\tau^2} = -\Gamma^i_{00} = -\frac{1}{2} g^{ij} g_{00,j} = \tilde{\partial}^i \Phi + \frac{1}{A} \frac{\partial A}{d\phi} \tilde{\partial}^i \phi =: F_N + F_\phi \tag{1.11}$$

(where $\tilde{\partial}^i$ are derivatives from Eq. (1.9) with the index raised using $\tilde{g}^{ij}$). The $F_N := \tilde{\partial}^i \Phi$ term is the Newtonian gravitational force, and $F_\phi := \frac{\partial \ln A}{d\phi} \tilde{\partial}^i \phi$

5

gives the scalar-mediated fifth force. Importantly, perturbations in ϕ are themselves sourced by matter. The ϕ equation of motion, obtained from varying the action of Eq. (1.6), gains an additional term from $\mathcal{L}_{\mathrm{m}}$ of the form

$$\frac{1}{\sqrt{-\tilde{g}}}\frac{\partial\sqrt{-g}\mathcal{L}_{\mathrm{m}}}{\partial\phi} = \frac{1}{A^4}\frac{1}{\sqrt{-g}}\frac{\partial\sqrt{-g}\mathcal{L}_{\mathrm{m}}}{\partial g^{\mu\nu}}\frac{\partial g^{\mu\nu}}{\partial\phi} = -\frac{1}{A}\frac{\partial A}{\partial\phi}\tilde{T}_{\mu\nu}\tilde{g}^{\mu\nu} \qquad (1.12)$$

(where the last equality uses Eq. (1.3) and $\sqrt{-g}T_{\mu\nu}g^{\mu\nu} = \sqrt{-\tilde{g}}\tilde{T}_{\mu\nu}\tilde{g}^{\mu\nu}$) such that

$$\tilde{\Box}\phi = \frac{\partial}{\partial\phi}\left(\tilde{V}(\phi) + \tilde{T}\ln A\right) , \qquad (1.13)$$

i.e., ϕ couples to the trace of the matter stress–energy $\tilde{T} = \tilde{T}_{\mu\nu}\tilde{g}^{\mu\nu}$ with a coupling strength $\ln A$; throughout this thesis I will consider nonrelativistic perfect fluid-like sources in which $\tilde{T}$ is dominated by the matter density ρ. We call the combination of potential and matter coupling the *effective potential*[3]

$$V_{\mathrm{eff}}(\phi) := \tilde{V}(\phi) + \tilde{T}\ln A . \qquad (1.14)$$

In vacuum around a spherically symmetric source in three spatial dimensions, a scalar field with the quadratic potential $\frac{1}{2}\mu_\phi^2\phi^2$ of Eq. (1.4) and a Yukawa coupling $\ln A(\phi) = \phi/M$ (where M is a mass scale needed to make A dimensionless) will have a Yukawa field profile $\phi_{\mathrm{Yukawa}}(r) = g_3 e^{-\mu_\phi r}/r$ at a distance r from a material body, where g_3 depends on M and also the mass and radius of the source[4], and a corresponding force of $F_{\mathrm{Yukawa}} = \nabla\phi_{\mathrm{Yukawa}} = -g_3(1 + \mu_\phi r)e^{-\mu_\phi r}/r^2$.

Also of interest to us will be the field profile around a cylindrically symmetric source, or equivalently around a spherically symmetric source in two spatial dimensions. There $\phi_{\mathrm{Yukawa}}(r) = g_2 K_0(\mu_\phi r)$ where K_0 is a modified Bessel function of the second kind, for a g_2 that also depends on M and the mass and radius of the source[5], and a corresponding force of $F_{\mathrm{Yukawa}} = \nabla\phi_{\mathrm{Yukawa}} = -g_2\mu_\phi K_1(\mu_\phi r)$. Scalar fields around one-dimensional sources will not be dealt with here, as the models that we will focus on can be and have been studied in an entirely analytical manner [14].

---

[3]A classical object, not to be confused with an 'effective potential' that is formed by adding loop corrections to the tree-level potential, which is the topic of Sec. 2.2.

[4]To find an explicit expression for the constant of integration g_3, one must solve for ϕ both inside and outside the source and enforce that the field profile and its derivative are continuous at the surface of the source. For example, with $\Box\phi = \mu_\phi^2\phi$ in vacuum and the approximation $\Box\phi = \rho/M$ inside the source, $g_3 = m_s/[4\pi M(1 + \mu_\phi r_s)]$, where m_s and r_s are the source mass and radius respectively.

[5]Using the same approximation as the previous footnote, $g_2 = m_s/[2\pi M\mu_\phi r_s K_0(\mu_\phi r_s)]$.

1.3 Screened fifth forces

Yukawa forces are constrained by laboratory tests of gravity such as torsion pendulum experiments and precision measurements of the Casimir force [15, 16]; and by solar-system tests of gravity, in particular lunar laser ranging and planetary orbits [17–19]. However, simple constraints obtained by assuming a quadratic potential for the scalar field, as in Eq. (1.4), are not general.

Non-linearities in the scalar equation of motion mean that fluctuations in the scalar field depend on the evolution of the background scalar field, which is in turn dependent on anything in the environment that the field is coupled to. When this dependence is such that fifth force of Eq. (1.11) is suppressed by its environment, such as by decreasing its range or the strength of its coupling to matter — say, the field follows a Yukawa-like potential $\sim g e^{-\mu_\phi r}/r$ and the coupling g decreases or mass μ_ϕ increases — this is called *screening*, and when the force is screened around dense sources then it may evade precision constraints that are obtained from observations made in the environment around the Sun and Earth.

Screening can be quantified with a *screening factor* λ_s which we will define here to be F_ϕ/F_{Yukawa}, the ratio between the scalar force F_ϕ of Eq. (1.11) experienced by a test particle and the Yukawa force $F_{\text{Yukawa}} \propto \nabla\phi_{\text{Yukawa}}$ described in Sec. 1.2.

In this thesis I will only consider scalar fields whose screening comes from non-linearities in their potential, rather than from non-canonical kinetic terms. Thus there are two such mechanisms of screening, the symmetron and the chameleon, which are conventionally studied in the Einstein frame. Combined with appropriate choices of potential $\tilde{V}(\phi)$ which will be described in their individual sections, the standard symmetron model features a quadratic matter coupling $\ln A \sim \phi^2$ such that $d\ln A$ vanishes as $\phi \to 0$ inside a high local matter density, while chameleon models work with a linear matter coupling $\ln A \sim \phi$ such that the chameleon mass increases with the local matter density.

1.3.1 Symmetron models

In a symmetron model, the coupling to matter decreases as the local matter density increases, vanishing when the density reaches some critical value [20].
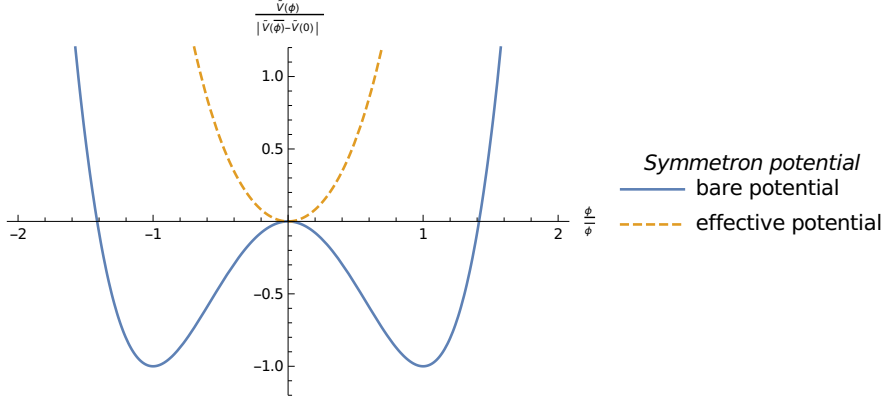
Figure 1: Symmetron bare potential (blue, solid) and an example of a screened effective potential in the presence of a matter density $\rho > \mu^2 M^2$ (orange, dashed).

The potential and the matter coupling are symmetric under $\phi \to -\phi$,

$$\tilde{V}(\phi) = V_0 + \frac{\lambda}{4}\phi^4 - \frac{\mu^2}{2}\phi^2 \ , \qquad A^2(\phi) \sim 1 + \frac{\phi^2}{M^2} \ , \tag{1.15}$$

where V_0 is a constant term of mass dimension four, μ and M are mass scales, and λ is a dimensionless self-coupling constant. As I will discuss in Section 2.2, $\lambda < 1$ is desired to ensure that quantum corrections do not dominate over the bare potential. There is little *a priori* constraint on M, but $M < M_{\mathrm{P}}$ is needed to make the unscreened force stronger than gravity, the situation in which a screening mechanism is necessary. Finally, typical values of μ depend on the context in which the model is being studied: for laboratory tests, the Compton wavelength $\sim 1/\mu$ needs to be comparable to laboratory scales; in other contexts, one needs to consider the effective potential

$$\tilde{V}_{\mathrm{eff}}(\phi) = \frac{\lambda}{4}\phi^4 + \frac{1}{2}\left(\frac{\rho}{M^2} - \mu^2\right)\phi^2 \ . \tag{1.16}$$

The form of the bare potential in Eq. (1.15) is symmetry-breaking such that its minima are at $\pm\mu/\sqrt{\lambda} \neq 0$, and as long as $\rho < \mu^2 M^2$, the effective potential has two minima at $\bar{\phi}(\rho) = \pm\bar{\phi}_\infty\sqrt{1 - \rho/\mu^2 M^2}$, where $\bar{\phi}_\infty = \mu/\sqrt{\lambda}$.

However, when $\rho \geq \mu^2 M^2$, the minimum of $\tilde{V}_{\mathrm{eff}}(\phi)$ vanishes, as seen in Fig. 1, so fluctuations $\delta\phi$ around this minimum couple to matter with strength $\sim \bar{\phi}\delta\phi/M^2 = 0$ and the force is thus screened. For the original

8

cosmological symmetrons, μ is chosen such that this phase transition occurs at late times, around the current cosmic density, therefore $\mu^2 M^2 \sim H_0^2 M_{\mathrm{P}}^2$ [20].

Symmetron-like behaviour has also been studied in a model where the symmetry-breaking potential is generated through loop corrections induced by a coupling to a massless scalar field [21], which is expected to behave in a similar manner to Eq. (1.15) phenomenologically.

Screening factors

In order to treat the screening behaviour analytically, we consider a compact, maximally symmetric source with finite radius r_s, uniform density ρ_{in} and total mass m_s, embedded in a diffuse background with uniform density ρ_{out} that is less than the critical value $\mu^2 M^2$. In the literature, e.g., Ref. [22], the screening of the symmetron fifth force sourced by this object is determined by dividing space into two regions: one inside and one outside the source object. In addition, we make the following assumptions: (i) the field inside the source remains close to zero and (ii) the field outside the source remains close to the value that minimises the effective potential outside the source, which we denote by

$$\bar{\phi}_{\mathrm{out}} \equiv \bar{\phi}(\rho_{\mathrm{out}}) = \bar{\phi}_\infty \sqrt{1 - \rho_{\mathrm{out}}/\mu^2 M^2} \ , \tag{1.17}$$

where we have arbitrarily (but without loss of generality) selected the positive vacuum solution at spatial infinity. We then approximate the effective potential as quadratic about its minimum in each of the two regions. The effective mass of the field inside and outside the source is given by

$$m_{\mathrm{in(out)}}^2 = \left. \frac{\mathrm{d}^2 V_{\mathrm{eff}}(\phi)}{\mathrm{d}\phi^2} \right|_{\substack{\phi = \bar{\phi}_{\mathrm{in(out)}} \\ \rho = \rho_{\mathrm{in(out)}}}} \ , \tag{1.18}$$

where $\bar{\phi}_{\mathrm{in}} = \bar{\phi}(\rho_{\mathrm{in}})$. We impose the boundary conditions that the field be regular at the origin and tend to a constant at infinity, and that ϕ and $\mathrm{d}\phi/\mathrm{d}r$ be continuous at the surface of the source.

After making the assumptions described above and further approximating the fifth force as $\vec{F} = -\phi\vec{\nabla}\phi/M^2 \approx -\bar{\phi}_{\mathrm{out}}\vec{\nabla}\phi/M^2$,[6] the external field profile

---

[6]The full expression for λ_s does not approximate the fifth force $-\phi\vec{\nabla}\phi/M^2$ as $-\bar{\phi}_{\mathrm{out}}\vec{\nabla}\phi/M^2$ and therefore depends on the distance from the source.
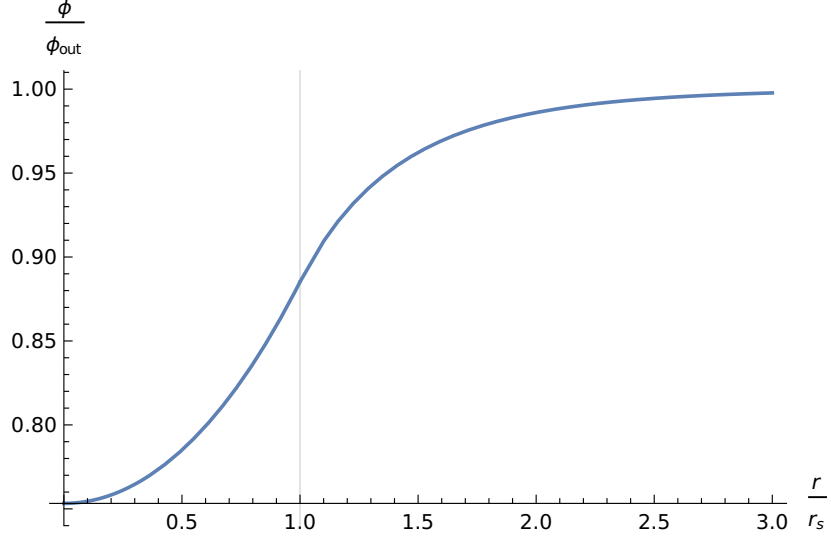
Figure 2: An approximate symmetron field profile around a spherical source of radius r_s, produced by matching a $\sinh(m_{\text{in}}r)/r$ profile in $r < r_s$ to an $e^{-m_{\text{out}}r}/r$ profile in $r > r_s$. In this example, $\mu = 1/r_s$, $\rho_{\text{out}} = 0$, and $\rho_{\text{in}} = 2\mu^2 M^2$. The thin vertical line marks the surface of the source.

around our object, which we centre at the origin, can be written as [23]

$$\phi_{\text{out}}(r) = \bar{\phi}_{\text{out}} - \lambda_s \frac{m_s}{\bar{\phi}_{\text{out}}} \frac{e^{-m_{\text{out}}(r-r_s)}}{(1 + m_{\text{out}}r_s)4\pi r} \;, \tag{1.19}$$

where the screening factor λ_s is given by

$$\lambda_s = \frac{4\pi\bar{\phi}_{\text{out}}^2(1 + m_{\text{out}}r_s)}{m_s}\left(1 - \frac{\bar{\phi}_{\text{in}}}{\bar{\phi}_{\text{out}}}\right)\frac{m_{\text{in}}r_s - \tanh(m_{\text{in}}r_s)}{m_{\text{in}} + m_{\text{out}}\tanh(m_{\text{in}}r_s)} \;. \tag{1.20}$$

An example of a full construction can be seen in Fig. 2.

The cylindrically symmetric (i.e., two-dimensional) case can be treated in a similar manner, with the exterior field falling off as the modified Bessel function of the second kind $K_0(m_{\text{out}}r)$:

$$\phi_{\text{out}}(r) = \bar{\phi}_{\text{out}} - \lambda_s \frac{m_s}{\bar{\phi}_{\text{out}}} \frac{1}{2\pi m_{\text{out}}r_s} \frac{K_0(m_{\text{out}}r)}{K_1(m_{\text{out}}r_s)} \;, \tag{1.21}$$

with

$$\lambda_s = \frac{2\pi\bar{\phi}_{\text{out}}^2}{m_s}\left(1 - \frac{\bar{\phi}_{\text{in}}}{\bar{\phi}_{\text{out}}}\right)\frac{m_{\text{in}}m_{\text{out}}r_s I_1(m_{\text{in}}r_s)K_1(m_{\text{out}}r_s)}{m_{\text{in}}I_1(m_{\text{in}}r_s)K_0(m_{\text{out}}r_s) + m_{\text{out}}I_0(m_{\text{in}}r_s)K_1(m_{\text{out}}r_s)} \;, \tag{1.22}$$
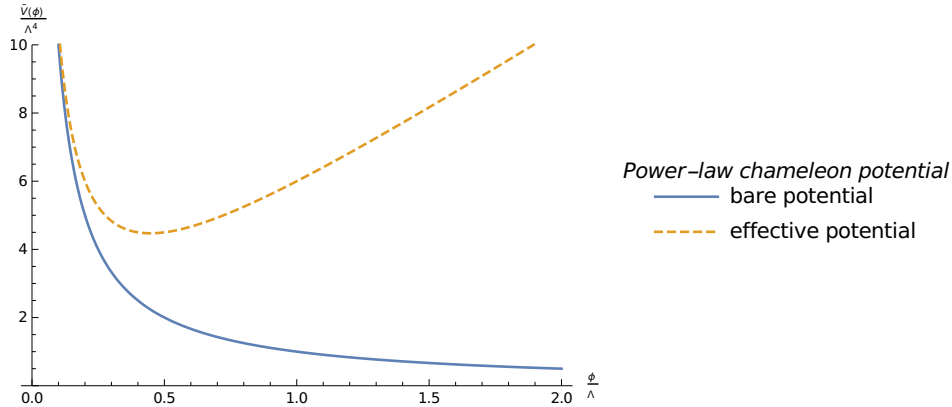
10

Figure 3: Power-law chameleon bare potential (blue, solid) and an example of an effective potential in the presence of a non-zero local matter density (orange, dashed).

where we have again assumed that the fifth force can be approximated as $-\bar{\phi}_{\text{out}}\vec{\nabla}\phi/M^2$.

1.3.2 Chameleon models

In a chameleon model, the scalar mass increases with the local matter density[7]. The prototypical chameleon model [24] features a monotonically decreasing potential and, given the absence of any symmetries forbidding terms that are linear in ϕ, a matter coupling that is to leading order linear

$$\tilde{V}(\phi) = \frac{\Lambda^{4+n}}{\phi^n} \ , \qquad A^2(\phi) \sim 1 + \frac{2\phi}{M} \ , \tag{1.23}$$

for mass scales Λ and M. Often Λ has been considered to be around the scale of the cosmological constant ≈ 2.4 meV, with the idea being that the full potential might be $\sim \Lambda^4 \exp(\Lambda^n/\phi^n)$ such that the leading-order term in the $\phi \gg \Lambda$ expansion is the cosmological constant. However, this region of the parameter space has been almost entirely excluded by precision atomic measurements, interferometry, and Eöt–Wash experiments, which have pushed the space of viable chameleon models to smaller values of Λ [25].

---

[7]Although the symmetron also sees a density-dependent mass with $\mu_\phi^2 \sim \rho$ for large ρ, this is not the primary mechanism of its screening.
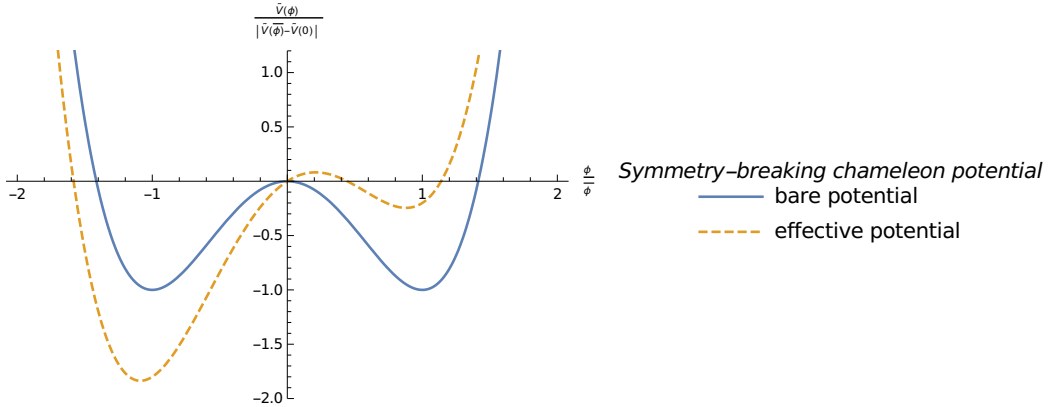
Figure 4: Symmetry-breaking chameleon bare potential (blue, solid) and an example of an effective potential in the presence of a non-zero local matter density (orange, dashed).

Inside a nonrelativistic source of density ρ, the minimum $\bar{\phi}$ of the effective potential

$$\tilde{V}_{\text{eff}}(\phi) = \frac{\Lambda^{4+n}}{\phi^n} + \frac{\rho}{M}\phi \; , \tag{1.24}$$

as shown in Fig. 3, scales as $1/\bar{\phi}^{n+1} \sim \rho$ and therefore the mass-squared $\mu_\phi^2 = \tilde{V}_{\text{eff}}''(\phi)$ around this minimum scales as $\mu_\phi^2 \sim 1/\bar{\phi}^{n+2} \sim \rho^{(n+1)/(n+2)}$. For large ρ and with a large source radius—these will be quantified shortly—the chameleon field will decay to the minimum within a short range of the surface of the source, and will therefore not feel the majority of the source mass which is deeper within the material.

Chameleonic behaviour can occur in a wider variety of theories than those with bare potentials of the form Λ^{4+n}/ϕ^n. For instance, it has been studied in the context of the environmentally-dependent dilaton [26], which in the notation of this thesis used $\tilde{V}(\phi) = V_0 A^4 e^{-\phi/M_{\text{P}}}$.

Throughout this thesis we will also consider a model where a linear matter coupling is paired with a symmetron-like potential, previously studied as a toy model of the Higgs with a Yukawa coupling [14], giving an effective potential

$$\tilde{V}_{\text{eff}}(\phi) = \frac{\lambda}{4}\phi^4 - \frac{\mu^2}{2}\phi^2 + \frac{\rho}{M}\phi \; , \tag{1.25}$$

as seen in Fig. 4. This is still a chameleon theory, as for large $\rho \gg \mu^3 M/\sqrt{\lambda}$ the minimum $\bar{\phi}$ of the effective potential scales as $\bar{\phi}^3 \sim -\rho$ such that the

12

mass scales as $\mu_\phi^2 \sim \bar{\phi}^2 \sim \rho^{2/3}$, with the caveat that—if this is to be a scalar–tensor theory with a Jordan-frame description—higher-order terms in $A(\phi)$ must come into play at large negative ϕ in order to ensure that $A = 0$ is not reached by the field reaching $\phi = -M$.

Although I have so far mentioned only theories with a Jordan-frame action of the form Eq. (1.5), there is an even simpler option for the chameleon. The presence of kinetic terms for $\ln A$ in Eq. (1.7b) means that a theory without a kinetic term for a scalar field in the Jordan frame can still become a scalar field theory in the Einstein frame with a linear matter coupling $\ln A \propto \phi$. Such a theory is known to be equivalent to $f(R)$ gravity, in which the Jordan-frame action is that of Einstein–Hilbert, Eq. (1.1), but with $R \to f(R)$ such that $A^2(\varphi) \equiv f'(R)$ and $V(\varphi) \equiv \frac{1}{2}M_\mathrm{P}^2(f'(R)R - f(R))$; therefore $f(R)$ gravity theories can experience chameleon screening [27–29].

Screening factors

Considering again a uniform-density, maximally symmetric source of mass m_s and radius r_s, embedded in a low-density background, the standard approach to computing the chameleon screening factor is to divide space into three regions: one outside and two inside the source [30]. In the innermost region, the field is so massive that the field value is approximately constant. The surface of this region defines a "thin shell" radius r_shell with $0 \leq r_\mathrm{shell} \leq r_s$. In the region $r_\mathrm{shell} \leq r \leq r_s$, the effective potential is dominated by the matter coupling.

The exterior field profile around a homogeneous spherically-symmetric source of radius r_s is [31]

$$\phi_\mathrm{out}(r) = \bar{\phi}_\mathrm{out} - \lambda_s \frac{m_s}{M} \frac{e^{-m_\mathrm{out}(r-r_s)}}{(1 + m_\mathrm{out}r_s)4\pi r} \ . \tag{1.26}$$

The resulting screening factor is given by

$$\lambda_s = 1 - \left(\frac{r_\mathrm{shell}}{r_s}\right)^3 \tag{1.27}$$

and, taking $m_\mathrm{out}r \ll 1$, the thin-shell radius is

$$r_\mathrm{shell} = r_s \sqrt{1 - \frac{2M(\bar{\phi}_\mathrm{out} - \bar{\phi}_\mathrm{in})}{\rho_\mathrm{in}r_s^2}} \ . \tag{1.28}$$

13

Only the matter within the shell near the surface of the object sources perturbations in the field. This form of the solution holds for all models with a linear coupling to matter, as different self-interaction potentials $V(\phi)$ merely lead to different expressions for $\bar{\phi}_{\text{out}}$.

When $r_{\text{shell}} = 0$ (or r_{shell} has no real solutions) and $\lambda_s = 1$, which occurs for $2M(\bar{\phi}_{\text{out}} - \bar{\phi}_{\text{in}}) \geq \rho_{\text{in}} r_s^2$, the field cannot reach its minimum anywhere and the object is entirely unscreened. When $r_{\text{shell}} \to r_s$ and $\lambda_s \to 0$, occurring when $\rho_{\text{in}} r_s^2 \gg 2M(\bar{\phi}_{\text{out}} - \bar{\phi}_{\text{in}})$, the field quickly drops to its minimum near the surface of the source and the object is maximally screened.

The cylindrically symmetric or two-dimensional case is similar, with [31]

$$\phi_{\text{out}}(r) = \bar{\phi}_{\text{out}} - \lambda_s \frac{m_s}{M} \frac{1}{2\pi m_{\text{out}} r_s} \frac{K_0(m_{\text{out}} r)}{K_1(m_{\text{out}} r_s)} \ , \qquad \lambda_s = 1 - \left(\frac{r_{\text{shell}}}{r_s}\right)^2 \ , \quad (1.29)$$

and the thin-shell radius r_{shell} is given by

$$\left(\frac{r_{\text{shell}}}{r_s}\right)^2 = \frac{-(X+Y)}{W_{-1}(-e^{-X}(X+Y))} \ , \qquad (1.30)$$

where

$$X = 1 + \frac{2}{m_{\text{out}} r_s} \frac{K_0(m_{\text{out}} r_s)}{K_1(m_{\text{out}} r_s)} \ , \qquad Y = \frac{4M(\bar{\phi}_{\text{in}} - \bar{\phi}_{\text{out}})}{\rho r_s^2} \ , \qquad (1.31)$$

and W_k denotes the kth real branch of the Lambert W function. The argument of the W function becomes non-negative when $X < -Y$, and Eq. (1.30) no longer gives an r_{shell} between 0 and r_s. As the argument approaches zero, the W function tends to $-\infty$, $r_{\text{shell}} \to 0$, and the source is unscreened.

1.4 Tests for screened fifth forces

Screened fifth forces, hidden from conventional tests, need unconventional tests to uncover them or, conversely, to rule out their existence. Such tests occur in a vacuum environment in order to minimise the risk that the background density is sufficient for screening, and therefore tend to involve astrophysical or cosmological observations [5,25], experiments conducted inside vacuum chambers [5,25], or experiments searching for violations of the equivalence principle in space [32].

As chameleon screening between masses depends on the density and physical dimensions of the masses—for a spherical source this is the combination

$\rho_{\text{in}} r_s^2$—tests for chameleons often feature sources that minimise their spatial extent in some way so as to maximise the chameleon force. Searches for chameleons that make use of this feature include torsion pendulum and Eöt-Wash experiments [15, 33, 34], and precision measurements of the Casimir force [35–37], all of which are used to measure the force between thin plates; and atom [31, 38–41] and neutron interferometry [42, 43], which use particles that might be very dense but have very small source radii. In a similar vein, searches for fifth forces have been conducted using optically levitated microspheres [44], which are neither dense nor large; another proposal is to measure the effect of a fifth force on the cyclotron motion of charged particles [45].

Constraints on the chameleon have almost entirely excluded the parameter space where $\Lambda \gtrsim 2.4$ meV, the dark energy scale [25]. As symmetron screening, however, depends only on whether the density is greater than the critical density $\mu^2 M^2$ and is not alleviated by a small spatial extent, many fifth force experiments that provide stringent constraints for the chameleon are less effective in constraining the symmetron but are nevertheless valuable [23, 40, 41, 46, 47]. On the other hand, symmetrons can display behaviour impossible for the chameleon: the presence of degenerate minima in the symmetron potential makes domain walls possible, which could be detected if they form inside vacuum chambers [23, 48] or pass close to the Earth [49].

Not all tests that are designed for screened scalar fields are directly tests for the resulting fifth forces. Constraints can also be obtained from measurements of the electron magnetic moment [50], from searches for variations in the fine-structure constant and fermion masses [49], and from neutron spectroscopy [51].

1.5 Outline of this Thesis

In Section 2, I will look at the contributions of a non-minimal coupling (Section 2.1) and one-loop corrections (Section 2.2) to the dynamics of a scalar field, ultimately obtaining sets of bounds—Eq. (2.40) and (2.43)—for the symmetron and the symmetron-like chameleon in which we can trust the classical Einstein-frame Eqs. (1.15) and (1.25) to provide reliable predictions for observations and experiments.

The remainder of this thesis will then focus on the consequences of non-linearities in the equation of motion, primarily for the symmetron, for two scenarios of interest. Section 3 will examine the superradiant instability of scalar fields around Kerr black holes, and Section 4 is a study of the sym-

metron, and the chameleon of Eq. (1.25), around compact spherical objects, ending with scaling relationships and screening factors that can be applied even in the limit of point-like sources.

2 Suitability of the Classical Approximation

Before we can assess when the linearised Eq. (1.4) is a suitable approximation for a model such as Eq. (1.15) or Eq. (1.24), we must first determine whether models such as Eq. (1.15) or Eq. (1.24) are themselves reliable given the effects of non-minimal couplings and quantum corrections.

Sections 2.1 and 2.2 will examine respectively a non-minimal coupling and one-loop corrections, and will conclude in both cases that the effects can be accounted for by additional non-linearities in the effective potential that are suppressed with respect to those of the bare potential under sets of bounds given in Eq. (2.40) and (2.43).

2.1 Non-minimal coupling contributions

As shown in Section 1.2, a non-minimal gravitational coupling term in the action of the form $A^2(\varphi)R$ can be removed by a suitable conformal transformation. One might therefore suppose that, since in the Einstein frame the scalar field equation of motion in vacuum is exactly $\tilde{\Box}\phi = \tilde{V}'(\phi)$, the effects of non-minimal couplings are nonexistent in the absence of matter. Similarly, the Jordan-frame equation of motion reduces to the simple $\Box\varphi = V'(\varphi)$ in vacuum when the curvature $R = 0$.

However, φ has its own stress–energy and therefore it sources a non-zero curvature, so the Jordan-frame equation of motion must be more complicated than it would at first appear, and a frame transformation cannot cause the physics of the coupling to cease to exist, so this physics must also be hiding somewhere in the Einstein-frame equation of motion. In this section I shall uncover where exactly the physics is hiding, and what form it takes—how the form of $\tilde{\Box}\phi = \tilde{V}'(\phi)$ differs from that of $\Box\varphi = V'(\varphi)$—after the conformal transformation has been performed.

Consider the transformation between Eqs. (1.5) and (1.6),

$$S = \int d^4x \sqrt{-g}\mathcal{L}_\varphi, \qquad \mathcal{L}_\varphi = \frac{M_P^2}{2}A^2(\varphi)R - \frac{1}{2}g^{\mu\nu}\nabla_\mu\varphi\nabla_\nu\varphi - V(\varphi)\ ,$$

$$S = \int d^4x \sqrt{-\tilde{g}}\mathcal{L}_\phi, \qquad \mathcal{L}_\phi = \frac{M_P^2}{2}\tilde{R} - \frac{1}{2}\tilde{g}^{\mu\nu}\tilde{\nabla}_\mu\phi\tilde{\nabla}_\nu\phi - \tilde{V}(\phi)\ ,$$

via Eqs. (1.7a) and (1.7b),

$$\sqrt{-\tilde{g}} = A^4 \sqrt{-g} \,, \tag{2.2a}$$

$$\tilde{R} = A^{-2} \left(R - 6g^{\mu\nu}\nabla_\mu\nabla_\nu \ln A - 6g^{\mu\nu}\nabla_\mu \ln A \nabla_\nu \ln A \right) \,, \tag{2.2b}$$

more closely. To compare the terms in the two frames it is easiest to transform the $\mathcal{L}_\phi$ action into the Jordan frame. The $\tilde{R}$ term sees the greatest change:

$$\sqrt{-\tilde{g}}\frac{M_{\mathrm{P}}^2}{2}\tilde{R} = A^4 \sqrt{-g}\frac{M_{\mathrm{P}}^2}{2}A^{-2}\left(R - 6g^{\mu\nu}\nabla_\mu\nabla_\nu \ln A - 6g^{\mu\nu}\nabla_\mu \ln A \nabla_\nu \ln A \right)$$

$$= \sqrt{-g}\left(\frac{M_{\mathrm{P}}^2}{2}A^2 R - 3M_{\mathrm{P}}^2 A^2 g^{\mu\nu}\nabla_\mu\nabla_\nu \ln A - 3M_{\mathrm{P}}^2 A^2 g^{\mu\nu}\nabla_\mu \ln A \nabla_\nu \ln A \right)$$

$$= \sqrt{-g}\left(\frac{M_{\mathrm{P}}^2}{2}A^2 R + 3M_{\mathrm{P}}^2 A^2 g^{\mu\nu}\nabla_\mu \ln A \nabla_\nu \ln A \right) \,. \tag{2.3}$$

In the final line we have integrated by parts to find

$$A^2 \nabla^\mu \nabla_\mu \ln A = \nabla^\mu (A^2 \nabla_\mu \ln A) - 2A^2 \nabla^\mu \ln A \nabla_\mu \ln A$$

and, as we take spacetime to have no boundaries and all fields to attain a constant value at infinity, removed the resulting total divergence. The other two terms in the Lagrangian of Eq. (1.6) become

$$\sqrt{-\tilde{g}}\frac{1}{2}\tilde{g}^{\mu\nu}\tilde{\nabla}_\mu\phi\tilde{\nabla}_\nu\phi = \sqrt{-g}\frac{1}{2}A^2 g^{\mu\nu}\nabla_\mu\phi\nabla_\nu\phi \,, \tag{2.4a}$$

$$\sqrt{-\tilde{g}}\tilde{V}(\phi) = A^4 \sqrt{-g}\tilde{V}(\phi) \,. \tag{2.4b}$$

Under these transformations, $\mathcal{L}_\phi$ is transformed into

$$\frac{\sqrt{-\tilde{g}}}{\sqrt{-g}}\mathcal{L}_\phi = \frac{M_{\mathrm{P}}^2}{2}A^2 R + \frac{1}{2}\left(6M_{\mathrm{P}}^2 \left(\frac{dA}{d\varphi}\right)^2 - A^2 \left(\frac{d\varphi}{d\phi}\right)^{-2} \right)g^{\mu\nu}\nabla_\mu\varphi\nabla_\nu\varphi - V(\varphi) \tag{2.5}$$

and, in the other direction, $\mathcal{L}_\varphi$ is transformed into

$$\frac{\sqrt{-g}}{\sqrt{-\tilde{g}}}\mathcal{L}_\varphi = \frac{M_{\mathrm{P}}^2}{2}\tilde{R} - \frac{1}{2A^2}\left(6M_{\mathrm{P}}^2 \left(\frac{dA}{d\phi}\right)^2 + \left(\frac{d\varphi}{d\phi}\right)^2 \right)\tilde{g}^{\mu\nu}\nabla_\mu\phi\nabla_\nu\phi - \tilde{V}(\phi). \tag{2.6}$$

Equating the kinetic term in Eq. (2.5) with that in $\mathcal{L}_\varphi$, and the kinetic term in Eq. (2.6) with that in $\mathcal{L}_\phi$, tells us that

$$\frac{d\phi}{d\varphi} = \sqrt{\frac{1 + 6M_{\mathrm{P}}^2 \left(\frac{dA}{d\varphi}\right)^2}{A^2}} = \sqrt{\frac{1}{A^2 - 6M_{\mathrm{P}}^2 \left(\frac{dA}{d\phi}\right)^2}} \tag{2.7}$$

where each of the two expressions is useful if we know A as a function of φ or of ϕ respectively. As long as $(dA/d\varphi)^2$, $(dA/d\phi)^2 \ll 1/M_{\mathrm{P}}^2$, the expressions simplify and $d\phi/d\varphi \to 1/A$.

The fact that the scalar field is transformed between the two frames, combined with the relationship $V(\varphi) = A^4 \tilde{V}(\phi)$, shows us that we can expect the effects of the non-minimal coupling to be reflected in the differences between the Jordan- and Einstein-frame forms of the potential.

However, this does not mean that we cannot use $\Box \varphi = V'(\varphi)$, as a good approximation to the true equation of motion $\tilde{\Box} \phi = \tilde{V}'(\phi)$. The differences between the equations of motion in the two frames may be suppressed, such as when the curvature sourced by φ is sufficiently small such that $A^2(\varphi) \approx 1$, as is the case when $A^2(\varphi) \sim 1 + 2\varphi^n/n!M^n$ and $|\varphi| \ll M$. In such a situation, $\phi \approx \varphi$, up to a constant of integration[8].

It is necessary to assess the suitability of an approximation of the form $\Box \varphi = V'(\varphi)$ on a model-by-model basis. I will do this for the symmetron in Section 2.1.1 and for the chameleon in Section 2.1.2.

2.1.1 Quadratic matter coupling and symmetrons

The quadratic matter coupling $A^2(\varphi) \sim 1 + \varphi^2/M^2$ needs only $\varphi^2/M^2 \ll M^2/M_{\mathrm{P}}^2$ to give us the approximation $d\phi = d\varphi/A$, which may be integrated to get

$$\phi = \varphi - \frac{\varphi^3}{6M^2} + \mathcal{O}\left(\frac{\varphi^4}{M^4}\right) \ . \tag{2.8}$$

The same logic can be applied to $A^2(\phi) \sim 1 + \phi^2/M^2$, giving

$$\varphi = \phi + \frac{\phi^3}{6M^2} + \mathcal{O}\left(\frac{\phi^4}{M^4}\right) \ . \tag{2.9}$$

---

[8]This constant, call it c, does not change the kinetic term, nor does it change the form of the potential. What it does is shift the potential from $\tilde{V}(\phi) \to \tilde{V}(\phi + c)$ and therefore the zero of the potential to $-c$. Choosing a non-zero constant of integration c therefore amounts to taking an expansion of the potential around $\phi = -c$.

The symmetron model [20], as described in Section 1.3.1, has such a quadratic matter coupling with a symmetry-breaking potential such as

$$V(\varphi) = V_0 + \frac{\lambda}{4}\varphi^4 - \frac{\mu^2}{2}\varphi^2 \ , \qquad (2.10)$$

where V_0 is a constant term of mass dimension four, μ is a mass scale, and λ is a dimensionless self-coupling constant. The minimum of this potential is $\bar{\varphi} = \mu/\sqrt{\lambda}$. When Eq. (2.10) is the potential in the Jordan frame, the potential in the Einstein frame is

$$\tilde{V}(\phi) = V_0 + \frac{\lambda}{4}\left(1 + \frac{10}{3}\frac{\bar{\varphi}^2}{M^2}\right)\phi^4 - \frac{\mu^2}{2}\left(1 + \frac{4V_0}{\mu^2 M^2}\right)\phi^2 - \frac{\lambda}{3}\frac{\phi^2}{M^2}\phi^4 + \mathcal{O}\left(\frac{\phi^4}{M^4}\right)$$
$$(2.11)$$

where the coefficients of the $\mathcal{O}(\phi^4/M^4)$ terms depend on higher-order terms in $A(\phi)$. The leading-order addition to the potential is of order ϕ^2/M^2, which we take to be small in order to ensure that $A \approx 1$. There are also $\bar{\varphi}^2/M^2$ and $V_0/\mu^2 M^2$ corrections to the values of λ and μ^2 respectively; if $V_0 \lesssim \mu^4/\lambda$ then $V_0/\mu^2 M^2 \lesssim \bar{\varphi}^2/M^2$ and these corrections are both guaranteed to be small as well.

A change that is not immediately quantified by Eq. (2.11) is that the minimum of $\tilde{V}(\phi)$ is generally displaced from $\phi = \bar{\varphi}$, which is important to recognise if one attempts to find a linearised approximation like Eq. (1.4) to the symmetron by taking a Taylor expansion of the potential around its minimum. This displacement is not only due to the inequality between φ and ϕ, but also because φ couples to the curvature sourced by a non-zero $V(\bar{\varphi})$, and so the Jordan-frame potential will also have the location of its minimum shifted from $\mu/\sqrt{\lambda}$ unless $V_0 = \mu^4/4\lambda$ such that $V(\bar{\varphi}) = 0$. It turns out that the Einsten-frame minimum $\bar{\phi}$ will be displaced from $\mu/\sqrt{\lambda}$ unless $V_0 = \mu^4/3\lambda$, to leading order.

In order to isolate the cause of the displaced minimum from the Einstein-frame viewpoint and thereby determine when it can be neglected, it is helpful to expand Eqs. (2.10) and (2.11) around $\varphi, \phi = \bar{\varphi}$ and express the result in terms of the field excursions $(\psi, \tilde{\psi}) = (\varphi, \phi) - \bar{\varphi}$. The original potential Eq. (2.10) becomes

$$V(\psi) = V_0 - \frac{\mu^4}{4\lambda} + \frac{\mu^4}{\lambda}\left[\left(\frac{\psi}{\bar{\varphi}}\right)^2 + \left(\frac{\psi}{\bar{\varphi}}\right)^3 + \frac{1}{4}\left(\frac{\psi}{\bar{\varphi}}\right)^4\right] \ . \qquad (2.12)$$

21

Then $\tilde{V}(\tilde{\psi})$ acquires several differences: Firstly, each of the terms in Eq. (2.12) is transformed into an infinite series of order $(\bar{\varphi}/M)^{2m}$ terms with integers $m \geq 0$. Secondly, there are also terms of higher order in $\tilde{\psi}$, which are generally negligible when $\tilde{\psi} \ll \bar{\varphi}$ and are further suppressed by factors of order $\bar{\varphi}^2/M^2$. Both of these types of contributions are therefore of the same order as those that can be seen in Eq. (2.11). Finally, $\tilde{V}(\tilde{\psi})$ has an $\mathcal{O}(\tilde{\psi}/\bar{\varphi})$ term and this is responsible for $\bar{\phi} \neq \bar{\varphi}$; its coefficient is $-4V_0\bar{\varphi}^2/M^2$ or $+4\bar{\varphi}^4\mu^2/3M^2$ (depending on the presence and size of V_0). To ensure that Eq. (2.10) is a valid approximation to $\tilde{V}(\tilde{\psi})$, the most restrictive condition is that the $\tilde{\psi}^4$ term remains dominant over this $\tilde{\psi}$ term, which requires

$$\frac{16}{\lambda} \frac{V_0}{\bar{\varphi}^2 M^2} \, , \, \frac{16}{3} \frac{\bar{\varphi}^2}{M^2} \ll \frac{\tilde{\psi}^3}{\bar{\varphi}^3} \, . \tag{2.13}$$

When $|V_0| \lesssim \mu^4/\lambda$, these become another constraint that $\bar{\varphi}^2/M^2$ must be small, although here it must also be smaller than $(\tilde{\psi}/\bar{\varphi})^3$ that may itself be $\ll 1$.

2.1.2 Linear matter coupling and chameleons

Naïvely, we run into a problem when trying to transform a linearly-coupled theory between the Jordan and Einstein frames. The final expression in Eq. (2.7) is not real unless the theory in the Einstein frame satisfies

$$A^2 \geq 6M_{\mathrm{P}}^2 \left(\frac{dA}{d\phi}\right)^2 \, . \tag{2.14}$$

In theories such as the symmetron or with even higher-order couplings, $dA/d\phi$ will be at least of order ϕ/M and so this constraint is easily satisfied for $|\phi| \ll M$, telling us only that higher-order terms in A^2 will become relevant for larger $|\phi|$. However, with a linear coupling $A^2(\phi) \sim 1 + 2\phi/M$, the constraint turns into $A^2 \geq 6M_{\mathrm{P}}^2/M^2$.

The constraint Eq. (2.14) thus cannot be satisfied given $A^2(\phi) \sim 1+2\phi/M$ with both $\phi \ll M$, which we need so as to ensure that any results are not dependent on the exact form of $A(\phi)$, and $M < \sqrt{6}M_{\mathrm{P}}$, which is the situation that we are interested in as forces with $M > M_{\mathrm{P}}$ are weaker than gravity and so do not require screening to remain hidden. We cannot then talk about contributions caused by non-minimal coupling when the bare equation of motion $\Box\varphi = V'(\varphi)$ does not exist.

To see what happens when we try to transform a linearly-coupled theory with small M into the Einstein frame using Eq. (2.7), consider starting from a Jordan-frame coupling $A^2(\varphi) = 1 + 2\varphi/M$ with $A \approx 1$, $M^2 \ll M_\mathrm{P}^2$. Then from Eq. (2.7) we find $d\phi/d\varphi \approx \sqrt{6}M_\mathrm{P}/MA^2$, which gives

$$\phi = \frac{\sqrt{6}}{2}M_\mathrm{P} \ln\left(1 + \frac{2\varphi}{M}\right) \;\Rightarrow\; A^2 = 1 + \frac{2\varphi}{M} = e^{2\phi/\sqrt{6}M_\mathrm{P}} \;, \tag{2.15}$$

or to leading order

$$\phi = \frac{\sqrt{6}M_\mathrm{P}}{M}\varphi \;\Rightarrow\; A^2 = 1 + \frac{2\phi}{\sqrt{6}M_\mathrm{P}} \;. \tag{2.16}$$

An arbitrarily small Jordan-frame M has given us an Einstein-frame coupling scale of $\sqrt{6}M_\mathrm{P}$. Note that the scale M hasn't been removed from the theory; it will still be present in the form of $\mathcal{O}(M^2/M_\mathrm{P}^2)$ terms.

A special case of this frame transformation is when $A^2 = e^{2\varphi/M} = e^{2\phi/\sqrt{6}M_\mathrm{P}}$ exactly. In this case the kinetic term of the Jordan-frame action Eq. (2.5) vanishes and we therefore have $f(R)$ gravity as mentioned in Section 1.3.2; M disappears as there is no independent scale $M \not\equiv \sqrt{6}M_\mathrm{P}$ in the Jordan frame to begin with [27–29].

The source of the apparent impossibility of obtaining $M < \sqrt{6}M_\mathrm{P}$ is that Eq. (2.7) is based on the assumption that the action in Eq. (2.5) has a canonical sign on its kinetic term as does our original Jordan-frame action in Eq. (1.5). If the Jordan and Einstein frames are equivalent on a quantum level then this cannot be necessary, as the Einstein-frame action in Eq. (1.6) is clearly free of pathologies even for small values of M. One could then argue that the reason why a 'canonical' kinetic term in the Jordan frame is not necessary is that the $A^2(\varphi)R$ term in the Jordan-frame action means that the metric, and therefore the theory as a whole, is not canonically normalised. anyway. This would mean that in the Jordan-frame description, the φ ghosts must somehow be kept in check by the $A^2(\varphi)R$ coupling even in vacuum where $R \to 0$.

Assuming for the sake of calculation that it is viable to have a chameleon in the Jordan frame whose Einstein-frame matter coupling is small, let us consider here the consequences of a 'non-canonical' Jordan-frame chameleon. What we must do to get a theory with a small Einstein-frame M is then to take an action like the Jordan-frame Eq. (1.5) but give it the 'wrong' sign

in its kinetic term, such that we are comparing the potential in $\Box\phi = \tilde{V}'(\phi)$ to that in the 'uncorrected' $-\Box\varphi = V'(\varphi)$. Changing the sign of the kinetic term in Eq. (1.5) turns Eq. (2.7) into

$$
\frac{d\phi}{d\varphi} = \sqrt{\frac{6M_{\mathrm{P}}^2 \left(\frac{dA}{d\varphi}\right)^2 - 1}{A^2}} = \sqrt{\frac{1}{6M_{\mathrm{P}}^2 \left(\frac{dA}{d\phi}\right)^2 - A^2}} \tag{2.17}
$$

and so we can make sense of an Einstein-frame $M \ll M_{\mathrm{P}}$ such that $d\phi/d\varphi \sim AM/\sqrt{6}M_{\mathrm{P}}$. Thus in this case we now find that an arbitrarily small Einstein-frame M corresponds to a Jordan-frame coupling scale of $\sqrt{6}M_{\mathrm{P}}$, and taking $A \sim 1 + \phi/M$ gives us, to $\mathcal{O}(\phi/M)$,

$$
\varphi = \frac{\sqrt{6}M_{\mathrm{P}}}{M} \left(\phi - \frac{\phi^2}{2M}\right), \qquad \phi = \frac{M}{\sqrt{6}M_{\mathrm{P}}} \left(\varphi + \frac{\varphi^2}{2M}\right) . \tag{2.18}
$$

The original chameleon model [24], as described in Section 1.3.2, involves a linear matter coupling and an inverse power-law potential, of which the simplest is $V(\varphi) = \Lambda^5/\varphi$. When this is in the Jordan frame, with $A^2(\varphi) \sim 1 + 2\varphi/\sqrt{6}M_{\mathrm{P}}$, the potential in the Einstein frame is

$$
\tilde{V}(\phi) = \frac{\Lambda^5}{M_{\mathrm{P}}} \left(\frac{M}{\sqrt{6}\phi} + \text{constant} + \mathcal{O}\left(\frac{\phi}{M}\right)\right) . \tag{2.19}
$$

The leading-order effect on the non-minimal coupling contributions is simply the swapping of $\varphi/\sqrt{6}M_{\mathrm{P}}$ with ϕ/M, such that the chameleon scale Λ has been effectively transformed into some $\tilde{\Lambda} = (M/\sqrt{6}M_{\mathrm{P}})^{1/5}\Lambda$. The overall constant term is $\Lambda^5(1/2\sqrt{6} - 4)/M_{\mathrm{P}}$ plus any constant that is present in the full Jordan-frame potential.

The coefficients of the $\mathcal{O}(\phi/M)$ terms in Eq. (2.19) depend on higher-order terms in $A^2(\phi)$ (and the presence of any constants in the Jordan-frame potential) so we cannot quantify them exactly, but they are generally non-zero and so the chameleon minimum will be at a finite value even in vacuum.

The chameleon model of Eq. (1.25) combines the linear coupling to matter with the symmetron-like bare potential of Eq. (2.10). Transforming this Jordan-frame potential into the Einstein frame with $A^2(\varphi) \sim 1 + 2\varphi/\sqrt{6}M_{\mathrm{P}}$,

24

and performing the rescalings $\mu \to \mu M/\sqrt{6}M_{\mathrm{P}}$ and $\lambda \to \lambda M^4/36M_{\mathrm{P}}^4$, gives

$$
\begin{aligned}
\tilde{V}(\phi) = V_0 \left(1 - 4\sqrt{6}\frac{\phi}{M} \right) &+ \frac{\lambda}{4} \left(1 - 2(1 + 2\sqrt{6})\frac{\phi}{M} \right) \phi^4 \\
&- \frac{\mu^2}{2} \left(1 + (1 + 4\sqrt{6})\frac{\phi}{M} \right) \phi^2 + \mathcal{O}\left(\frac{\phi^2}{M^2} \right)
\end{aligned}
\tag{2.20}
$$

where, as with Eq. (2.19), the coefficients of the higher-order terms generally depend on higher-order terms in $A^2(\phi)$ so we cannot quantify them exactly. As with the symmetron, the Einstein-frame minimum $\bar{\phi}$ of $\tilde{V}(\phi)$ will be displaced from $\bar{\varphi} = \mu/\sqrt{\lambda}^9$, in this case unless $V_0 = (1 - 1/\sqrt{6})\mu^4/4\lambda$, to leading order. And again as with the symmetron, it is helpful to rewrite Eq. (2.20) in terms of $\tilde{\psi} = \phi - \bar{\varphi}$ and compare it with Eq. (2.12). In this case, each of the terms in Eq. (2.12) is transformed into an infinite series of order $(\tilde{\varphi}/M)^m$ terms with integers $m \geq 0$, and terms of higher order in $\tilde{\psi}$ are further suppressed by factors of order $\bar{\varphi}/M$. The $\mathcal{O}(\tilde{\psi}/\bar{\varphi})$ term has a coefficient of $-4\sqrt{6}V_0\bar{\varphi}/M$ or $+(\sqrt{6}-1)\bar{\varphi}^3\mu^2/M$ (depending on the presence and size of V_0), so requiring that the $\tilde{\psi}^4$ term remains dominant over the $\tilde{\psi}$ term gives

$$
\frac{4\sqrt{6}}{\lambda}\frac{V_0}{\bar{\varphi}^3 M} \ , \ 4(\sqrt{6}-1)\frac{\bar{\varphi}}{M} \ll \frac{\tilde{\psi}^3}{\bar{\varphi}^3} \ .
\tag{2.21}
$$

When $|V_0| \lesssim \mu^4/\lambda$, these become another constraint that $\bar{\varphi}/M$ must be small, although here it must also be smaller than $(\tilde{\psi}/\bar{\varphi})^3$ that may itself be $\ll 1$.

2.1.3   Equations of motion

Although a careful look at the Weyl transformation of the action, as performed earlier in this section, shows us where the effects of the non-minimal coupling are to be found in the Einstein frame, for completeness I shall now examine how the equations of motion are transformed.

In the absence of matter fields, the gravitational equations of motion from the Einstein-frame action are, by construction, the Einstein field equations $M_{\mathrm{P}}^2\tilde{G}_{\mu\nu} = \tilde{T}_{\mu\nu}$ sourced by the stress–energy tensor $\tilde{T}_{\mu\nu}$ of the scalar field ϕ. Meanwhile, the equation of motion for the scalar field is simply $\tilde{\Box}\phi = \tilde{V}'(\phi)$.

---

[9]Somewhat of an abuse of notation, as μ and λ here are different from those in Eq. (2.10) such that this "$\bar{\varphi}$" and the Jordan-frame $\bar{\varphi}$ differ by a factor of $\sqrt{6}M_{\mathrm{P}}/M$.

For the Jordan-frame actions, the gravitational equations of motion are more complicated, as we have

$$\delta(A^2 R) = A^2 R_{\mu\nu} \delta g^{\mu\nu} + g^{\mu\nu} \delta(A^2 R_{\mu\nu}) = (R_{\mu\nu} - \nabla_\mu \nabla_\nu + g_{\mu\nu} \Box) A^2 \delta g^{\mu\nu} \quad (2.22)$$

and therefore the gravitational equations from Eq. (1.5) are

$$A^2 G_{\mu\nu} = (\nabla_\mu \nabla_\nu - g_{\mu\nu} \Box) A^2 + \frac{1}{M_{\mathrm{P}}^2} \nabla_\mu \varphi \nabla_\nu \varphi - \frac{1}{M_{\mathrm{P}}^2} g_{\mu\nu} \left(\frac{1}{2} (\nabla\varphi)^2 + V(\varphi) \right)$$
$$(2.23)$$

from which we can take the trace to obtain

$$A^2 R = 3 \Box A^2 + \frac{1}{M_{\mathrm{P}}^2} (\nabla\varphi)^2 + \frac{4 V(\varphi)}{M_{\mathrm{P}}^2} \ . \quad (2.24)$$

Meanwhile, the scalar field equation of motion is

$$\Box \varphi = V'(\varphi) - M_{\mathrm{P}}^2 A \frac{dA}{d\varphi} R \quad (2.25)$$

in which we can eliminate R to end up with

$$\Box \varphi + \frac{1}{A} \frac{dA}{d\varphi} (\nabla\varphi)^2 = V'(\varphi) - \frac{4 V(\varphi)}{A} \frac{dA}{d\varphi} - \frac{3 M_{\mathrm{P}}^2}{A} \frac{dA}{d\varphi} \Box A^2 \ . \quad (2.26)$$

When this equation is transformed into the Einstein frame, the potential terms simplify as

$$V'(\varphi) = \frac{\partial}{\partial \varphi} \left(A^4 \tilde{V}(\phi) \right) = 4 A^3 \tilde{V}(\phi) \frac{dA}{d\varphi} + A^4 \frac{d\phi}{d\varphi} \tilde{V}'(\phi) \ , \quad (2.27a)$$

$$-\frac{4 V(\varphi)}{A} \frac{dA}{d\varphi} = -4 A^3 \tilde{V}(\phi) \frac{dA}{d\varphi} \ . \quad (2.27b)$$

The two Jordan-frame V-dependent terms have been reduced to a single term proportional to $\tilde{V}'(\phi)$.

Demonstrating this with $V(\varphi) = \lambda \varphi^4 / 4 - \mu^2 \varphi^2 / 2$ and $A^2(\varphi) = 1 + \varphi^2 / M^2$ as an example, Eq. (2.25) becomes

$$\Box \varphi = \lambda \varphi^3 - \left(\mu^2 + \frac{M_{\mathrm{P}}^2}{M^2} R \right) \varphi \ , \quad (2.28)$$

and so it initially appears that the mass of the symmetron, in the Jordan frame, is modified in the presence of non-zero R by the non-minimal coupling.

When R is sourced only by matter fields, this is indeed the whole story. At the other extreme, when R is purely dependent on φ, this equation becomes Eq. (2.26), which after a bit of rearrangement is

$$\Box\varphi + \frac{\varphi(\nabla\varphi)^2}{M^2+\varphi^2} + \frac{6M_P^2}{M^2}\frac{\varphi^2\Box\varphi + \varphi(\nabla\varphi)^2}{M^2+\varphi^2} = \lambda\varphi^3 - \mu^2\varphi - \frac{4V_0\varphi + \lambda\varphi^5 - 2\mu^2\varphi^3}{M^2+\varphi^2}\,.$$
(2.29)

The R-containing term has separated into many non-linear terms. Those that contain factors of $\nabla_\mu\varphi$ and $\Box\varphi$, which I have placed on the left-hand side, will not affect the mass of fluctuations around $\bar\varphi$, where $\Box\varphi = \nabla_\mu\varphi = 0$. They will affect the overall evolution of φ, but from Eqs. (2.27a) and (2.27b) we know that the right-hand side is equal to $A^4\frac{d\phi}{d\varphi}\tilde{V}'(\phi)$, so from the Einstein-frame equation of motion we know that the kinetic terms of the left-hand side in fact equal $A^4\frac{d\phi}{d\varphi}\tilde{\Box}\phi$.

The remaining R-derived terms simply correspond to $\mathcal{O}(\varphi^2/M^2)$ contributions to the potential. From Eq. (2.7), $A^4\frac{d\phi}{d\varphi}\tilde{V}'(\phi) \approx A^3\tilde{V}'(\phi)$, and indeed applying this transformation to the right-hand side of Eq. (2.29) gives

$$\left(\lambda\varphi^3 - \mu^2\varphi - \frac{\lambda\varphi^5 - 2\mu^2\varphi^3}{M^2+\varphi^2}\right)\left(1 + \frac{\varphi^2}{M^2}\right)^{-3/2}$$
$$= \lambda\left(1 + \frac{7\bar\varphi^2}{2M^2}\right)\varphi^3 - \mu^2\left(1 + \frac{4V_0}{\mu^2 M^2}\right)\varphi - \frac{5\lambda}{2}\frac{\varphi^2}{M^2}\varphi^3 + \mathcal{O}\left(\frac{\varphi^3}{M^3}\right) \quad (2.30)$$
$$= \lambda\left(1 + \frac{10\bar\varphi^2}{3M^2}\right)\phi^3 - \mu^2\left(1 + \frac{4V_0}{\mu^2 M^2}\right)\phi - 2\lambda\frac{\phi^2}{M^2}\phi^3 + \mathcal{O}\left(\frac{\phi^3}{M^3}\right)$$

which is the derivative of Eq. (2.11).

2.2 One-loop corrections

To compare the size of quantum corrections with the size of the classical terms, including the contributions from non-minimal coupling, we can use the effective action and look at the one-loop corrections.

From here on we will apply our calculations to the Einstein frame, and drop the tilde on $\tilde{V}$[10]. This section will only study the coupling of the scalar field to its own stress–energy. Ideally one should include couplings

_____

[10]Nevertheless, this can work in the Jordan frame (although recall the caveat in Sec. 2.1.2 that the two frames may not be equivalent when it comes to quantum field theory). V should then be taken to be the classical effective potential (that is to say, the non-kinetic

to all matter fields, as these are also explicit in the Einstein frame through $S \supset \int d^4x \sqrt{-g(\varphi)} \mathcal{L}_{\mathrm{m}}$, but such calculations are beyond the scope of this project.

The method to obtain the effective action is as follows [52]: taking mass terms to be part of the interaction and not the free Lagrangian, each possible one-loop Feynman diagram consists of n vertices each contributing $iV''(\varphi)$ to the amplitude, and n lines each contributing a massless propagator. Including also a symmetry factor of $1/2n$ gives the one-loop correction

$$i \int \frac{d^4k}{(2\pi)^4} \sum_{n=1}^{\infty} \frac{1}{2n} \left(\frac{V''}{k^2} \right)^n = \frac{1}{2} \int \frac{d^4k}{(2\pi)^4} \ln \left(1 + \frac{V''}{k^2} \right) . \qquad (2.31)$$

This integral can be performed by Wick-rotating it and using $d^4k = 2\pi^2 k^3 dk$. The integral is divergent, but integrating it up to a cutoff, Λ^{11}, results in

$$\frac{\Lambda^2 V''}{32\pi^2} + \frac{(V'')^2}{64\pi^2} \left(\ln \frac{V''}{\Lambda^2} - \frac{1}{2} \right) . \qquad (2.32)$$

Ideally, the next step would be to add appropriate counterterms to remove the cutoff-dependence, resulting in the initial form of the one-loop-corrected effective potential being

$$V_{1\mathrm{loop}} = V + \frac{\Lambda^2 V''}{32\pi^2} + \frac{(V'')^2}{64\pi^2} \left(\ln \frac{V''}{\Lambda^2} - \frac{1}{2} \right) + \sum \frac{a_n}{n!} \varphi^n , \qquad (2.33)$$

where the sum is over all necessary counterterms, one for each power of φ that appears in Eq. (2.32). The expression is completed by fixing the counterterms, which can usually be achieved by enforcing conditions on $V_{1\mathrm{loop}}^{(n)}(\varphi)$ at some chosen value of φ. For example, we could pick $V_{1\mathrm{loop}}^{(n)}(\bar{\varphi}) = V^{(n)}(\bar{\varphi})$, where $\bar{\varphi}$ is a minimum of $V(\varphi)$, to ensure that we are describing a theory in which the classical equation of motion is accurate around the classical minimum.

As an example, we can consider the φ^4 potential as studied by Coleman and Weinberg [52]. With $\lambda \varphi^4 / 4$, $V''(\varphi) = 3\lambda \varphi^2$ and so Eq. (2.32) is

$$\frac{3\lambda \Lambda^2}{32\pi^2} \varphi^2 + \frac{9\lambda^2}{64\pi^2} \varphi^4 \ln \left(\frac{3\lambda}{\Lambda^2} \varphi^2 \right) - \frac{9\lambda^2}{128\pi^2} \varphi^4 . \qquad (2.34)$$

---

terms in Eq. (2.26)), rather than the true potential that appears in the action, in order to capture the φ-dependence of the non-minimal coupling which only arises at the level of the equations of motion.

[11]Only in this section will Λ refer to an arbitrary cutoff rather than to the mass scale of the chameleon potential.

There are two counterterms, one for φ^2 and one for φ^4. The first can be fixed at $\varphi = \bar{\varphi} = 0$ with $V_{\text{1loop}}^{(2)}(0) = V^{(2)}(0) = 0$, but $V_{\text{1loop}}^{(4)}$ contains a $\ln(\varphi^2)$ term which cannot be analysed at $\varphi = 0$, so the φ^4 counterterm requires some arbitrary scale $m \neq 0$ such that we choose $\lambda(m)$ by taking $V_{\text{1loop}}^{(4)}(m) = V^{(4)}(m)$. Both of these give simple equations that can be solved easily to produce the final one-loop corrected potential,

$$V_{\text{1loop}} = \frac{\lambda}{4}\varphi^4 \left(1 + \frac{9\lambda^2}{16\pi^2} \left[\ln\frac{\varphi^2}{m^2} - \frac{25}{6} \right] \right) \ . \tag{2.35}$$

What makes this work is the fact that we cannot enforce all conditions at $\varphi = \bar{\varphi}$. If we could have $V_{\text{1loop}}^{(n)}(\bar{\varphi}) = V^{(n)}(\bar{\varphi})$ for all applicable n then we would in effect be matching the Taylor series of V_{1loop} with that of V, leading to $V_{\text{1loop}} = V$ (up to a constant, as $n = 0$ receives no counterterm) in the vicinity of $\bar{\varphi}$. That is to say, we would be describing a theory with $V_{\text{1loop}}(\bar{\varphi})$ chosen by us, rather than finding the general V_{1loop} generated by V.

What we will do here instead is take the corrections to be of order $-(V'')^2/128\pi^2$. That this is somewhat sensible can be justified in two ways.

Firstly, regardless of how we fix the counterterms, they serve to remove all dependence on the cutoff Λ and so they must always fully cancel out the first term in Eq. (2.32) which is $\propto \Lambda^2$. Similarly, regardless of what values we fix any $V_{\text{1loop}}^{(n)}(\bar{\varphi})$ to, the $\ln(V''(\varphi)/\Lambda^2)$ in Eq. (2.32) will be countered by the presence of terms that go like $-\ln(V''(\bar{\varphi})/\Lambda^2)$ to leave an overall factor of $\ln(V''(\varphi)/V''(\bar{\varphi}))$ which is negligible for $\varphi \approx \bar{\varphi}$. This leaves only the $-(V'')^2/128\pi^2$ term able to source the one-loop corrections.

Secondly, we should acknowledge that our model is an effective field theory, so the cutoff must have some finite value. We can simply choose the cutoff and directly compare the terms in Eq. (2.32) to those in V without employing counterterms. Choosing $\Lambda^2 = V''(\bar{\varphi})$ again makes the logarithm negligible for $\varphi \approx \bar{\varphi}$, and also makes the two remaining terms in Eq. (2.32) similar in size so we can examine either one of them.

2.2.1 Corrections to the symmetron potential

We shall take as an example here only the symmetry-breaking potential expanded around the Jordan-frame minimum $\bar{\varphi}$, Eq. (2.12),

$$V(\psi) = V_0 - \frac{\mu^4}{4\lambda} + \frac{\mu^4}{\lambda} \left[\left(\frac{\psi}{\bar{\varphi}}\right)^2 + \left(\frac{\psi}{\bar{\varphi}}\right)^3 + \frac{1}{4}\left(\frac{\psi}{\bar{\varphi}}\right)^4 \right] \ , \tag{2.36}$$

and the contributions from non-minimal coupling. Without those contributions, our estimate for the size of the one-loop correction is

$$\frac{(V'')^2}{128\pi^2} = \sum_{n=0}^{4} a_n \mu^4 \left(\frac{\psi}{\bar{\varphi}}\right)^n \qquad (2.37)$$

with $\mathcal{O}(0.1)$ numerical coefficients a_n[12]. The $n = 0$ term is a constant that can be ignored, and an $n = 1$ term shows us that the minimum of the loop-corrected effective potential has been shifted from that of the classical potential. Finally, the $n \geq 2$ terms differ from their counterparts in Eq. (2.12) by factors of $a_n \lambda$ (or $4a_4\lambda$ for $n = 4$), and thus are comparatively small if $\lambda \ll 1/a_n = \mathcal{O}(10)$. This is to be expected: a smaller λ means a smaller probability of vertices and hence loops, so the loops will have a smaller overall effect.

For both $A^2(\phi) \sim 1 + \phi^2/M^2$ and $A^2(\phi) \sim 1 + 2\phi/M$, the non-minimal coupling corrections to the coefficients of ψ^n in Eq. (2.12), with $n > 1$, are respectively of order $(\bar{\varphi}/M)^{2m}$ and $(\bar{\varphi}/M)^m$ with $m > 0$. Therefore, as long as $\bar{\varphi}^2 \ll M^2$ and $\bar{\varphi} \ll M$ respectively, the additional one-loop corrections from $(V'')^2$ are similarly suppressed and this introduces no one-loop corrections more significant than those in Eq. (2.37). This leaves us only to compare the classical non-minimal coupling contributions to the minimally-coupled one-loop corrections.

2.2.2 Corrections to the symmetron model

With $A^2(\phi) \sim 1 + \phi^2/M^2$ and $V_0 = 0$, the leading-order $\bar{\varphi}^2/M^2$ terms found in the $\psi/\bar{\varphi}$, $(\psi/\bar{\varphi})^3$, and $(\psi/\bar{\varphi})^4$ coefficients[13] respectively give the following one-loop–to–non-minimal ratios:

$$\frac{3\mu^4/16\pi^2}{4\mu^6/3\lambda^2 M^2} = \frac{9}{64\pi^2}\frac{\lambda^2 M^2}{\mu^2} \approx \frac{\lambda}{70}\frac{M^2}{\bar{\varphi}^2} \ , \qquad (2.38a)$$

$$\frac{9\mu^4/32\pi^2}{10\mu^6/3\lambda^2 M^2} = \frac{27}{320\pi^2}\frac{\lambda^2 M^2}{\mu^2} \approx \frac{\lambda}{117}\frac{M^2}{\bar{\varphi}^2} \ , \qquad (2.38b)$$

$$\frac{9\mu^4/128\pi^2}{25\mu^6/6\lambda^2 M^2} = \frac{27}{1600\pi^2}\frac{\lambda^2 M^2}{\mu^2} \approx \frac{\lambda}{585}\frac{M^2}{\bar{\varphi}^2} \ . \qquad (2.38c)$$

---

[12]Specifically $a_0 = 1/32\pi^2 \approx 1/316 \approx 0.003$, $a_1 = 3/16\pi^2 \approx 1/53 \approx 0.019$, $a_2 = 3/8\pi^2 \approx 1/26, \approx 0.038$, $a_3 = 9/32\pi^2 \approx 1/35 \approx 0.028$, $a_4 = 9/128\pi^2 \approx 1/140 \approx 0.007$.

[13]There are no contributions to $\psi^2/\bar{\varphi}^2$ before $\bar{\varphi}^4/M^4$.

The $\psi/\bar{\varphi}$ and $(\psi/\bar{\varphi})^2$ terms also have V_0-dependent terms suppressed only by $\bar{\varphi}^2/M^2$[14], and using them in a comparison gives

$$\frac{3\mu^4/16\pi^2}{4V_0\mu^2/\lambda M^2} = \frac{3}{64\pi^2}\frac{\lambda\mu^2 M^2}{V_0} \approx \frac{\lambda}{211}\frac{\mu^2 M^2}{V_0} \; , \tag{2.39a}$$

$$\frac{3\mu^4/8\pi^2}{2V_0\mu^2/\lambda M^2} = \frac{3}{16\pi^2}\frac{\lambda\mu^2 M^2}{V_0} \approx \frac{\lambda}{53}\frac{\mu^2 M^2}{V_0} \; , \tag{2.39b}$$

which provide the same kind of ratios as Eq. (2.38) when $|V_0| \sim \mu^4/\lambda$.

Thus, for the non-minimal coupling terms to dominate over quantum ones, we require not only that $\lambda \ll \mathcal{O}(10)$, but that $\lambda \ll \mathcal{O}(10)\bar{\varphi}^2/M^2$. Recall that we also need $\bar{\varphi}^2/M^2 \ll 1$ for the non-minimal coupling contributions to *not* dominate over the bare potential $\lambda\varphi^2/4 - \mu^2\varphi^2/2$. Combining these bounds,

$$\frac{\mu^2}{M^2} \ll \lambda \ll \frac{\mu}{M} \tag{2.40}$$

is the condition under which we can trust the minimally-coupled classical theory to provide a valid approximation to the full dynamics. Its validity given a particular solution can be further limited with $\tilde{\psi}^3/\bar{\varphi}^3 \gg \bar{\varphi}^2/M^2$ from Eq. (2.13), a bound which ensures that the minimum of the Einstein-frame scalar field can be taken as that of the Jordan-frame field at $\bar{\varphi} = \mu/\sqrt{\lambda}$, $\tilde{\psi} = 0$.

As the symmetron has been a popular subject of phenomenology, we may compare Eq. (2.40) to regions of the symmetron parameter space studied in previous works in order to determine how applicable any constraints obtained therein actually are. Useful for this is Fig. 24 of Ref. [25], which shows bounds on the symmetron parameters M and λ from atom interferometry, Eöt-Wash experiments, and astrophysics. The astrophysics constraints are independent of μ but are relevant for M from just below 10^{15} to above 10^{20} GeV and constrain λ no greater than around 10^{-45}; Eq. (2.40) tells us that they are in fact trustworthy as long as $\mu \gg \lambda M$[15], which is never larger than 10^{-21} eV. Conversely, the interferometry and Eöt-Wash constraints exclude only regions of $\mu \in [10^{-5}, 10^{-2}]$ eV for $M \in [1, 10^5]$ GeV, giving a maximum $\{\mu^2/M^2, \mu/M\}$ of $\{10^{-4}, 10^{-2}\}$ and a minimum of $\{10^{-14}, 10^{-7}\}$, providing far narrower ranges of λ than depicted in the figure.

---

[14]V_0-dependent contributions for higher powers of $\psi/\bar{\varphi}$ are further suppressed.
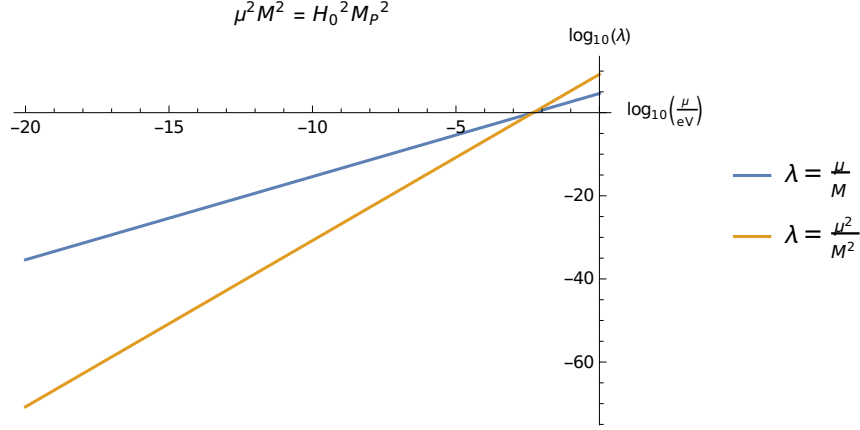
[15]And also $\mu \ll M$.

Figure 5: Bounds of applicable λ given Eq. (2.40) and a symmetron with $\mu^2 M^2 \sim H_0^2 M_{\mathrm{P}}^2$, with lines obtained by setting $\mu^2 M^2 = H_0 M_{\mathrm{P}}^2$ and approximating H_0 as 10^{-32} eV. The applicable region must be where $\mu/M > \mu^2/M^2$, and as the lines intersect when $\mu^2 = H_0 M_{\mathrm{P}}$, this requires $\mu \lesssim 4.9 \times 10^{-3}$ eV.

We may also consider symmetrons obeying the cosmologically-motivated relationship, $\mu^2 M^2 \sim H_0^2 M_{\mathrm{P}}^2$, as described in Sec. 1.3.1. This relationship gives $M \sim H_0 M_{\mathrm{P}}/\mu$, and therefore $\{\mu^2/M^2, \mu/M\} \sim \{\mu^4/H_0^2 M_{\mathrm{P}}^2, \mu^2/H_0 M_{\mathrm{P}}\}$. These bounds are illustrated in Fig. 5.

2.2.3 Corrections to the symmetron-like chameleon model

With $A^2(\phi) \sim 1 + 2\phi/M$ and $V_0 = 0$, the leading-order $\bar{\varphi}^2/M^2$ terms found in the $\psi/\bar{\varphi}$, $(\psi/\bar{\varphi})^2$, $(\psi/\bar{\varphi})^3$, and $(\psi/\bar{\varphi})^4$ coefficients respectively give the following one-loop–to–non-minimal ratios:

$$\frac{3\mu^4/16\pi^2}{(\sqrt{6}-1)\mu^5/\lambda^{3/2}M} = \frac{3}{16(\sqrt{6}-1)\pi^2}\frac{\lambda^{3/2}M}{\mu} \approx \frac{\lambda}{76}\frac{M}{\bar{\varphi}} \ , \qquad (2.41\mathrm{a})$$

$$\frac{3\mu^4/8\pi^2}{(8\sqrt{6}+7)\mu^5/2\lambda^{3/2}M} = \frac{3}{4(8\sqrt{6}+7)\pi^2}\frac{\lambda^{3/2}M}{\mu} \approx \frac{\lambda}{350}\frac{M}{\bar{\varphi}} \ , \qquad (2.41\mathrm{b})$$

$$\frac{9\mu^4/32\pi^2}{(16\sqrt{6}+9)\mu^6/2\lambda^{3/2}M} = \frac{9}{16(16\sqrt{6}+9)\pi^2}\frac{\lambda^{3/2}M}{\mu} \approx \frac{\lambda}{846}\frac{M}{\bar{\varphi}} \ , \qquad (2.41\mathrm{c})$$

$$\frac{9\mu^4/128\pi^2}{5(2\sqrt{6}+1)\mu^5/2\lambda^{3/2}M} = \frac{9}{320(2\sqrt{6}+1)\pi^2}\frac{\lambda^{3/2}M}{\mu} \approx \frac{\lambda}{2070}\frac{M}{\bar{\varphi}} \ . \qquad (2.41\mathrm{d})$$

32

The $\psi/\bar{\varphi}$ term also has a V_0-dependent term suppressed only by $\bar{\varphi}/M$, and using this[16] in a comparison gives

$$\frac{3\mu^4/16\pi^2}{4\sqrt{6}V_0\mu/\lambda^{1/2}M} = \frac{3}{64\sqrt{6}\pi^2}\frac{\lambda^{1/2}\mu^3 M}{V_0} \approx \frac{\lambda^{1/2}}{515}\frac{\mu^3 M}{V_0} \ , \tag{2.42}$$

which provides the same kind of ratios as Eq. (2.41) when $|V_0| \sim \mu^4/\lambda$.

Thus, for the non-minimal coupling terms to dominate over quantum ones, we require not only that $\lambda \ll \mathcal{O}(10)$, but that $\lambda \ll \mathcal{O}(10)\bar{\varphi}/M$. Recall that we also need $\bar{\varphi}/M \ll 1$ for the non-minimal coupling contributions to *not* dominate over the bare potential $\lambda\varphi^2/4 - \mu^2\varphi^2/2$. Combining these bounds,

$$\frac{\mu^2}{M^2} \ll \lambda \ll \frac{\mu^{2/3}}{M^{2/3}} \tag{2.43}$$

is the condition under which we can trust the minimally-coupled classical theory to provide a valid approximation to the full dynamics. Its validity given a particular solution can be further limited with $\tilde{\psi}^3/\bar{\varphi}^3 \gg \bar{\varphi}/M$ from Eq. (2.21), a bound which ensures that the minimum of the Einstein-frame scalar field can be taken as that of the Jordan-frame field at $\bar{\varphi} = \mu/\sqrt{\lambda}$, $\tilde{\psi} = 0$.

2.3 Conclusions

In this section we have calculated or estimated the contributions from non-minimal gravitational couplings and one-loop quantum corrections to modified theories of gravity in which the fifth force is screened due to non-linearities in the bare potential. Through this, we have obtained bounds on model parameters for models with the symmetry-breaking potential of Eq. (2.10). For a self-coupling constant λ and a non-minimal coupling term $\sim \varphi^n/M^n$, the bare potential dominates over contributions from the non-minimal coupling as long as $\bar{\varphi}^n/M^n \ll 1$, and the one-loop corrections are weaker still as long as $\lambda \ll \bar{\varphi}^n/M^n$. When rewritten in terms of the mass scale μ instead of the minimum $\bar{\varphi}$, these give bounds on λ, which we provide in Eq. (2.40) for $n = 2$ and Eq. (2.43) for $n = 1$.

From here on we will always consider choices of parameters such that the conditions of Eq. (2.40) or Eq. (2.43) are satisfied, and that we no longer need to distinguish between the Jordan and Einstein frames.

---

[16]There is no contribution to any $\psi^n/\bar{\varphi}^n$ term before $\bar{\varphi}^n/M^n$, so only $\psi/\bar{\varphi}$ is useful here.

3 Non-Linearities in Black Hole Superradiance

Having established the conditions of Eqs. (2.40) and (2.43) under which the minimally-coupled classical equations of motion hold, we can move on to estimating both when and how non-linearities will affect scenarios of interest for tests of screened fifth forces.

In this section, the scenario under consideration is the superradiant instability of uncharged scalar fields around Kerr black holes, hereafter referred to as 'black hole superradiance' without further qualification. In Section 3.1.1 I will provide definitions for the terms and symbols used for discussing Kerr black holes, and in Section 3.1.2 I will provide an overview of what superradiance is and how it has been previously applied to obtain constraints on scalar fields. Then, Section 3.2 will show that non-linearities are expected to affect the process of black hole superradiance, and finally Section 3.3 will apply a method previously used for axion-like fields to determine how the effects of non-linearities in the symmetron and chameleon theories will differ from those in models of axions.

3.1 Black hole superradiance

3.1.1 Kerr black holes

A Kerr black hole is a vacuum solution to the Einstein field equations Eq. (1.1) given (in Boyer–Lindquist coordinates) by

$$ds^2 = -\frac{\Delta - a^2 \sin^2\theta}{\Sigma}dt^2 - \frac{2ar_{\mathrm{s}}r\sin^2\theta}{\Sigma}dtd\phi + \frac{\Sigma}{\Delta}dr^2 + \Sigma d\theta^2 + \frac{\Gamma}{\Sigma}d\phi^2 \quad (3.1)$$

where

$$\Delta = r^2 + a^2 - r_{\mathrm{s}}r \ , \tag{3.2a}$$

$$\Sigma = r^2 + a^2 \cos^2\theta \ , \tag{3.2b}$$

$$\Gamma = (r^2 + a^2)^2 - \Delta a^2 \sin^2\theta \ , \tag{3.2c}$$

$$r_{\mathrm{s}} = 2GM_{\mathrm{H}} \ , \tag{3.2d}$$

and M_{H} is the mass of the black hole and its angular momentum is aM_{H}.

Two important regions of the Kerr black hole are the outer event horizon and the ergoregion. The event horizons, surfaces from inside which no
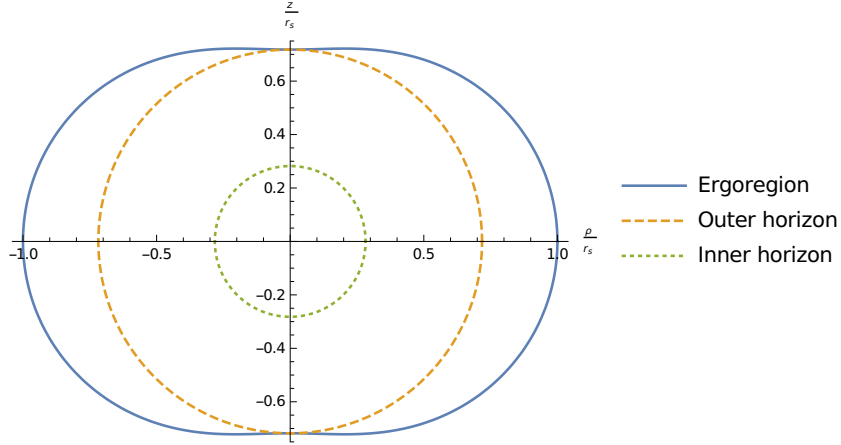
Figure 6: Surfaces of the Kerr metric in coordinates $(\rho, z) = r(\sin\theta, \cos\theta)$ for $a = 0.45 r_\mathrm{s}$: the surface of the ergoregion (blue, solid), the outer event horizon (orange, dashed), and the inner event horizon (green, dotted).

particles can escape, at $r_\pm$ are the solutions to

$$g_{rr} \to \infty \Rightarrow \Delta = 0 \Rightarrow r_\pm = \frac{1}{2}\left(r_\mathrm{s} \pm \sqrt{r_\mathrm{s}^2 - 4a^2}\right) \ , \qquad (3.3)$$

from which it can be seen that the maximum value of a is $r_\mathrm{s}/2 = GM_\mathrm{H}$. The ergoregion, a volume outside the horizon inside which no particles can remain stationary, is given by $r_+ < r < r_\mathrm{ergo}$ where r_ergo is the larger solution to

$$g_{tt} = 0 \Rightarrow \Delta = a^2 \sin^2\theta \Rightarrow r_\mathrm{ergo} = \frac{1}{2}\left(r_\mathrm{s} + \sqrt{r_\mathrm{s}^2 - 4a^2 \cos^2\theta}\right) \ . \qquad (3.4)$$

The radii at which these surfaces occur for an example of $a = 0.45 r_\mathrm{s}$ are shown in Fig. 6.

3.1.2 Superradiance

Superradiance is a phenomenon whereby waves are amplified upon interaction with a dissipative medium that is moving faster than the phase velocity of the waves. In superradiance around a Kerr black hole, the ergoregion behaves as the dissipative 'medium', as the energy of a wave or particle within the ergoregion can become negative for a stationary external observer [53].

36

Black hole superradiance is equivalent to the Penrose process, whereby classical particles, rather than waves, similarly gain kinetic energy from a Kerr black hole [54].

The condition that a wave must satisfy to undergo superradiant amplification is [53]

$$\omega < m\Omega_{\mathrm{H}} \ , \tag{3.5}$$

where ω is the frequency of the wave and m is its azimuthal number with respect to the black hole-centred coordinates of Eq. (3.1), such that in said coordinates the wave behaves as $e^{-i\omega t + im\phi}$, and

$$\Omega_{\mathrm{H}} = - \left. \frac{g_{t\phi}}{g_{\phi\phi}} \right|_{r=r_+} = \frac{a}{r_{\mathrm{s}} r_+} \tag{3.6}$$

is the angular velocity of the black hole; that is, the angular velocity, on the equator of the outer event horizon, of an object with zero angular momentum.

If the waves are trapped in the vicinity of the black hole—for instance, when a field has mass then its waves are able to form bound states around the black hole—then the waves are continually amplified and a 'cloud' of particles grows exponentially around the black hole until enough angular momentum has been extracted from the hole that the condition Eq. (3.5) is no longer satisfied [53].

As we will see in Sec. 3.3, waves in orbit of a black hole obey a classical equation of motion which has a similar form to the Schrödinger equation for a hydrogen atom, so they will behave analogously to electrons in atomic orbitals in that they will have discrete energy levels whose energy increases with the orbital radius. One might therefore expect that superradiance is maximised for fields where the lowest-energy modes have an average orbital radius close to the ergoregion, in order to be amplified, but outside the event horizon, so as to not fall in; this requires the Compton wavelength to be of order the Schwarzschild radius of the black hole, which indeed has been found to be the case [55, 56]. Observations of black hole superradiance, either by detecting nearly monochromatic gravitational wave emission (gravitons being produced when particles transition between energy levels, and when pairs of uncharged particles annihilate) or by noting an absence of high-spin black holes with certain masses, would therefore provide not only evidence for a new field but also an approximate measurement of its mass [57, 58]. Searches for black hole superradiance can thereby probe any theory which introduces

new light degrees of freedom, because all fields feel the gravity of black holes and are thus subject to the process.

Here I shall consider only the case of an uncharged scalar field around a single Kerr black hole. For this case, constraints from black hole mass and spin measurements have been obtained over the last few years in e.g., [59–67], while constraints from the non-observation of gravitational wave signatures were made in 2019 from LIGO data [68, 69]. Many analyses of superradiance even for this case have only considered the linearised limit Eq. (1.4) of scalar field theories, taking the potential of the scalar field to have the form $\frac{1}{2}\mu_\varphi^2\varphi^2$, both for studying the phenomenon in general [54–56, 70, 71] and for deriving constraints on scalar masses from observations of black holes [57–59, 64, 68, 72–78]. Some focus on 'non-linearities' in fact refers to non-linear terms that result from interactions with additional fields rather than a more complicated potential [79]. Even in the context of scalar–tensor gravity, studies of superradiance have made use only of quadratic potentials, and the non-minimal coupling between the scalar field and the curvature is taken to manifest only in the form of a coupling to surrounding matter in the Einstein frame [80, 81]. Otherwise, studies of black hole superradiance in modified gravity have considered modifications made to the Kerr metric, but the fields undergoing superradiance have only come from the simple model of Eq. (1.4) rather than the degrees of freedom of the modified gravity theories themselves [82–84].

Studies of the effects of non-linearities from the potential have instead primarily focused on axions and axion-like particles, which for the purposes of superradiance are either scalars or pseudoscalars (parity does not come into the calculations) with a periodic potential such as

$$V(\varphi) = \mu^2 f^2 \left[1 - \cos\left(\frac{\varphi}{f}\right)\right] = \frac{1}{2}\mu^2\varphi^2 - \frac{1}{24}\frac{\mu^2}{f^2}\varphi^4 + \mathcal{O}\left(\frac{\varphi^4}{f^4}\right) \ . \qquad (3.7)$$

Only the leading-order non-linearity in Eq. (3.7) is necessary to obtain the results described throughout this section, with the sign of the term being the most important for a qualitative understanding. Early papers identified two effects of the $-\varphi^4$ non-linearity on the progress of black hole superradiance. One of these is the *bosenova*, where self-interactions cause the axion cloud to collapse and release a burst of gravitational radiation [85–88].

Bosenovae were first predicted as a phenomenon that can be induced in Bose–Einstein condensates by adjusting the strength of the self-coupling between a fixed number of particles [89]; in the context of superradiance, they

come from an increase in particle number. They slow down the exponential growth of the cloud, but also provide an additional gravitational wave signature as the cloud collapses [85].

The second effect is level mixing or mode mixing, where self-interactions transfer energy to non-superradiant modes and thereby inhibit the growth of the superradiant instability [85, 87]. Early numerical simulations showed the effects of level mixing to generally be weak, failing to prevent the cloud from growing to the point where a bosenova occurs [87, 88], and consequently many attempts to derive constraints on axion-like fields (and, in one case, constraints on primordial black holes by using pions [90]) from superradiance acknowledged or accounted for bosenovae in analyses that are otherwise based on linearised models of a scalar field [60–63, 65–67, 69, 90–94].

2019 and 2020 saw a few papers that, noting how numerical simulations suffered from a large hierarchy between the timescale of the evolution of the scalar field and the time for a bosenova to occur, aimed to deal with non-linearities more accurately, and with applicability to more scalar field theories than those of axion-like particles [95–97]. Baryakhtar *et al.* determined that particle emission and coupling between modes will generally suppress superradiant growth such that a bosenova will not occur [95]; however, Omiya *et al.* then claimed that the Baryakhtar paper is flawed by its adherence to a perturbative treatment of level mixing and that its results are therefore inconclusive [97].

The topic of non-linearities in black hole superradiance, and whether non-perturbative effects such as bosenovae are relevant to the process, is therefore still a developing field as of the time of writing. I will not attempt here to resolve the issue myself. Instead, upon confirming in Section 3.2 that non-linear effects do indeed become important for screened scalar fields, I will then in Section 3.3 go through a nonrelativistic calculation that has been previously used to justify the occurrence of bosenovae for axion-like particles and see whether it predicts anything different in terms of phenomenology when applied to other theories, in particular to the symmetron and chameleon models.

A useful quantity that often appears throughout the topic of black hole superradiance is the gravitational coupling α between a black hole of mass M_{H} and a particle of mass μ_φ, $\alpha = GM_{\mathrm{H}}\mu_\varphi$. Previous work has shown that superradiance occurs at its fastest rate for $\alpha = \mathcal{O}(1)$, specifically $\alpha \approx 0.42$ for a linearised field around a near-extremal black hole (and slightly lower values
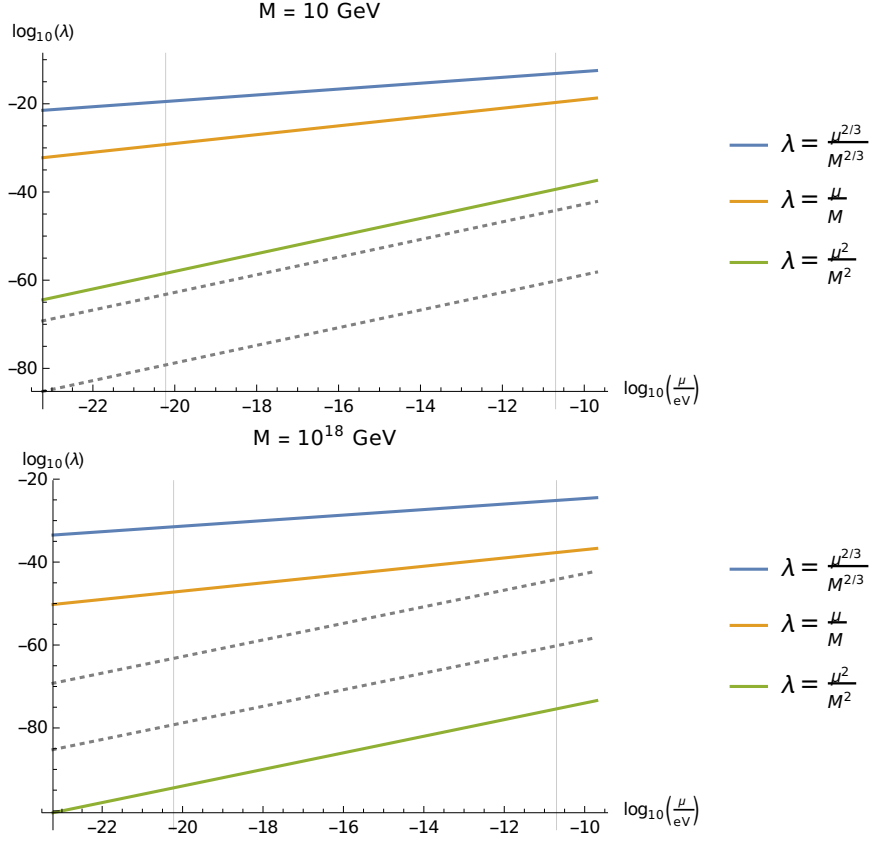
Figure 7: Plots comparing the region of parameter space depicted in Figs. 7 and 8 of Ref. [95] (marked with dotted lines) with the bounds of Eqs. (2.40) and (2.43) (marked with solid diagonal lines), for $M = 10$ GeV (top) and $M = 10^{18}$ GeV (bottom). The thin vertical lines mark μ such that $\alpha = 0.45$ (the right-hand edge of the figures of Ref. [95]) for a supermassive black hole of mass $M_{\mathrm{H}} = 10^{10}\ M_\odot$ (left) and a stellar-mass black hole of mass $M_{\mathrm{H}} = 3\ M_\odot$ (right) respectively. For the larger value of M we can see that the entire parameter space is included within both Eqs. (2.40) and (2.43); for the smaller value, it all falls into $\lambda \ll \mu^2/M^2$ and so non-minimal coupling contributions will dominate over the bare potential.

for lower angular momenta) [55,56], so we can treat α as a conversion constant relating μ_φ and M_{H}: any given black hole mass will be most sensitive to one particular scalar mass, and any given scalar mass will undergo the fastest

superradiance around one particular black hole mass.

For reference, Fig. 7 shows how the parameter space of Figs. 7 and 8 of Ref. [95], throughout the entirety of which it is calculated that non-perturbative effects do not occur, compares to the bounds of Eqs. (2.40) and (2.43), in which we can trust that the symmetron and symmetron-like chameleon equations of motion are close enough to the classical $\Box\varphi = \lambda\varphi^3 - \mu^2\varphi$ that our results are relevant. For large M (e.g., 10^{18} GeV) the classical equation of motion is trustworthy, but for small M (e.g., 10 GeV) $\lambda \ll \mu^2/M^2$ so non-minimal coupling contributions will dominate over the bare potential.

3.2   Initial fluctuations

First we must confirm that non-linearities will influence the process of black hole superradiance at all. Nonlinear effects are usually insignificant when small fluctuations $\psi = \varphi - \bar{\varphi}$ around a minimum $\bar{\varphi}$ of the effective potential are much smaller than $\bar{\varphi}$. That is to say, ψ behaves like a massive linearised field $\Box\varphi = \mu_\varphi^2\varphi$, and as it grows with superradiance it may eventually reach $\psi \approx \bar{\varphi}$, by which point the non-linear terms in its equation of motion become important. It may be the case that the linearised approximation $\Box\varphi = \mu_\varphi^2\varphi$ breaks down before this point, with one candidate to cause this breakdown being the perturbative level mixing effects of Ref. [95], but the onset of non-perturbative effects when $\psi \approx \bar{\varphi}$ will at least provide a definite upper bound for the timescale on which the breakdown will occur.

In linearised analyses of superradiance, the scalar field grows exponentially with time, i.e., $\varphi(t) = \varphi(0)e^{t/\tau}$ for some instability timescale τ that is no less than $\mathcal{O}(1-100)(M_{\mathrm{H}}/M_\odot)$ seconds [55,80]. We therefore expect that non-linear terms will become important after no more time than

$$t_{\mathrm{crit}} = \tau \ln\left(\frac{\bar{\varphi}}{\psi_0}\right) \;, \tag{3.8}$$

where ψ_0 is the size of the initial fluctuation in the scalar field, assuming the background value is $\bar{\varphi}$. We can estimate this size by taking the fluctuation to be a single particle, with its potential energy being equal to its mass μ_φ. When it forms a bound state with a black hole, it is spread over a volume of order the Schwarzschild radius, $2\alpha/\mu_\varphi \approx 1/\mu_\varphi$, cubed and so we can express the approximate mass density of the fluctuation as μ_φ^4. An estimate for the value of ψ_0 then comes by solving

$$V(\psi_0) = \mu_\varphi^4 \;. \tag{3.9}$$

41

The Schwarzschild radius is an underestimate of the scale involved (as will be shown in the next section, the Bohr radius $(\alpha\mu_\varphi)^{-1}$ might be a better choice), but we are interested in finding the largest value of ψ_0 outside the event horizon and therefore we can afford to overestimate the density.

For a field with only a mass term in the potential, which we expect to be a suitable approximation when $\psi_0 \ll \bar\varphi$, Eq. (3.9) is easily solved.

$$\frac{1}{2}\mu_\varphi^2\psi_0^2 = \mu_\varphi^4 \Rightarrow \psi_0 = \sqrt{2}\mu_\varphi \qquad (3.10)$$

3.2.1 Symmetrons

Writing the symmetron potential as a function of ψ as in Eq. (2.12) makes it apparent that non-linearities are indeed suppressed when $\psi_0 \ll \bar\varphi$ such that Eq. (3.10) is a sensible approximation to use. Because $\mu_\varphi = \sqrt{2}\mu$ and $\bar\varphi = \mu/\sqrt{\lambda}$, the number of e-foldings required for ψ to reach $\bar\varphi$ is

$$\frac{t_{\mathrm{crit}}}{\tau} = \frac{1}{2}\ln\left(\frac{\bar\varphi^2}{\psi_0^2}\right) \sim \frac{1}{2}\ln\left(\frac{1}{4\lambda}\right) \ . \qquad (3.11)$$

Substituting $\sqrt{2}\mu = \mu_\varphi = \alpha/GM_{\mathrm{H}} = 8\pi\alpha M_{\mathrm{P}}^2/M_{\mathrm{H}}$ into the bounds of Eq. (2.40) tells us that, in order for us to both detect symmetrons via black hole superradiance and have any trust in the theory, we need

$$\frac{64\pi^2\alpha^2}{2}\frac{M_{\mathrm{P}}^4}{M^2 M_{\mathrm{H}}^2} \lesssim \lambda \lesssim \frac{8\pi\alpha}{\sqrt{2}}\frac{M_{\mathrm{P}}^2}{M M_{\mathrm{H}}} \qquad (3.12)$$

such that

$$\frac{\sqrt{2}}{64\pi\alpha}\frac{M_{\mathrm{H}}}{M_{\mathrm{P}}}\frac{M}{M_{\mathrm{P}}} \lesssim \frac{\bar\varphi^2}{\psi_0^2} \lesssim \frac{1}{128\pi^2\alpha^2}\frac{M_{\mathrm{H}}^2}{M_{\mathrm{P}}^2}\frac{M^2}{M_{\mathrm{P}}^2} \ . \qquad (3.13)$$

Nonlinear effects will become important if the resulting number of e-foldings, given by Eq. (3.11), is smaller than that required for superradiance to end, which happens when enough angular momentum has been extracted from the black hole for the condition $\omega < m\Omega_H$ to no longer hold. The number of bosons N at the end of superradiance can be obtained by equating their total angular momentum, Nm (assuming most particles are in the same state), with the change in the black hole's angular momentum, $\Delta a M_{\mathrm{H}}$ (assuming the change in mass is negligible). This gives N at this end point as [72, 91]

$$N = \frac{\Delta a M_{\mathrm{H}}}{m} \le \frac{1}{8\pi}\frac{M_{\mathrm{H}}^2}{M_{\mathrm{P}}^2} \qquad (3.14)$$

since $\Delta a \leq GM_H$ and $m \geq 1$. This is larger than the lower bound for $\bar{\varphi}^2/\psi_0^2$ by a factor of order M_H/M, and thus requires of order $\ln(M_H/M)$ additional e-foldings to reach, which is large for $M_H \gtrsim M_\odot \gg M_P \gtrsim M$; for instance $\ln(M_\odot/M_P) \approx \ln(4.6 \times 10^{38}) \approx 89$. It is also larger than the upper bound for $\bar{\varphi}^2/\psi_0^2$ by a factor of order M_P^2/M^2. So the time until superradiance would end for a scalar field with a linear equation of motion is longer than the time until the symmetron stops behaving like a scalar field with a linear equation of motion.

For any of the preceding comparisons to matter, these e-foldings must also take a small enough time so as to occur within the lifetime of our universe. For this it will be helpful to express Eq. (3.11) via Eq. (3.13) as

$$\frac{1}{2} \ln \left(10^{37} \frac{M_H}{M_\odot} \frac{M}{M_P} \right) \lesssim \frac{t_{\text{crit}}}{\tau} \lesssim \frac{1}{2} \ln \left(10^{75} \frac{M_H^2}{M_\odot^2} \frac{M^2}{M_P^2} \right) \ . \tag{3.15}$$

Although we have not calculated what τ is for the symmetron, as our concern is with the failure of linearity we shall estimate it to be of similar order to the timescales obtained in previous superradiance studies i.e., $\tau = \mathcal{O}(1-100)(M_H/M_\odot)$ seconds [55,80]. On the upper bound of Eq. (3.15), for a supermassive black hole of 10^{10} solar masses—the largest from which superradiance constraints have so far been obtained [66,67]—and a large coupling constant $M = M_P$, it takes $t_{\text{crit}}/\tau = 110$ e-foldings, and with an instability timescale of $\tau = 100$ seconds per solar mass, the resulting time is around 3.5 million years. On the lower bound, and for a black hole of three solar masses—which LIGO and Virgo use as the minimum mass required to count an event as an unambiguous black hole detection [98]—given $M = 1$ GeV and $\tau = 1$ s, non-linear effects could become important within $t_{\text{crit}}/\tau = 22$ e-foldings or $t_{\text{crit}} = 66$ seconds.

In conclusion, it is certainly necessary to take into account non-linear terms when analysing symmetron superradiance.

3.2.2 Chameleons

The minimally-coupled chameleon potential of $V(\varphi) = \Lambda^5/\varphi$ does not have a finite $\bar{\varphi}$, so we shall examine an effective potential, with a non-zero density ρ, as in Eq. (1.24),

$$V_{\text{eff}}(\varphi) = \frac{\Lambda^5}{\varphi} + \frac{\rho}{M} \varphi \ . \tag{3.16}$$

43

In the context of black hole superradiance, ρ may be the density of the medium surrounding the black hole.

Although the chameleon effective potential is typically derived for the Einstein frame, the matter term also arises indirectly in the Jordan frame when ρ is the Jordan-frame density. This is because the equation of motion for φ contains the non-minimal coupling term $-M_{\mathrm{P}}^2 A(\varphi) A'(\varphi) R$, from which the matter term in the effective potential can be obtained by using a chameleon coupling function $A(\varphi) \sim 1 + \varphi/M$ and the trace of the gravitational equations (neglecting the variation and stress–energy of the chameleon itself) $-M_{\mathrm{P}}^2 A(\varphi)^2 R = T \simeq \rho$.

The bounds on the validity of this potential are less general than those on the symmetron in Eq. (2.40) or on the symmetron-like chameleon in Eq. (2.43). As mentioned in Section 2.1.2, the contributions from non-minimal coupling in Eq. (2.19) have model-dependent coefficients, although if these remain small enough that the matter coupling remains approximately linear then we can still expect the leading-order contribution to be small compared to the matter coupling as long as $\rho \gg \Lambda^5/M$ (if Eq. (3.16) is defined in the Einstein frame; if it is in the Jordan frame then only $\rho \gg \Lambda^5 M/M_{\mathrm{P}}^2$ is needed). Additionally, we cannot compute the one-loop corrections for the bare potential in vacuum.

This effective potential expanded around $\bar{\varphi}$ is

$$V(\psi) = \sum_{n>1} (-1)^n \Lambda^5 \frac{\psi^n}{\bar{\varphi}^{n+1}} \; . \qquad (3.17)$$

The $(n+1)^{\mathrm{th}}$ term becomes equal in size to the nth, for all n, when $\psi = \bar{\varphi}$.

If the effective potential is valid then Eq. (3.10) might be a good approximation, with

$$\mu_\varphi^2 = \frac{2\Lambda^5}{\bar{\varphi}^3} \Rightarrow \frac{\bar{\varphi}}{\psi_0} = \frac{1}{2^{1/6}} \left(\frac{\Lambda}{\mu_\varphi} \right)^{5/3} \; . \qquad (3.18)$$

Using $\mu_\varphi = \alpha/GM_{\mathrm{H}}$, $\bar{\varphi}/\psi_0 \approx (GM_{\mathrm{H}}\Lambda)^{5/3}$, so Eq. (3.8) gives

$$\frac{t_{\mathrm{crit}}}{\tau} = \frac{5}{3} \ln \left(\frac{1}{8\pi\alpha} \frac{\Lambda M_{\mathrm{H}}}{M_{\mathrm{P}}^2} \right) \approx \frac{5}{3} \ln \left(10^{37} \frac{M_{\mathrm{H}}}{M_\odot} \frac{\Lambda}{M_{\mathrm{P}}} \right) \; . \qquad (3.19)$$

This is almost identical to the symmetron lower bound, except for depending on Λ rather than M and having a factor of $5/3$ rather than $1/2$, and in that there is an equals sign whereas the symmetron has a pair of bounds. A

requirement of $\mathcal{O}(10)$ e-foldings is still to be expected; for instance, with $M_\mathrm{H} = 3M_\odot$ and Λ as the dark energy scale 2.4 meV, Eq. (3.19) gives $t_\mathrm{crit} \approx 29\tau$.

Also of note is that the mass μ_φ can be expressed in terms of Λ, ρ, and M, namely $(\rho^3/\Lambda^5 M^3)^{1/4}$. The condition under which $\psi_0 \ll \bar{\varphi}$ is therefore $\rho \ll \Lambda^3 M$; this is easily compatible with $\rho \gg \Lambda^5/M$, the condition for non-minimal coupling effects to be negligible, as long as $\Lambda^2 \ll M^2$.

The chameleon with a symmetron-like potential of Eq. (1.25) can be analysed in a manner more similar to the symmetron; the only relevant difference is that the power on μ/M in the upper bound of Eq. (2.43) is $2/3$ rather than 1. The equivalent of Eq. (3.13) is therefore

$$\left(\frac{\sqrt{2}}{64\pi\alpha}\frac{M_\mathrm{H}}{M_\mathrm{P}}\frac{M}{M_\mathrm{P}}\right)^{2/3} \lesssim \frac{\bar{\varphi}^2}{\psi_0^2} \lesssim \frac{1}{128\pi^2\alpha^2}\frac{M_\mathrm{H}^2}{M_\mathrm{P}^2}\frac{M^2}{M_\mathrm{P}^2} \,, \tag{3.20}$$

and the superradiance-saturating particle number N given by Eq. (3.14),

$$N = \frac{\Delta a M_\mathrm{H}}{m} \leq \frac{1}{8\pi}\frac{M_\mathrm{H}^2}{M_\mathrm{P}^2} \,,$$

is larger than the lower bound for $\bar{\varphi}^2/\psi_0^2$ by a factor $\sim (M_\mathrm{H}^2/MM_\mathrm{P})^{2/3}$, and thus requires of order $\frac{2}{3}\ln(M_\mathrm{H}^2/MM_\mathrm{P})$ additional e-foldings to reach. This is large for $M_\mathrm{H} \gtrsim M_\odot \gg M_\mathrm{P} \gtrsim M$; for instance $\frac{2}{3}\ln(M_\odot^2/M_\mathrm{P}^2) \approx \frac{4}{3}\ln(4.6 \times 10^{38}) \approx 119$. As in the case of the symmetron, it is also larger than the upper bound for $\bar{\varphi}^2/\psi_0^2$ by a factor of order M_P^2/M^2. So the time until superradiance would end for a scalar field with a linear equation of motion is longer than the time until the symmetron-like chameleon stops behaving like a scalar field with a linear equation of motion.

Likewise, the equivalent of the symmetron's Eq. (3.15) is

$$\frac{1}{3}\ln\left(10^{37}\frac{M_\mathrm{H}}{M_\odot}\frac{M}{M_\mathrm{P}}\right) \lesssim \frac{t_\mathrm{crit}}{\tau} \lesssim \frac{1}{2}\ln\left(10^{75}\frac{M_\mathrm{H}^2}{M_\odot^2}\frac{M^2}{M_\mathrm{P}^2}\right) \,, \tag{3.21}$$

where the only difference from Eq. (3.15) is that the coefficient on the lower bound has been multiplied by a factor of $2/3$. This changes the minimum possible timescale for the onset of non-linear behaviour, for a black hole of three solar masses given $M = 1$ GeV and $\tau = 1$ s, from 66 seconds to 44.

In conclusion, non-linear terms are just as important when the matter coupling has been changed to a linear function of φ.

3.3 Nonrelativistic energies

The effects of the non-linear terms in the potential can be estimated by making a nonrelativistic approximation and looking for extrema of the energy. This has previously been done for axion-like fields with a perioidic potential [85, 86], so after reviewing the general case, we'll look at those as an example before moving back to models of screened fifth forces.

There are five steps to the process: expand the Lagrangian around the minimum of the potential, split up the $(\nabla\varphi)^2 = (\nabla\psi)^2$ term in the Lagrangian into $g^{tt}\dot{\psi}^2 + g^{ij}\partial_i\psi\partial_j\psi$ (where i, j runs over the spatial indices), choose the appropriate $g_{\mu\nu}$, decompose ψ in such a way that a nonrelativistic limit can be taken, and obtain the resulting expression for the energy.

The first two steps give

$$\mathcal{L} = -\frac{1}{2}g^{tt}\dot{\psi}^2 - \frac{1}{2}g^{ij}\partial_i\psi\partial_j\psi - V(\psi) , \qquad (3.22)$$

and then, describing gravity by taking a small perturbation of the metric to be $-g_{tt} = 1 + 2\Phi$, where $\Phi \ll 1$ is the Newtonian gravitational potential, gives

$$-\frac{1}{2}g^{tt}\dot{\psi}^2 \approx \frac{1}{2}\dot{\psi}^2 - \Phi\dot{\psi}^2 . \qquad (3.23)$$

Next, the decomposition of ψ is

$$\psi = \frac{1}{\sqrt{2\mu_\varphi}}\left(\chi e^{-i\mu_\varphi t} + \chi^* e^{i\mu_\varphi t}\right) , \qquad (3.24)$$

which is so that the conditions for nonrelativistic behaviour are $|\dot{\chi}| \ll \mu_\varphi|\chi|$ and that timescales are much greater than $1/\mu_\varphi$. The latter means that any terms with phase factors that remain in Eq. (3.22) after substituting in Eq. (3.24) can be dropped, because these are rapidly oscillating and so, upon integrating the Lagrangian over time, have negligible net contribution to the action (although they do contribute to the emission of scalar radiation [95]).

The potential $V(\psi)$, expressed as a series in powers of ψ, is then easily dealt with. ψ^n for odd n has no terms without a rapidly-oscillating phase factor, while for even n the slowly-oscillating term in the expansion of ψ^n is $\binom{n}{n/2}(\chi^*\chi/2\mu_\varphi)^{n/2}$. In particular, the mass term $\mu_\varphi^2\psi^2/2$ becomes $\mu_\varphi\chi^*\chi/2$, while the following ψ^4 (the highest power that we will consider here) becomes $6(\chi^*\chi)^2/4\mu_\varphi^2$.

For the $\dot{\psi}^2$ term in Eq. (3.22), both χ and $e^{-i\mu_\varphi t}$ have nonzero time derivatives, so

$$\dot{\psi}^2 = \frac{1}{2\mu_\varphi} \left(\dot{\chi}e^{-i\mu_\varphi t} - i\mu_\varphi \chi e^{-i\mu_\varphi t} + \dot{\chi}^* e^{i\mu_\varphi t} + i\mu_\varphi \chi^* e^{i\mu_\varphi t} \right)^2$$

$$= \frac{1}{2\mu_\varphi} \left[(\dot{\chi}^2 - \mu_\varphi^2 \chi^2 - 2i\mu_\varphi \dot{\chi}\chi)e^{-2i\mu_\varphi t} + (\dot{\chi}^{*2} - \mu_\varphi^2 \chi^{*2} + 2i\mu_\varphi \dot{\chi}^* \chi^*)e^{2i\mu_\varphi t} \right]$$

$$+ \frac{1}{\mu_\varphi}\dot{\chi}^*\dot{\chi} + \mu_\varphi \chi^* \chi + i(\chi^*\dot{\chi} - \dot{\chi}^*\chi)$$

$$\approx \mu_\varphi \chi^* \chi + 2i\chi^*\dot{\chi} \ .$$

$$(3.25)$$

Along with taking $|\dot{\chi}|^2 \ll \mu_\varphi^2 |\chi|^2$ and neglecting terms with phase factors, the final line of Eq. (3.25) uses $-\dot{\chi}^*\chi = \chi^*\dot{\chi} - \partial_t(\chi^*\chi)$, with the time derivative in the latter also being dropped. Then,

$$\frac{1}{2}\dot{\psi}^2 - \Phi\dot{\psi}^2 \approx \frac{\mu_\varphi}{2}\chi^*\chi + i\chi^*\dot{\chi} - \mu_\varphi\Phi\chi^*\chi - 2i\Phi\chi^*\dot{\chi} \ . \qquad (3.26)$$

Although the first term on the right-hand side is much larger than the rest, when added to the remaining terms of Eq. (3.22) it will be cancelled out by the $-\mu_\varphi\chi^*\chi/2$ from the mass term of the potential. However, the fourth term is still small compared to the second term and can therefore be ignored. Thus, one Φ-dependent term remains even though $\Phi \ll 1$ because of the separation of time-dependent parts in Eq. (3.24) and the condition $|\dot{\chi}| \ll \mu_\varphi|\chi|$. As there is no analogous separation of the space-dependent parts of ψ, any perturbation of g^{ij} will remain negligible and need not be considered. The term for the spatial derivatives in Eq. (3.22) is then simply

$$-\frac{1}{2}g^{ij}\partial_i\psi\partial_j\psi \approx -\frac{1}{2}(\partial_i\psi)^2 = -\frac{1}{4\mu_\varphi}\left(\partial_i\chi e^{-i\mu_\varphi t} + \partial_i\chi^* e^{i\mu_\varphi t}\right)^2$$

$$= -\frac{1}{4\mu_\varphi}\left[(\partial_i\chi)^2 e^{-2i\mu_\varphi t} + (\partial_i\chi^*)^2 e^{2i\mu_\varphi t}\right] - \frac{1}{2\mu_\varphi}(\partial_i\chi^*)(\partial^i\chi) \ .$$

$$(3.27)$$

We now have Eq. (3.26), the term without phase factors at the end of Eq. (3.27), and the expansion of the potential $V(\psi)$ into $\mu_\varphi\chi^*\chi/2$ plus higher-order terms. Putting these into Eq. (3.28), the nonrelativistic Lagrangian is

$$\mathcal{L} \approx i\chi^*\dot{\chi} - \frac{1}{2\mu_\varphi}|\partial_i\chi|^2 - \mu_\varphi\Phi\chi^*\chi - v(\chi) \ , \qquad (3.28)$$

47

where $v(\chi)$ comprises the terms in the potential beyond $\mathcal{O}(\psi^2)$.

Having obtained the Lagrangian of Eq. (3.28), the nonrelativistic energy is then the volume integral of $\frac{\partial \mathcal{L}}{\partial \dot{\chi}} \dot{\chi} - \mathcal{L}$,

$$E = \int \left(\frac{1}{2\mu_\varphi} |\partial_i \chi|^2 + \mu_\varphi \Phi \chi^* \chi + v(\chi) \right) dV . \qquad (3.29)$$

The χ-dependent terms can be integrated by taking the field profile to describe a cloud of $N = \int \chi^* \chi \, dV$ particles[17]. For the gradient terms, consider that in the linearised limit, $v(\chi) \to 0$, we would derive a field equation that looks like the Schrödinger equation, so bound states around a spherical source mass (such as a black hole) will resemble the wavefunction of the hydrogen atom. Substituting back in the gravitational coupling by $\mu_\varphi \Phi = -\alpha/r$, and assuming for simplicity that all N particles, being created by superradiant amplification of an original fluctuation, remain in the same state and thus have the same l, this leads to an approximation for the energy

$$E = \frac{N}{2\mu_\varphi} \left(\frac{l(l+1)}{r^2} + \frac{1}{R^2} \right) - \frac{\alpha N}{r} + \int v(\chi) \, dV , \qquad (3.30)$$

where l is the angular momentum number (≥ 1 for any superradiantly amplified modes), r is the radial distance from the source mass, and R is the scale of the cloud extension.

The average orbital radius of the cloud, r_c, is given by

$$0 = \left. \frac{dE}{dr} \right|_{r=r_c} = -\frac{Nl(l+1)}{\mu_\varphi r_c^3} + \frac{\alpha N}{r_c^2} \Rightarrow r_c = \frac{l(l+1)}{\mu_\varphi \alpha}$$

$$\Rightarrow E = \frac{N}{2\mu_\varphi R^2} - \frac{\alpha N}{2r_c} + \int v(\chi) \, dV . \qquad (3.31)$$

From now on we shall consider only the leading-order term in $v(\chi)$, which we take to be $-\xi \psi^4$ for some constant ξ, and thereby obtain our final approximation for the cloud energy,

$$E = \frac{N}{2\mu_\varphi R^2} - \frac{\alpha N}{2r_c} - \frac{6\xi N^2}{4\mu_\varphi^2 R^3} . \qquad (3.32)$$

---

[17]This is slightly different to the N used in the Section 3.2, as it gives $\int \frac{1}{2} \mu_\varphi^2 \psi^* \psi \, dV = \frac{1}{2} N \mu_\varphi$ instead of $N \mu_\varphi$. Using this there would make ψ_0 smaller by a factor of $\sqrt{2}$, which makes next to no difference to the results, especially given that $V(\psi) = \mu_\varphi/(GM_{\rm H})^3$ is only a rough estimate to begin with.

3.3.1 Bosenovae and axion-like fields

The non-linearities that have so far received most attention are those with $\xi > 0$—a negative ψ^4 term—as it is for the axion-like potential of Eq. (3.7) which has $\bar{\varphi} = 0$ such that $\xi = \mu^2/24f^2$. For $\xi > 0$, one can find an energy-maximising cloud extension R_m from Eq. (3.32).

$$0 = \left.\frac{dE}{dR}\right|_{R=R_\mathrm{m}} = -\frac{N}{\mu_\varphi R_\mathrm{m}^3} + \frac{9\xi}{2\mu_\varphi^2}\frac{N^2}{R_\mathrm{m}^4} \Rightarrow R_\mathrm{m} = \frac{9\xi N}{2\mu_\varphi} \qquad (3.33)$$

Having $\xi > 0$ is key to ensure that the energy is maximised for a non-zero R. When $r_\mathrm{c} > R_\mathrm{m}$, the cloud is stable with $R \sim r_\mathrm{c}$, but when N increases (as it does during superradiance), it reaches a point where $R_\mathrm{m} > R$ and then the cloud can lose energy by decreasing in size, so the cloud collapses: this is a bosenova.

From Eq. (3.33), the number of particles N_m at which bosenova occurs is

$$R_\mathrm{m} = r_\mathrm{c} \Rightarrow N_\mathrm{m} = \frac{2l(l+1)}{9\xi\alpha} \ . \qquad (3.34)$$

It is worth comparing this to the condition required for $v(\chi) \to 0$, which if unsatisfied puts the Schrödinger-like approximation at risk, and which cannot necessarily be expected to hold when non-linearities are so strong as to change the qualitative behaviour of the cloud. The strongest bound comes from ensuring that the ψ^4 term in Eq. (3.32), $-6\xi N^2/4\mu_\varphi^2 R^3$, is much smaller than $N/2\mu_\varphi R^2$, which tells us that $\xi N \ll \mu_\varphi R$. However, when $R = R_\mathrm{m}$, Eq. (3.33) tells us that $\xi N = \frac{9}{2}\mu_\varphi R$. Therefore, satisfying the condition for bosenova takes us out of the regime where we can be sure that a hydrogen-like field profile is valid in the first place. This is not an argument against bosenovae being an outcome of non-perturbative effects on the evolution of axion fields, and indeed bosenovae have been simulated numerically both around black holes [87, 88] and in boson stars [99–101]. However, it shows that the analytic approximations described here are unreliable at quantifying the point at which an axion bosenova occurs.

3.3.2 Black hole superradiance of screened fifth forces

For $\xi < 0$, there is no non-negative R_m from Eq. (3.33) and therefore no collapse of the cloud will occur. What we can do instead is something that

was not done in previous studies, which is to consider an energy-extremising particle number N_e.

$$0 = \left.\frac{dE}{dN}\right|_{N=N_e} = \frac{1}{2\mu_\varphi R^2} - \frac{\alpha}{2r_c} - \frac{6\xi}{2\mu_\varphi^2}\frac{N_e}{R^3} \Rightarrow N_e = \frac{\mu_\varphi R}{6\xi}\left(1 - \frac{l(l+1)R^2}{r_c^2}\right)$$
(3.35)

As $d^2E/dN^2 \propto -\xi$, N_e is a maximum for $\xi > 0$, and when $R \sim r_c$ it is also not a positive number, which simply tells us that all bound states have less energy than zero-particle states as long as the cloud has not collapsed[18]. There is no finite energy-minimising particle number for $\xi > 0$, but rather the energy continues to decrease as $N \to \infty$, which tells us only that the cloud continues to grow[19] until it is inhibited by either of the conditions $\omega = m\Omega_H$ or $R_m > r_c$ being reached. Thus for axion-like particles Eq. (3.35) is not useful.

However, N_e is not only a minimum for $\xi < 0$, it is also non-negative for $R \sim r_c$. This suggests that, although superradiance for $\xi < 0$ potentials is not slowed down by bosenovae, it is still inhibited by non-linearities increasing the energy required to add more than N_e particles to the cloud. The condition that $|\xi|N \ll \mu_\varphi R$ is also somewhat more reasonable here than in the bosenova calculation: with $R = r_c$ and $l = 1$, Eq. (3.35) gives $|\xi|N_e = \frac{1}{6}\mu_\varphi R$.

Both the symmetron and the chameleon have $\xi < 0$, respectively

$$
\begin{aligned}
-\xi = \frac{\lambda}{4} &\Rightarrow v(\chi) \approx \frac{\lambda}{4}\frac{6(\chi^*\chi)^2}{4\mu_\varphi^2} = \frac{3\lambda}{8}\frac{(\chi^*\chi)^2}{\mu_\varphi^2} , \\
-\xi = \frac{\Lambda^5}{\bar{\varphi}^5} = \frac{\mu_\varphi^2}{2\bar{\varphi}^2} &\Rightarrow v(\chi) \approx \frac{\Lambda^5}{\bar{\varphi}^5}\frac{6(\chi^*\chi)^2}{4\mu_\varphi^2} = \frac{3}{4}\frac{(\chi^*\chi)^2}{\bar{\varphi}^2} .
\end{aligned}
$$
(3.36)

Putting these into Eq. (3.35), with $R = r_c$, gives

$$N_e = \frac{2L}{3\alpha}\frac{1}{\lambda} \quad \text{(symmetron)} , \qquad N_e = \frac{L}{3\alpha}\frac{\bar{\varphi}^2}{\mu_\varphi^2} \quad \text{(chameleon)} , \qquad (3.37)$$

where $L = l(l+1)[l(l+1) - 1]$. These N_e are $\bar{\varphi}^2/\mu_\varphi^2$ multiplied by an $\mathcal{O}(1)$ coefficient, at least for field configurations whose particles have low angular

---

[18]A statement which is equivalent to $N/2\mu_\varphi R^2 < \alpha N/2r_c$, which reduces to the trivial $l(l+1) > 0$ for $R = r_c$.

[19]The energy being minimised by actually infinite N neglects higher-order terms in the potential, and is equivalent to stating that $v(\chi) = -\xi\psi^4$ on its own is unstable for $\xi > 0$.

momenta, much like the expressions for $\bar{\varphi}^2/\psi_0^2$ obtained in Section 3.2. This seems to imply that the onset of non-linearity is, for thse models, around the point at which N is sufficiently large that superradiance is inhibited.

In conclusion, regardless of whether or not level mixing prevents non-perturbative effects such as bosenovae from affecting black hole superradiance, screened scalar fields appear to have their superradiant growth rapidly inhibited by their own self-interactions.

3.4 Conclusions

The aim of this section was to determine whether non-linearities in the symmetron and chameleon equations of motion have a non-negligible effect on the growth of superradiant clouds around Kerr black holes, and if so, whether this effect helps or hinders the prospects for probing these theories using observations of black holes that have lost, or are in the process of radiating away, their spin through the superradiant amplification of scalar fields.

To achieve the first goal, we estimated the amount of growth necessary for an initial scalar fluctuation ψ_0 to be amplified to a point where non-linearities become significant, given only that the theory obeys the bounds of Eq. (2.40) or Eq. (2.43) required for us to trust our classical models of screened scalar fields. Even taking ψ_0 to be as small as a single-particle fluctuation, we found that this point is reached long before the superradiant instability ends, and will also take a very short time on cosmological scales (no more than tens of thousands of years).

For the second goal, we adapted to screened fifth forces a method that has previously been used to study the black hole superradiance of axion-like particles. This method involves making a non-relativistic approximation to the action, from which one obtains an expression for the energy of a cloud of bosons gravitationally bound to a central mass. By varying this energy with respect to the spatial extent of the cloud or the number of particles within it, one can estimate how the cloud behaves as it grows. For axion-like particles this method suggested the existence of the bosenova, whereby a cloud with a large number of particles can radiate away energy by decreasing in size; when applied to the symmetron and chameleon, the method instead suggests that there exists an energy-minimising particle number which might instead inhibit the growth of clouds beyond this point, reducing the ability of searches for superradiance to probe such theories.

4 Extremely Compact Sources

In Sec. 1.4 we looked at the wide variety of experimental environments in which theories with screening have been studied [5,15,23,25,31–51]. In many of these situations, there is a large hierarchy between the (small) spatial extents of the source and probe objects and the (large) Compton wavelength of the scalar field, in particular laboratory experiments that use small test particles such as atoms [23,31,38–41], neutrons [42,43,51], or micro-spheres [44], where the scalar Compton wavelength may be of order the size of the vacuum chamber; and observations of astrophysical environments, where the screening objects are stars and planets, but the scalar Compton wavelength may be of order galactic scales [25].

We would like to be able to treat these sources as effectively point-like, but, to understand their screening properties, it is currently necessary to know the details of their structure. Herein, we will differentiate between *point-like* and *compact* sources. While the former refers only to the spatial extent of the source, we consider a compact source to be one that is both small, compared to the Compton wavelength of the field, and high density.

A comprehensive treatment of the screening of individual point-like objects also represents an important first step towards a robust understanding of how distributions of discrete objects interact with light scalar fields. Such an understanding would tell us whether and when such distributions may be "averaged over" and treated as a single extended source with some continuous density, which is how screening has so far been studied, and it is also important for knowing how and when to include the effects of screening when computing interparticle forces in N-body simulations, e.g., of structure formation in the universe [102–107], especially when it is too computationally expensive to calculate the scalar fields sourced by each particle from first principles. In this work, we consider the screening of fifth forces around compact, point-like objects in flat space, paving the way to further study in curved spacetimes, such as around black holes [108–111].

Because of non-linearities, it is not always obvious how the behaviours of the field and the associated fifth force extrapolate to new regimes. Exact analytic solutions can often be obtained for systems that vary only in one spatial dimension, having applications to experiments that take place between parallel plates, such as torsion-pendulum, Casimir, and neutron experiments [42, 46, 48, 112, 113], as well as the nested cylinders of the MICROSCOPE mission [114]. The solution for a point source in one spatial

52

dimension is also known analytically for particular choices of potential and coupling [14]. Beyond these examples, however, our knowledge is more limited. Therefore, in this work, we perform a detailed analysis of the impact of the dimensionality of the system on the problem of taking the point-like limit of an object in models with screening.

In this section, we aim to solve for the static configurations of the scalar field around spherical and cylindrical matter sources in the limit where the radius of the source tends to zero. The scalar fields we will consider are the symmetron model of Eq. (1.15) and the chameleon model of Eq. (1.25), the latter of which has a symmetron-like bare potential but a linear rather than quadratic coupling to matter. We will see that it is important to differentiate between the point-like limit where the spatial extent of a source is sent to zero, while holding its mass fixed, and the compact limit where the size of the source is shrunk and the mass of the source is increased.

Non-trivial static vacuum solutions of non-linear classical field theories are well known, and they are often referred to as (topological) defects. These solutions may be stable if they're supported by some non-trivial topology of the vacuum manifold in field space [115], and their stability properties can be characterised using Derrick's theorem [116]. The solutions that we consider in this work differ in that they are supported by matter distributions. We present a new extension of Derrick's theorem, which, for the first time, characterises the stability properties of field profiles supported by sources. Moreover, in three spatial dimensions, it allows us to infer the behaviour of the scalar field profiles in the point-like limit. While we might expect the point-like limit to be divergent, carefully studying the limiting procedure allows us to understand how these divergences are regulated[20] and to determine how the fifth forces due to compact, point-like sources are screened.

The key results of this section are:

- An extension of Derrick's theorem to scalar profiles supported by external sources.

- Piecewise analytic approximations for finding the field profiles around point-like sources.

- A numerical treatment of the scalar field profiles around point-like and compact sources.

---

[20]A similar approach is taken in theories of infinitesimally thin branes in higher-dimensional spacetimes [117, 118].

- A comparison of the screening factors between the full numerically calculated field profiles and the approximate solutions that are currently used in the literature to quantify the amount by which the fifth force is screened.

A summary of the behaviour of screening in this limit for the two prototypical theories that we study, and for spherically and cylindrically symmetric sources, can be found in Table 2.

Section 4.1 describes how Derrick's theorem is modified in the presence of classical sources and discusses its implications for the behaviour of the scalar field profiles as the source becomes increasingly compact. In Sec. 4.2, we turn our attention to the computation of the field profiles. Sections 4.2.1 to 4.2.3 focus on improved piecewise approximations to the potentials and field profiles. Section 4.2.4 subsequently describes the numerical procedure that we employ to solve for the field profile without making any approximations to the form of its potential, with Sec. 4.2.5 giving examples of the profiles that are thereby obtained. In Sec. 4.3, we describe the implications of our numerical results for screening and estimates of screening around extremely compact sources, quantified by scaling relationships (Sec. 4.3.1) and screening factors (Sec. 4.3.2). In Sec. 4.3.3, we comment on the reliability of our classical calculations, establish the regimes in which we trust the classical predictions and identify when quantum corrections may become large. Finally, we provide our conclusions in Sec. 4.4. Extra details relating to the numerical procedures and an explicit example of a construction of a piecewise field profile are included in the appendices. A summary of our notation is provided in Table 1.

This section is based on Ref. [119] written in collaboration with Clare Burrage, Benjamin Elder, Peter Millington, and Daniela Saadeh. Secs. 4.1 and 4.3.3 include derivations initially performed by Peter and Benjamin respectively; I have checked the calculations for myself and included them here due to their vital role in interpreting our results. The results of Secs. 4.2.4 and 4.2.5 are obtained using code based on φenics, which is described in Ref. [120] by Jonathan Braden, Clare Burrage, Benjamin Elder, and Daniela Saadeh, but the modifications to make a numerical solver that works for the symmetron and chameleon of Eqs. (1.15) and (1.25) are my work.

M	mass scale determining the strength of the matter coupling
μ	mass parameter in the potential of the screening scalar
λ	quartic self-coupling of the screening scalar
ρ	energy density of the matter source
λ_s	screening factor
$\bar{\phi}(\rho)$	position of the density-dependent minimum of the effective potential
$\bar{\phi}_\infty \equiv \bar{\phi}(0)$	position of the minimum of the effective potential for $\rho = 0$
r_s	source radius
m_s	source mass
$\rho_{\rm in}$	constant density of the source
$\rho_{\rm out}$	constant ambient density external to the source
$\bar{\phi}_{\rm in(out)} \equiv \bar{\phi}(\rho_{\rm in(out)})$	position of the minimum of the effective potential for $\rho = \rho_{\rm in(out)}$
$m_{\rm in(out)}$	effective mass of the scalar fluctuations inside(outside) the source
$x \equiv \mu r$	dimensionless radius
$x_s \equiv \mu r_s$	dimensionless source radius
$r_{\rm shell}$	thin-shell radius
d	number of spatial dimensions
$\tilde{\rho} \equiv \rho/\rho_c$	normalised density: $\rho_c = \mu^2 M^2$ for the quadratically coupled model and $\rho_c = \mu^3 M/\sqrt{\lambda}$ for the linearly coupled model
$\tilde{m}_s$	normalised source mass, $\tilde{m}_s = m_s \mu^{d-2} \bar{\phi}_\infty^{n-2}/M^n$: for the quadratically coupled model ($n = 2$), $\tilde{m}_s = m_s \mu^{d-2}/M^2$; for the linearly coupled model ($n = 1$), $\tilde{m}_s = m_s \sqrt{\lambda} \mu^{d-3}/M$
ν	effective mass of scalar fluctuations in units of μ
$\lambda_{\rm approx}$	screening factor as obtained from piecewise quadratic approximations to the effective potential
$\lambda_{\rm full}$	screening factor as obtained from the full numerical solutions

Table 1: Summary of key notation of Section 4 and their definitions (in order of appearance).

4.1 Derrick's theorem with classical sources

Derrick's theorem [116] provides a set of conditions for the existence of stable and stationary localised solutions to non-linear field equations. It is usually applied in vacuum, that is, in the absence of sources. In this section, we generalise the derivation of Derrick's theorem to incorporate the presence of a classical hyperspherically, i.e., $O(d)$ symmetric uniform source, with density described by a top-hat distribution. The usual stability arguments then translate into information about how the theories introduced in the previous section behave around point-like sources and allow us to test the accuracy of our numerical solutions in Sec. 4.2.4. For comparison, the standard derivation of Derrick's theorem is recovered straightforwardly when the density ρ of the classical source is taken to zero.

We are interested in stationary localised solutions, which must correspond to a minimum of the energy. For the quadratically and linearly coupled models that we study here, the energy is given in d spatial dimensions by

$$
E[\phi] \;=\; \int \mathrm{d}^d \mathbf{x} \left[\frac{1}{2} \left(\boldsymbol{\nabla}\phi(\mathbf{x}) \right)^2 \;+\; V(\phi(\mathbf{x})) + \frac{1}{n!} \frac{\rho(\mathbf{x})}{M^n} \phi^n \right] , \tag{4.1}
$$

where $n = 1, 2$. This energy is finite as long as we shift the potential so that the field has zero energy density in vacuum, see Eq. (1.15) with $V_0 = \mu^4/4\lambda$. We can write the contributions from the kinetic, potential and matter-coupling parts respectively as

$$
E_K[\phi] \;\equiv\; \frac{1}{2} \int \mathrm{d}^d \mathbf{x} \left(\boldsymbol{\nabla}\phi(\mathbf{x}) \right)^2 , \tag{4.2a}
$$

$$
E_V[\phi] \;\equiv\; \int \mathrm{d}^d \mathbf{x}\, V(\phi(\mathbf{x})) , \tag{4.2b}
$$

$$
E_\rho[\phi] \;\equiv\; \frac{1}{n!} \int \mathrm{d}^d \mathbf{x}\, \frac{\rho(\mathbf{x})}{M^n} \phi^n . \tag{4.2c}
$$

For a spherically symmetric, uniform source with $\rho(\mathbf{x}) \equiv \rho(r) = \rho_{\mathrm{in}}\theta(r_s - r)$, where ρ_{in} is a constant and θ is the unit step function, we can write

$$
E_\rho[\phi] \;=\; \frac{1}{n!} \int \mathrm{d}\Omega_d \int_0^{r_s} \mathrm{d}r\, r^{d-1} \frac{\rho_{\mathrm{in}}}{M^n} \phi^n(r) , \tag{4.3}
$$

where $\int \mathrm{d}\Omega_d$ is the integral over the solid angle

$$
\Omega_d = 2\pi^{d/2}/\Gamma(d/2) \tag{4.4}
$$

subtended by the d-dimensional sphere.

In order to determine whether any given solution ϕ is stable (with respect to growth or collapse), we are interested in the first and second variations of the energy with respect to the transformation $\phi(\mathbf{x}) \to \phi'(\mathbf{x}) = \phi(\omega\mathbf{x})$, requiring that $\mathrm{d}E[\phi']/\mathrm{d}\omega\big|_{\omega=1} = 0$ and $\mathrm{d}^2E[\phi']/\mathrm{d}\omega^2\big|_{\omega=1} \geq 0$. These conditions are respectively

$$\frac{1}{n!}\,\Omega_d\,r_s^d\,\frac{\rho_{\rm in}}{M^n}\,\phi^n(r_s) \;=\; (d-2)E_K[\phi] \;+\; d\big(E_V[\phi] + E_\rho[\phi]\big)\,, \qquad (4.5\mathrm{a})$$

$$\frac{1}{(n-1)!}\,\Omega_d\,r_s^{1+d}\,\frac{\rho_{\rm in}}{M^n}\,\phi^{n-1}(r_s)\partial_{r_s}\phi(r_s) \;\geq\; 2(d-2)E_K[\phi]\,. \qquad (4.5\mathrm{b})$$

Writing $m_s = \rho_{\rm in}\Omega_d r_s^d/d$ (the source mass), we have

$$\frac{d}{n!}\,\frac{m_s}{M^n}\,\phi^n(r_s) \;=\; (d-2)E_K[\phi] \;+\; d\big(E_V[\phi] + E_\rho[\phi]\big)\,, \qquad (4.6\mathrm{a})$$

$$\frac{d}{(n-1)!}\,r_s\,\frac{m_s}{M^n}\,\phi^{n-1}(r_s)\partial_{r_s}\phi(r_s) \;\geq\; 2(d-2)E_K[\phi]\,. \qquad (4.6\mathrm{b})$$

We now suppose that we want the field profile to be generated by a point source of finite mass, with $r_s \to 0$. As long as ϕ and its spatial derivatives remain finite, this removes the left-hand side of Eq. (4.6b), giving $(d-2)E_K[\phi] \leq 0$. Since $E_K[\phi] > 0$ for theories with a canonical kinetic term and spatially varying profiles, this is satisfied in $d = 1$ and 2, but not in $d > 2$. Therefore, for any model with a canonical kinetic term, the derivative of any stable and stationary field has to diverge at r_s in $d > 2$ as $r_s \to 0$.

Whether the field itself also diverges cannot be derived from the arguments above, but we might expect it to depend on the form of the potential and the matter coupling, such that the field will tend towards the minimum of its effective potential. This may or may not diverge as $\rho \to \infty$, depending on the choice of $V(\phi)$ and the value of n. With the choice of bare potential in Eq. (1.15), an even value of n brings the minimum of $V_{\rm eff}(\phi)$ to zero as $\rho \to \infty$, while an odd value causes it to diverge, as we will see later in Sec. 4.2.4 (see Fig. 10).

In the remainder of this work, we take d to be the effective dimensionality of the source. The case $d = 3$ corresponds to a spherically symmetric source in three spatial dimensions; the case $d = 2$ instead corresponds to a cylindrically symmetric source in three spatial dimensions, i.e., a cylinder with infinite extent along its symmetry axis. For the latter case, we assume

that the solution $\phi(r, z)$ in three spatial dimensions has a separable solution, $\phi(r, z) = \phi(r)Z(z)$ (with some abuse of notation), such that we can integrate out $Z(z)$ to obtain an effective two-dimensional action, absorbing the mass scales and separation constant into the model parameters, such that $\phi(r)$ is dimensionless (having therefore canonical dimensions within a two-dimensional action).

In this work, Eqs. (4.6a) and (4.6b) will be used to perform quantitative checks of the numerically obtained field profiles (see Sec. 4.2.4). However, as we have seen, they provide us with a qualitative prediction for the behaviour of those numerical solutions in the point-like limit in $d = 3$.

4.2 Computing field profiles around extremely compact sources

In this section, we will describe how to compute the static scalar field profiles around sources as they become more compact and point-like. We begin by describing how the piecewise analytic approach to solving the field profiles can be extended to more compact sources. We then proceed to describe our numerical approach to computing these profiles, and the properties of the solutions that we find. We will consider solutions around an infinite cylinder ($d = 2$) and around a sphere ($d = 3$). Both sources will have a radius r_s and uniform density ρ, such that $\rho_{\text{in}} = \rho$ inside the source ($r \leq r_s$) and $\rho_{\text{out}} = 0$ outside the source ($r > r_s$). We note that ρ is a mass density with units mass/length^3 for a sphere and units mass/length^2 for an infinite cylinder.

Since we consider extended sources of finite density, we demand that the field profile is regular at $r = 0$ and that it approaches one of the field values that minimise the effective potential as $r \to \infty$. In vacuum, the effective potential for both models is invariant under $\phi \to -\phi$, and the field is equally likely to sit in the minimum at positive or negative ϕ. If the field couples to matter quadratically, as in Eq. (1.15), then the symmetry under $\phi \to -\phi$ is preserved in the matter coupling, and, up to an overall sign, the form of the field profile is insensitive to the choice of vacuum at $r \to \infty$.

The linearly coupled model of Eq. (1.25) requires more careful consideration, as the symmetry is broken explicitly inside the source by the matter coupling. For certain combinations of boundary conditions and sources, we will be unable to find piecewise analytic solutions. For example, if the boundary condition is $\phi \to -\bar{\phi}_\infty$ as $r \to \infty$ then the field may enter a regime close

58

to the surface of the source where the ϕ^4 term of the full effective potential dominates. It will not be possible to find a piecewise analytic solution in this case.

In what follows, and for the linearly coupled model, we will consider configurations where the field is in the $\bar{\phi}_\infty$ vacuum at infinity but where the field becomes large and negative inside the source. This raises the question of whether such a configuration is truly stable or whether it can tunnel to nucleate a bubble of the $-\bar{\phi}_\infty$ vacuum around the source. We leave further investigation of this interesting possibility for future work.

4.2.1 Piecewise appproximations

In Secs. 1.3.1 and 1.3.2, we outlined the approach that is common in the literature to finding piecewise analytic solutions for the scalar field profiles around compact objects, by approximating the full equations of motion,

$$\nabla^2 \phi = V'_{\text{eff}}(\phi) \ , \tag{4.7}$$

with equations that use approximate potentials that are either quadratic in ϕ around the density-dependent minima of the full effective potentials $V_{\text{eff}}(\phi)$, or are linear functions of ϕ in a "thin shell" region where a linear matter coupling dominates over the other terms in $V_{\text{eff}}(\phi)$. For the quadratically coupled model, and for unscreened objects in the linearly coupled model, we divided space into two parts: one inside and one outside the source; for screened objects in the linearly coupled model, we further divided the space inside the source into two regions. We will refer to these as two- and three-part solutions, respectively. When we outlined these approximations to the field profiles and the corresponding screening factors, however, we failed to check whether the values of the field in each spatial region were consistent with the approximations made to the effective potential. We will see here that for more point-like sources, these approximations do fail, and the solutions in Secs. 1.3.1 and 1.3.2 are inconsistent. For a wide range of sources, however, we can continue to make successive linear and quadratic approximations to the scalar potential, before matching the solutions to these approximate equations together.

The effective potentials in Eqs. (1.15) and (1.25) depend on three fixed scales, which we take to be the Compton wavelength $1/\mu$ (in vacuo), the vacuum expectation value (vev) $\bar{\phi}_\infty = \mu/\sqrt{\lambda}$ and the matter coupling ρ/M^n ($n = 1, 2$, depending on whether the coupling to matter is linear or quadratic

in the scalar field). This gives us the freedom to make two rescalings of the equations of motion and express them only in terms of dimensionless quantities. The solutions will depend on the dimensionless distance $x = \mu r$ (so that the source radius is $x_s = \mu r_s$) and the dimensionless source density $\tilde{\rho} := \rho \bar{\phi}_\infty^{n-2}/\mu^2 M^n$. For the quadratic coupling, this dimensionless density is $\tilde{\rho} = \rho/\mu^2 M^2$; it is the ratio of the source density to the critical density. For the linear coupling, it is $\tilde{\rho} = \sqrt{\lambda}\rho/\mu^3 M$.

When taking the point-source limit $x_s \to 0$, we keep the source mass fixed. We therefore parametrise the source mass as $\tilde{m}_s := \Omega_d \tilde{\rho} x_s^d/d = m_s \mu^{d-2} \bar{\phi}_\infty^{n-2}/M^n$, where Ω_d is the d-dimensional solid angle defined in Eq. (4.4). For the quadratic coupling, this dimensionless mass is $\tilde{m}_s = m_s \mu^{d-2}/M^2$; for the linear coupling, it is $\tilde{m}_s = m_s \sqrt{\lambda}\mu^{d-3}/M$. Solutions and screening factors then depend only on $\tilde{m}_s$ and x_s, except for an overall factor of $\bar{\phi}_\infty^2/M^2$ for the screening factors in the quadratically coupled models (Sec. 1.3.1).

4.2.2 The effective potential

We now briefly outline when linear and quadratic approximations can be made to the effective potential for our models. We begin by considering the effective potential outside the source, which is the same for both the quadratically and linearly coupled models.

1. Around $\phi \approx 0$, to quadratic order the potential $-\frac{1}{2}\mu^2\phi^2 + \frac{1}{4}\lambda\phi^4$ is simply $-\frac{1}{2}\mu^2\phi^2$.
2. The expansion of the potential to quadratic order around the minima $\pm\bar{\phi}_\infty$ is $V(\bar{\phi}_\infty) + \frac{1}{2}V''(\phi)\big|_{\phi=\bar{\phi}_\infty}(|\phi| - \bar{\phi}_\infty)^2$. Since $V(\bar{\phi}_\infty) = -\mu^4/4\lambda = -\frac{1}{4}\mu^2\bar{\phi}_\infty^2$ and $V''(\phi)\big|_{\phi=\bar{\phi}_\infty} = 2\mu^2$, this gives us $\frac{3}{4}\mu^2\bar{\phi}_\infty^2 + \mu^2\phi^2 - 2\mu^2\bar{\phi}_\infty|\phi|$.
3. Joining these together is a linear piece $a - b|\phi|$, where a and b, and the values of ϕ where the three pieces are stitched together, are the constants of integration that must be determined by enforcing continuity of the approxiated potential and its first derivative.

When this is done we find that the effective potential is well approximated by

$$V_{\text{out}}(\phi) \equiv \mu^2 \begin{cases} -\frac{1}{2}\phi^2, & 0 \leq |\phi| \leq \frac{1}{3}\bar{\phi}_\infty \\ \frac{1}{18}\bar{\phi}_\infty^2 - \frac{1}{3}\bar{\phi}_\infty|\phi|, & \frac{1}{3}\bar{\phi}_\infty \leq |\phi| \leq \frac{5}{6}\bar{\phi}_\infty \\ \frac{3}{4}\bar{\phi}_\infty^2 + \phi^2 - 2\bar{\phi}_\infty|\phi|, & \frac{5}{6}\bar{\phi}_\infty \leq |\phi| \leq \bar{\phi}_\infty \end{cases} . \quad (4.8)$$

As a result, we can consider up to three spatial regions outside the source. A comparison between this approximation and the full form of $V(\phi)$ is shown
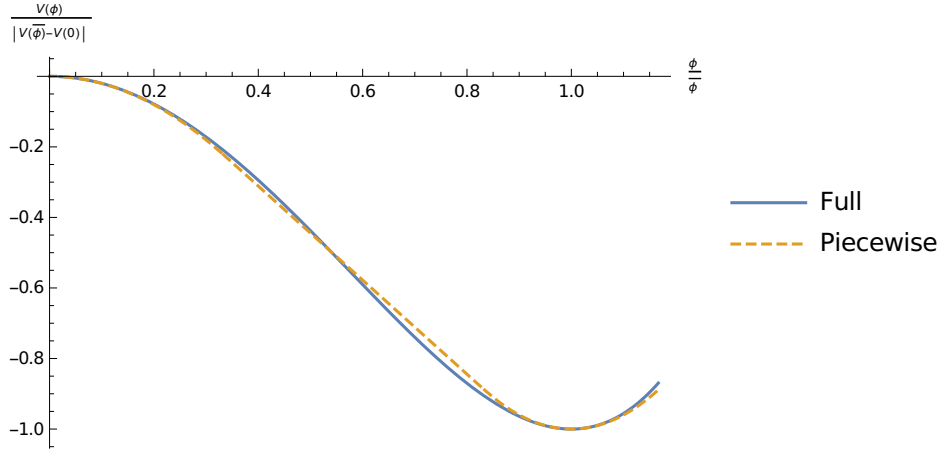
Figure 8: The symmetron potential $V(\phi) = \lambda\phi^4/4 - \mu^2\phi^2/2$ for $\phi > 0$ (blue, solid) and the corresponding piecewise approximation (orange, dashed).

in Fig. 8.

Inside the source, $\rho > 0$, and we must differentiate between the behaviour of the linearly and quadratically coupled models:

1. **Quadratic coupling.** We approximate the effective potential as

$$V_{\rm in}(\phi) \equiv V(0) + \frac{1}{2}\nu^2\mu^2(\phi - \bar{\phi}(\rho))^2 \ . \tag{4.9}$$

   This expansion is valid when ν, the mass of the scalar fluctuations in units of μ, satisfies $\nu^2 \gg 2\bar{\phi}(\rho)(\phi - \bar{\phi}(\rho))/\bar{\phi}_\infty^2$. This is always true for sources with $\rho > \mu^2 M^2$, since $\bar{\phi}(\rho) = 0$ and $\nu^2 = \rho/(\mu^2 M^2) - 1 > 0$ for this case. For sources with $\rho < \mu^2 M^2$, $\bar{\phi}(\rho) = \bar{\phi}_\infty\sqrt{1 - \rho/(\mu^2 M^2)}$ and $\nu^2 = 2[1 - \rho/(\mu^2 M^2)]$. The condition $\nu^2 \gg 2\bar{\phi}(\rho)(\phi - \bar{\phi}(\rho))/\bar{\phi}_\infty^2$ then simplifies to $\phi - \bar{\phi}(\rho) \ll \bar{\phi}(\rho)$, and it is possible to make a consistent quadratic approximation around this minimum everywhere inside the source as long as ϕ remains less than $2\bar{\phi}(\rho) = 2\bar{\phi}_\infty\sqrt{1 - \rho/(\mu^2 M^2)}$. Otherwise, the field profile must be found numerically, as we do below.

2. **Linear coupling.** For the linearly coupled model, there are two cases to consider: $\tilde{\rho} < \sqrt{12}/9$, when the effective potential inside the source has two non-degenerate minima; and $\tilde{\rho} > \sqrt{12}/9$, when the effective potential has only one minimum.

   When the effective potential has two minima, the first minimum ϕ_+ satisfies $\bar{\phi}_\infty/\sqrt{3} < \phi_+ < \bar{\phi}_\infty$ (moving from the upper to the lower limit

61

of this range as the density increases). The second minimum ϕ_- lies in the range $\phi_- < -\bar{\phi}_\infty$ (decreasing monotonically as $\tilde{\rho}$ increases). The only situation that we can approximate analytically is when ϕ remains close to ϕ_+ inside the source, in which case we can approximate the effective potential as a quadratic around ϕ_+, i.e.,

$$V_{\text{out}}(\phi) \equiv V(\phi_+) + \frac{1}{2}\nu^2\mu^2(\phi - \phi_+)^2 \ . \tag{4.10}$$

When only one minimum is present, the field may pass through a region where $|\phi| \ll \tilde{\rho}^{1/3}\bar{\phi}_\infty$ before it is able to reach the minimum of the potential. This region defines a "shell" near the surface of the source. In this case, we find

$$V(\phi) = \mu^2 \begin{cases} \dfrac{1}{4\bar{\phi}_\infty^2}\bar{\phi}(\rho)^4 - \dfrac{1}{2}\bar{\phi}(\rho)^2 + \tilde{\rho}\bar{\phi}_\infty\bar{\phi}(\rho) \\ \qquad\qquad + \dfrac{1}{2}\nu^2(\phi - \bar{\phi}(\rho))^2 \ , & \phi \le \zeta\bar{\phi}_\infty \\ \tilde{\rho}\bar{\phi}_\infty\phi - \frac{1}{2}\phi^2 \ , & \zeta\bar{\phi}_\infty \le \phi \end{cases} \ , \tag{4.11}$$

where

$$\nu^2 = \frac{\tilde{\rho}^2 - 2U}{2U - 2\tilde{\rho}\bar{\varphi}(\rho) + \bar{\varphi}^2(\rho)} \ , \tag{4.12a}$$

$$\zeta = \frac{2U - \tilde{\rho}\bar{\varphi}(\rho)}{\tilde{\rho} - \bar{\varphi}(\rho)} \ , \tag{4.12b}$$

$$U = \frac{\lambda}{\mu^4}V_{\text{eff}}(\bar{\phi}(\rho)) \ , \tag{4.12c}$$

and $\bar{\varphi}(\rho) := \bar{\phi}(\rho)/\bar{\phi}_\infty$. Although not obvious from the expression, $\zeta < 0$ by construction, since $\bar{\phi}(\rho) < \zeta\bar{\phi}_\infty < 0$. As $\tilde{\rho} \to \infty$, $\zeta \to -\tilde{\rho}^{1/3}/2 = \bar{\varphi}(\rho)/2$.

The construction of Eq. (4.11) is similar to the much simpler construction of the linearly coupled solutions in Sec. 1.3.2, where instead only the $\tilde{\rho}$ term is kept in the shell and the interior region has a constant $\phi(r) = \bar{\phi}(\rho)$. By Eq. (1.28), the equivalent of ζ is then $1 - \rho r_s^2/(2M\bar{\phi}_\infty)$. Note that, in the case of quadratic coupling, we only have one approximation to the potential and one region inside the source; for the linearly coupled model, we have at most two. This is the same as in the calculation of the screening factors outlined in Secs. 1.3.1 and 1.3.2 respectively. However, in what follows, we will be careful to check the validity of these approximations.

4.2.3 Piecewise scalar field profiles

Figure 9 provides examples of piecewise continuous field profiles around spherically symmetric sources (in three spatial dimensions) and cylindrically symmetric sources (in two spatial dimensions) for both the quadratically (Fig. 9a) and linearly coupled models (Fig. 9b). The constants of integration in the piecewise solutions to the scalar equations of motion are determined by ensuring continuity of the field and its first derivative at the matching surfaces. An example of this construction is given in Appendix A. For cylindrically symmetric sources, analytic solutions to the equations determining the constants of integration are not available, and they must instead be solved numerically. The source parameters for the various examples shown in Fig. 9 were chosen to give sources of sufficient compactness to require a two-part (solid blue), three-part (solid orange) or four-part (solid green) piecewise construction. The dotted lines are the "standard" two- (for quadratic coupling) and three-part (for linear coupling) approximations to the field profiles around a source of the same mass and radius, as outlined in Secs. 1.3.1 and 1.3.2, and references therein. For the linearly coupled case, the sources have $\tilde{\rho} > \sqrt{12}/9$ so that the effective potential inside the source only has a single minimum. By inspection, we see that the approximations for the linear coupling fail to capture the full behaviour of the field profiles, and this worsens as the sources become more compact.

One can see from these profiles that the qualitative behaviour is the same around spherically and cylindrically symmetric sources: for the quadratic coupling, the field at the centre of the source tends towards zero as the source density increases; for the linear coupling, the field at the centre of the source becomes more negative as the source becomes more compact. We begin to see indications of the behaviour of the field profiles around extremely compact sources. For the quadratic coupling, the field value at the origin decreases towards zero as the source becomes more compact. In three spatial dimensions, as the source is made more compact, the field profile becomes flatter in the exterior of the source, and the field rises more steeply in the vicinity of the surface of the source. This matches our conclusions in Sec. 4.1 that the gradient of the field should diverge at the origin, while the field itself

63
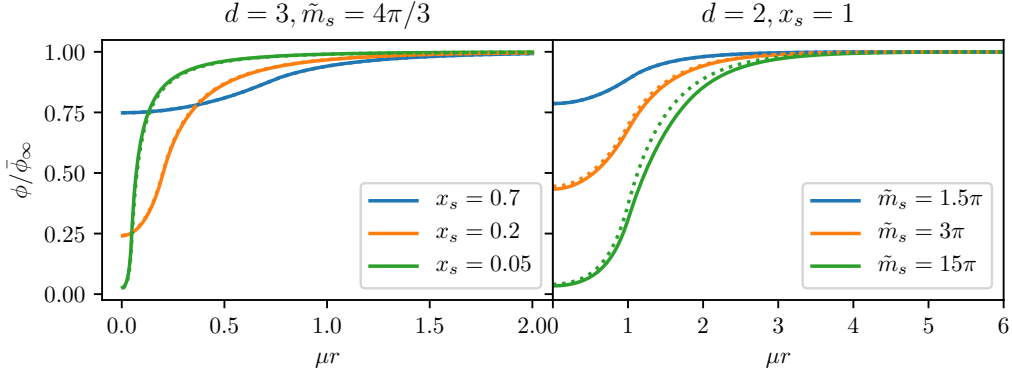
(a) quadratically coupled model
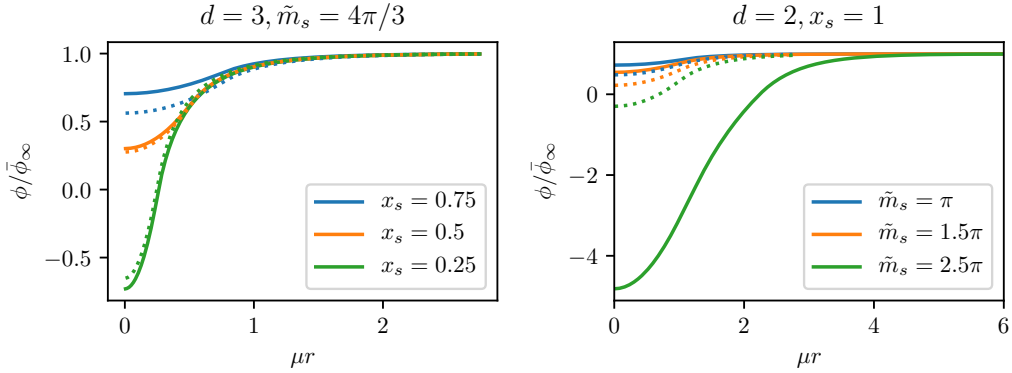
(b) linearly coupled model

Figure 9: Examples of piecewise-constructed field profiles around spherical sources, i.e., $d = 3$ (left panels), and cylindrical sources, i.e., $d = 2$ (right panels), for (a) the quadratically coupled model and (b) the linearly coupled model. In each case, the values of the dimensionless source radius x_s and the dimensionless source mass $\tilde{m}_s$ are chosen so that we require a two-part (solid blue), three-part (solid orange) or four-part (solid green) solution. The quartic self-coupling was taken to be unity, i.e., $\lambda = 1$. The dotted lines give the corresponding approximate solutions constructed as described in Secs. 1.3.1 and 1.3.2. In the quadratically coupled case, the solid blue and dotted blue lines are indistinguishable. We remark that there is generally good agreement with our multi-part solutions in the quadratically coupled case. On the other hand, we see that the standard approximate solutions deviate significantly from our multi-part solutions in the linearly coupled case and especially for cylindrically symmetric sources, i.e., in $d = 2$.

64

should go to $\bar{\phi}(\rho) = 0$. This will be confirmed by our numerical solutions in Sec. 4.3.1. Also in agreement with our conclusions in Sec. 4.1, we see in the linearly coupled model that the field evolves through $\phi = 0$ and becomes negative for compact sources, and our calculations indicate the possibility that the value of the field at the origin diverges in the point-source limit. We will explore this further with our numerical field profiles in Sec. 4.3.1.

4.2.4 Numerical calculations of field profiles

The piecewise approximations to the field profiles, derived in the previous section, give us some intuition for how the quadratically and linearly coupled models behave around increasingly point-like sources. In this section, we compute numerical solutions to the full equations of motion for both the linearly and quadratically coupled models around cylindrical and spherical sources.

To obtain the numerical solutions, we have modified the φ`enics` code[21], a numerical code building on the `FEniCS` library[22] [121–123] and applying the finite element method to problems of screening. The modified numerical code, as well as `Jupyter` notebooks for the main results presented in this section, are available at `https://github.com/benjthrussell/symsolver`. The numerical method underlying the φ`enics` code has been extensively described in Ref. [120]. In the following, we limit ourselves to summarising its main qualitative aspects, while focusing on the details of the implementation specific to this work. We conclude by showing sample field profiles around highly compact sources.

The equations of motion to be solved are

$$\nabla^2 \phi + \mu^2 \phi - \lambda \phi^3 - \frac{\rho}{M^2} \phi = 0 \qquad (4.13)$$

for the quadratically coupled model of Eq. (1.15), and

$$\nabla^2 \phi + \mu^2 \phi - \lambda \phi^3 - \frac{\rho}{M} = 0 \qquad (4.14)$$

for the linearly coupled model of Eq. (1.25), for field profiles with the boundary conditions $\{\mathrm{d}\phi(r \to 0)/\mathrm{d}r = 0; \; \phi(r \to \infty) = \mu/\sqrt{\lambda}\}$. For computational convenience, we work with dimensionless quantities: further details can be

---

[21]`https://github.com/scaramouche-00/phienics`
[22]`https://fenicsproject.org/`

found in Appendix A of Ref. [120]. However, in this section, we will express all equations in their native form for readability.

The equations of motion can trivially be rewritten in terms of $\psi = \phi - \bar{\phi}_\infty$, for which the Dirichlet boundary condition $\phi(r \to \infty) = \mu/\sqrt{\lambda}$ becomes $\psi(r \to \infty) = 0$. We have developed both solvers, i.e., one for the field ϕ and another one for the field ψ. We find the latter to be more accurate, thanks to its better characterisation of the exponential decay at large r.

Eqs. (4.13) and (4.14) are:

- non-linear boundary value problems

- which may have a large hierarchy in scales (between the source radius and the field's Compton wavelength)

- in which we need to calculate the field's behaviour around a sharp transition between $\rho = 0$ and $\rho \neq 0$ regions (in order to test our results against the Derrick's theorem conditions of Eq. (4.6), which were derived under the assumption of a step profile),

all of which combine to make for a very challenging numerical problem, but nevertheless a problem which the finite element method is suited for. The finite element method has been applied successfully to the study of chameleon [33,41,124] and symmetron screening [40,47,50], as well as Vainshtein screening [120, 125, 126] (which involves non-canonical kinetic terms rather than non-linear potentials). A detailed presentation of the method is beyond the scope of this work; we refer the interested reader to Refs. [123, 127], while listing here the most relevant basic aspects. A discussion focused on using the finite element method for solving equations of motion with screening, including worked examples, is given in Ref. [120].

The finite element method involves solving a discrete approximation to the original continuous problem. The domain of the function is discretised into a mesh, and the function space itself is discretised into a space of polynomials. I will now explain each of these in turn.

Firstly, we run our numerical calculations over only a finite region of space, and since the solutions we are studying are spherically or cylindrically symmetric, this means we take a radial domain $r/r_s \in [0, \hat{r}_{\max}]$ for some appropriately large dimensionless number $\hat{r}_{\max}$[23]. This domain is then divided

---

[23]We take $\hat{r}_{\max} = 10^4/x_s$ (so that $\hat{r}_{\max} r_s = 10^4/\mu$, i.e., 10^4 times the field's Compton wavelength) when $x_s < 1$, and $\hat{r}_{\max} = 100$ when $x_s \geq 1$.

into N intervals $\{[\hat{r}_i, \hat{r}_{i+1}], i \in 0, \cdots, N\}$, with $\hat{r}_0 = 0$ and $\hat{r}_{N+1} = \hat{r}_{\max}$, which we will refer to as "cells". We will additionally refer to the collection of all cells as a "mesh" and to cell extrema as mesh "vertices". Details of the meshes that we use are given in Ref. [120].

$\hat{r}_{i+1} - \hat{r}_i$ does not need to be the same for all i. This allows us to overcome the difficulties caused by having a large hierarchy of scales and a sharp transition at the source radius, as we can calculate the field profile to a high resolution close to the source by having small cells, while having large cells far from the source, where the field is expected to evolve more slowly, means that computational costs are not magnified across the entire domain.

Secondly, the space of solutions is discretised. A set of basis functions[24] is chosen—in this work, they will be Lagrange polynomials—on every mesh cell[25], and each piece of the solution on each cell is a linear combination of these basis functions, equated at the vertices to obtain a piecewise continuous function across the entire mesh. Finding a numerical solution to a given equation of motion then amounts to finding the coefficients of each term in these sums of basis functions, which is a problem amenable to linear algebra if the equation of motion is expressed in an appropriate form.

Our solver solves these linear algebra problems using Newton's method, which finds a sequence of iterated approximations $\{\phi^{(k)}\}$ for integers k, with the aim of starting from an initial guess $\phi^{(0)}$ and reaching a close approximation $\phi^{(n_{\text{iter}})}$, where n_{iter} is the total number of iterations, to the true solution ϕ.

When $\phi^{(k)}$ is sufficiently close to ϕ, Eqs. (4.13) and (4.14) can be expanded to first order to obtain linearised equations of motion for an improved approximation $\phi^{(k+1)}$ using the current iteration $\phi^{(k)}$,

$$\nabla^2 \phi^{(k+1)} + \mu^2 \phi^{(k+1)} - 3\lambda(\phi^{(k)})^2 \phi^{(k+1)} + 2\lambda(\phi^{(k)})^3 - \frac{\rho}{M^2}\phi^{(k+1)} = 0 \; ,$$
(4.15a)

$$\nabla^2 \phi^{(k+1)} + \mu^2 \phi^{(k+1)} - 3\lambda(\phi^{(k)})^2 \phi^{(k+1)} + 2\lambda(\phi^{(k)})^3 - \frac{\rho}{M} = 0 \; . \quad (4.15b)$$

Although the solutions to these will not solve the full non-linear equations of motion, the residuals will decrease as more iterations are performed until

---

[24]For the number of basis functions used in the results we present, as well as for any other numerical setting, we refer the reader to the code and the `Jupyter` notebooks on `https://github.com/benjthrussell/symsolver`.

[25]It is not always desirable to employ globally continuous function spaces; see, e.g., Ref. [120].

a desired accuracy has been obtained. The convergence criteria that we use are discussed in Ref. [120].

In particular, the finite element method works well with the "weak" formulation of the equation of motion, in which rather than demanding that the left-hand side of the chosen equation of motion in Eq. (4.15) vanishes at every point throughout the entire domain $r/r_s \in [0, \hat{r}_{\max}]$, we demand only the vanishing of the inner product of the left-hand side with some chosen "test" functions v. The inner product in this case is a volume integral of the product of the two functions, and so the weak form of the equations of motion Eq. (4.15) are

$$
-\int \nabla \phi^{(k+1)} \, \nabla v \, r^{d-1} \, \mathrm{d}r + \int \left(\mu^2 - 3\lambda (\phi^{(k)})^2 - \frac{\rho}{M^2} \right) \phi^{(k+1)} \, v \, r^{d-1} \, \mathrm{d}r
$$
$$
= -2\lambda \int (\phi^{(k)})^3 \, v \, r^{d-1} \, \mathrm{d}r \ ,
$$
(4.16a)

$$
-\int \nabla \phi^{(k+1)} \, \nabla v \, r^{d-1} \, \mathrm{d}r + \int \left(\mu^2 - 3\lambda (\phi^{(k)})^2 \right) \phi^{(k+1)} \, v \, r^{d-1} \, \mathrm{d}r
$$
$$
= \int \left(\frac{\rho}{M} - 2\lambda (\phi^{(k)})^3 \right) \, v \, r^{d-1} \, \mathrm{d}r \ ,
$$
(4.16b)

where we have used the Neumann boundary condition $\mathrm{d}\phi(r \to 0)/\mathrm{d}r = 0$ and integrated by parts the term $\int \nabla^2 \phi^{(k+1)} \, v \, r^{d-1} \, \mathrm{d}r$ to lower the order of the first differential operator. For the test space, we use the space of square-integrable functions on $\mathbb{R}^d$, whose gradients are also square-integrable on $\mathbb{R}^d$. This integral form is particularly adept at handling sharp transitions like the step source profile for which we intend to solve.

Initial guess

In Sec. 4.2.1, we showed how to approximate the scalar field profile around a compact source, which could serve as an initial guess for our iterative Newton's solver. We use the conditions on the matching radii, derived for the piecewise approximations of Sec. 4.2.1 to determine how many piecewise approximations we need to match together to find a good initial guess for a given set of model and source parameters. Whilst it would be possible to also use the analytic expressions previously determined as piecewise approximations in these regions, we find it numerically more efficient to use `FEniCS`

to solve the linearised equations of motion in each region in order to find a good initial guess. The resulting initial guesses are an excellent match to our analytically derived piecewise profiles. The coefficients of the linearised equations of motion solved by `FEniCS` to find the required initial guess are given in Appendix B.

For the quadratically coupled model, when $\tilde{\rho} = 1$, the approximation described in Sec. 4.2.1 fails. In this case, we artificially detune the physical parameters away from the critical point $\rho = (\mu M)^2$ for the purpose of obtaining an initial guess for the algorithm. Further details are given in Appendix B. We stress that the initial guess only needs to be accurate enough to allow the solver to converge to the correct physical solution; it need not be an accurate reflection of the final profile, although a more accurate initial guess will ensure faster convergence to the true solution.

4.2.5 Numerical scalar field profiles

To ensure the validity of our numerical solutions, we perform all the convergence tests described in Appendix B of Ref. [120]. Moreover, we perform the Derrick's theorem tests of Eqs. (4.6a) and (4.6b). We have checked that our results do not depend on the specific source profile used for the density: a step function, a smoothed top-hat profile, or a Gaussian profile. We present results for the step function here, since these can be compared with the analytic results in Eqs. (4.5a) and (4.5b), derived from the generalisation of Derrick's theorem.

For choices of parameters where we trust the validity of our piecewise initial guesses, such as those shown in Fig. 9 and the orange lines in Fig. 10, we find that the field profile found by our solver is always close to that initial guess. For the quadratically coupled model around spherically symmetric sources (or in three spatial dimensions), we find the limiting behaviour that $\phi(r_s) \to 0$ for more compact sources, as we might expect. For cylindrically symmetric sources (or in two spatial dimensions), we find the same limiting behaviour, but shallower gradients, with the field reaching zero more slowly, cf. Table 2. For the linearly coupled model around spherically symmetric (three-dimensional) sources, we find that $\phi(r = 0) \approx \bar{\phi}(\rho) = -\bar{\phi}_\infty \tilde{\rho}^{1/3}$ for small r_s. For cylindrically symmetric ($d = 2$) sources, we find that that $\phi(r = 0)$ becomes very negative, although the particular scaling with the source parameters is more complicated, as we describe in Sec. 4.3.1. This confirms our hypothesis that the field at the origin diverges near a point

69
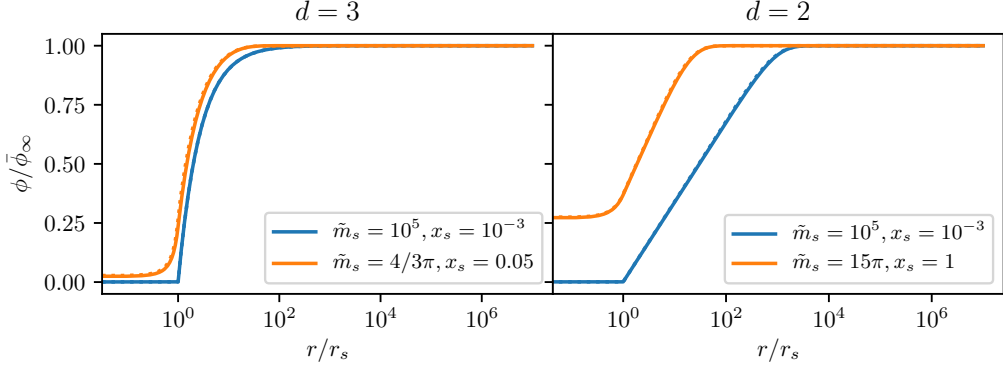
(a) quadratically coupled model
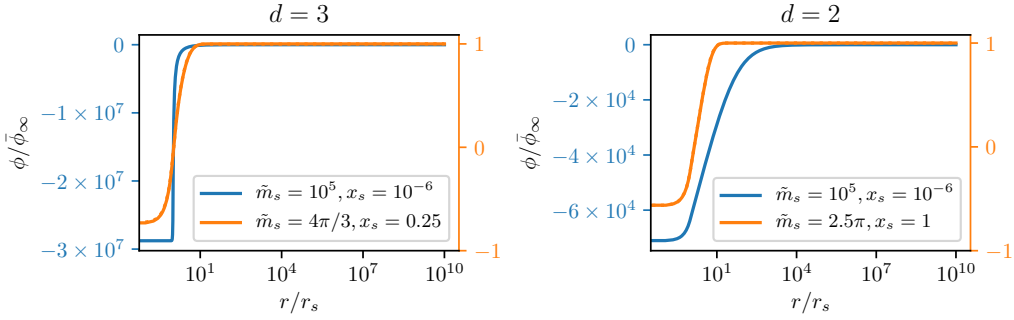
(b) linearly coupled model

Figure 10: Comparison of the numerically obtained (solid lines) and four-part piecewise constructed field profiles (dotted lines) for (a) the quadratically coupled model and (b) the linearly coupled model for spherically ($d = 3$) and cylindrically ($d = 2$) symmetric sources. For the compact source in the linearly coupled case (blue), only the numerical solution is plotted, since the piecewise approximate solution overshoots the minimum to large negative values. In this case, the field value $|\phi(r_\mathrm{s})|$ is far greater than the vev $\bar{\phi}_\infty$ and is therefore outside the range of validity for the linearised potential in Eq. (4.8). Nevertheless, the numerical results agree with our expectations, such that the field reaches a minimum value with $\phi/\bar{\phi}_\infty = -\tilde{\rho}^{1/3}$ at the centre of the source. This relationship holds for other parameter choices, allowing us to confirm that inside dense sources, the field generally reaches the minimum of the effective potential at the origin. Elsewhere, we see that there is excellent agreement between the full numerical profiles and the four-part piecewise constructed profiles.

source in the linearly coupled model. Examples supporting all the above inferences are shown in Fig. 10.

4.3 Implications for screening around extremely compact sources

In this section, we describe the key implications of our results for the screening of dense objects whose spatial extent is significantly smaller than the Compton wavelength of the fifth-force mediator. We summarise these implications in two ways. First, we provide a set of scaling relationships, which capture the behaviour of the scalar field and its boundary conditions at the surface of the source. These allow our results to be extrapolated to even more compact sources. Second, we compare the screening factors obtained from our full numerical solutions with those obtained from the piecewise approximations usually applied in the literature. Where these screening factors disagree, our full numerical results provide refined screening conditions, which will find utility in phenomenological studies. Finally, and before offering our conclusions, we draw attention to the potential relevance of quantum corrections.

4.3.1 Scaling relationships

The piecewise approximations to the field profiles derived in Sec. 4.2, along with the inferences from applying our generalisation of Derrick's theorem, indicated the possible behaviour of the field profiles as the compactness of the sources increases. By complementing these results with full numerical solutions, we are able to analyse behaviour in regimes beyond the applicability of the piecewise approximations. By these means, we can extract a set of scaling relationships that characterise how the field value $\phi(r_s)$ and the field gradient $\mathrm{d}\phi(r_s)/\mathrm{d}r$ at the surface of the source vary with source mass and radius. This allows us to see the scaling in both the point-like limit, where $x_s \to 0$ holding $\tilde{m}_s$ fixed, and the compact limit, where $x_s \to 0$ and $\tilde{m}_s \to \infty$. These scaling relationships for compact sources are presented in Table 2. Together, they provide a guide to the boundary conditions that should be applied at the surface of the source, allowing our results to be extrapolated to still more compact sources without the need to solve for the full behaviour of the field.

The key observations can be summarised as follows:

Coupling	Dimensions	$\left.\dfrac{\phi}{\bar{\phi}_\infty}\right|_{r=r_s}$	$\left.\dfrac{\mathbf{r}\cdot\boldsymbol{\nabla}\phi}{\bar{\phi}_\infty}\right|_{r=r_s}$
$\dfrac{\rho}{M}\,\phi$	$d=3$	$-\dfrac{0.39\tilde{m}_s^{1/3}}{x_s}$	$\dfrac{0.17\tilde{m}_s^{2/3}}{x_s}$
	$d=2$	$-\dfrac{8.51\tilde{m}_s}{x_s^{0.06}[1+2.05(\tilde{m}_s x_s)^{0.59}]}$	$\dfrac{0.19\tilde{m}_s}{1+0.54(\tilde{m}_s x_s)^{0.39}}$
$\dfrac{\rho}{2M^2}\,\phi^2$	$d=3$	$1-\dfrac{1}{1+2.16(x_s/\tilde{m}_s)^{0.50}}$	$1+0.67x_s$
	$d=2$	$1-\dfrac{1}{1+(x_s^{0.16}/\tilde{m}_s^{0.53})}$	$0.25\,x_s^{1-0.44}\times$ $10^{0.44\sqrt{\log^2 x_s+1.86}}$

Table 2: Summary of scaling relationships for ϕ and $\mathbf{r}\cdot\boldsymbol{\nabla}\phi$ at the surface of compact sources ($r=r_s$), expressed in terms of the dimensionless source radius x_s and the dimensionless source mass $\tilde{m}_s$ (see Table 1). We reiterate that "two dimensional" versus "three dimensional" refers here to cylindrically and spherically symmetric problems, respectively. For the linearly coupled model, the scaling relations hold for $x_s \in [10^{-6}, 1]$, $\tilde{m}_s \in [10^{1.5}, 10^6]$. For the quadratically coupled model in $d=3$, the ranges are $x_s \in [10^{-3}, 10^{-0.5}]$, $\tilde{m}_s \in [10^{1.5}, 10^3]$. For the quadratically coupled model in $d=2$ and the scaling relation for $\phi/\bar{\phi}_\infty|_{r=r_s}$, the ranges are $x_s \in [10^{-3}, 10^{-2}]$, $\tilde{m}_s \in [10^{1.5}, 10^3]$. For the quadratically coupled model in $d=2$ and the scaling relation for $\mathbf{r}\cdot\boldsymbol{\nabla}\phi/\bar{\phi}_\infty|_{r=r_s}$, the ranges are $x_s \in [10^{-3}, 10^{-0.5}]$, $\tilde{m}_s \in [10^{1.5}, 10^3]$. Coefficients that have been determined numerically are given to two decimal places.

Linear coupling, $d=3$: Both the field and its gradient diverge at the surface of the source as the source becomes more compact. We note that the value of the field at the surface of the source scales with $\rho^{1/3}$, tracking the minimum of the effective potential ($V_{\text{eff}}(\phi) \sim \lambda\phi^4/4 + \rho\phi/M$ when the $-\mu^2\phi^2/2$ term is negligible), as discussed in Section 4.2.4 and Fig. 10.

Linear coupling, $d=2$: The field diverges at the surface of the source as the source becomes more compact. The behaviour of the gradient

of the field at the surface of the source depends on the way in which the limit is taken. In the point-like limit, where $\tilde{m}_s$ is held fixed and $x_s \to 0$, the gradient of the field at the surface of the source tends to a fixed value. If x_s is held fixed and the mass of the source is increased, the gradient of the field at the surface of the source diverges.

Quadratic coupling, $d = 3$: The field tends to zero, the minimum of the screened symmetron potential $V_{\text{eff}}(\phi) = \lambda\phi^4/4 + (\rho - \mu^2/M^2)\phi^2/2$ for $\rho > \mu^2 M^2$, at the surface of the source as the source becomes more compact. In the compact limit, the gradient of the field at the surface of the source diverges as $1/r_s$, in agreement with our expectations from Derrick's theorem that either the field or its gradient must diverge for Eq. (4.6b) to be satisfied in $d > 2$.

Quadratic coupling, $d = 2$: The field tends to zero at the surface of the source as the source becomes more compact. The field gradient is independent of the source mass and scales as a function of the source radius only.

The above behaviours agree with the inferences drawn from Derrick's theorem in Sec. 4.1 in three spatial dimensions. Derrick's theorem does not allow similar inferences to be drawn in two spatial dimensions. We note that in the limit that the source becomes point-like, the field profiles may not be continuous functions, but instead be distributions, reflecting the nature of the delta-function source. We also note that, for $d > 1$, we find no indication of the breakdown phenomenon identified in Ref. [14] in $d = 1$ for the linearly coupled model.
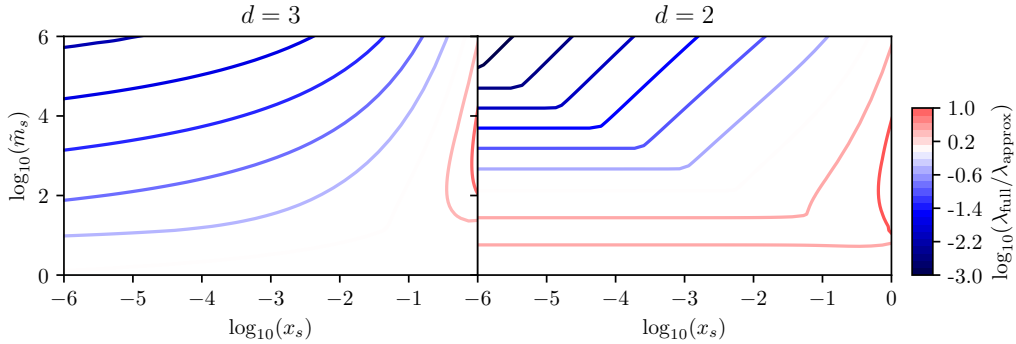
4.3.2   Screening factors

Having obtained full numerical solutions, we can determine screening factors without approximation. This allows us to validate existing calculations based on approximate analytic solutions, such as those presented in Secs. 1.3.1 and 1.3.2.

In Fig. 11, we compare the analytic expressions for the screening factors that appear in Eqs. (1.20) and (1.27) with those obtained from Eqs. (1.19) and (1.26) using the field gradients from the full numerical solutions. We refer to the former as λ_{approx} and the latter as λ_{full}. We note that λ_{full} depends on the distance from the source but tends to a constant at large distances. We
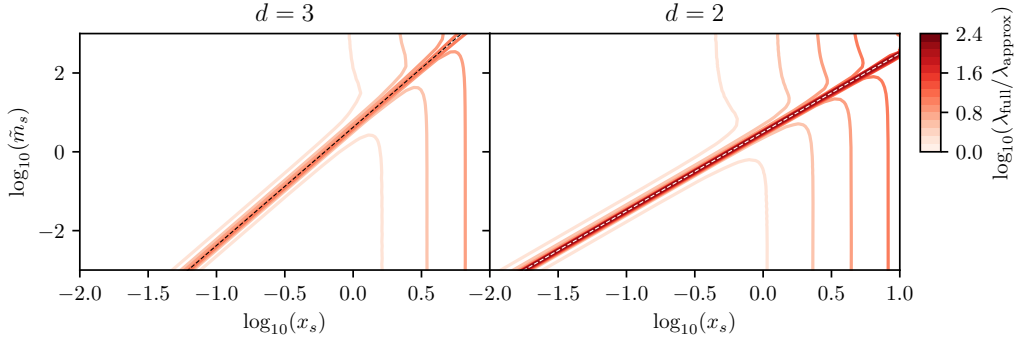
(a) Quadratically coupled model: The analytically derived, approximate screening factor becomes highly accurate for small source radii. However, large deviations occur when $\rho \sim \mu^2 M^2$, because the effective mass of the scalar goes to zero inside the source, and the non-linear terms in the potential dominate. This behaviour cannot be captured by a piecewise linear approximation to the potential, and no analytic prediction is available. The black ($d = 3$) and white ($d = 2$) dashed lines indicate where $\rho = \mu^2 M^2$.

(b) Linearly coupled model: In both the spherically and cylindrically symmetric cases ($d = 3$ and $d = 2$), the full screening factor is poorly approximated by the analytically derived expression for compact sources, corresponding to the upper left regions of the plots.

Figure 11: Logarithm of the ratio of the screening factors λ_{full} and λ_{approx}, as obtained from the full and approximate field profiles for (a) the quadratically coupled model and (b) the linearly coupled model, and for spherically ($d = 3$) and cylindrically ($d = 2$) symmetric sources. The quartic self-coupling was taken to be $\lambda = 0.1$.

74

therefore compare the screening factors at a radius of $10/x_s$, which proves to be sufficiently distant for all cases. For positive-definite and perturbative values of the quartic self-coupling λ, we expect results qualitatively similar to those shown in Fig. 11.

The comparisons of the screening factors can be summarised as follows:

Quadratic coupling (Fig. 11a): We find that $\lambda_{\text{full}} \geq \lambda_{\text{approx}}$, such that the approximate analytic solutions generally *overestimate* the degree of screening. This is because the full numerical field profiles have a smaller gradient in the vicinity of the source compared to the analytic approximation. As a result, the full numerical field profiles must have a larger gradient at greater distances from the source in order to reach the vev. We also find that the ratio $\lambda_{\text{full}}/\lambda_{\text{approx}}$ depends mostly on the source radius x_s in the $\rho > \mu^2 M^2$ region ($\tilde{m}_s > \Omega_d x_s^d/d$), tending to 1 as $x_s \to 0$, while the source mass $\tilde{m}_s$ is only relevant for small masses. The disappearance of vertical contours for $x_s \lesssim 1$ (with the exception of the region around $\rho = \mu^2 M^2$) results from the complete symmetry restoration at the centre of the source: once the symmetry is fully restored there, a further decrease in the radius of the source has no effect.

Most notable are the large deviations of λ_{full} from λ_{approx} that appear close to $\rho = \mu^2 M^2$. At this critical density, the effective mass of the scalar goes to zero inside the source. The potential is then dominated by the ϕ^4 term, and the analytic approximations become invalid. This leads to a significant enhancement in the ratio $\lambda_{\text{full}}/\lambda_{\text{approx}}$.

Linear coupling (Fig. 11b): While we observe contours along which $\lambda_{\text{approx}} = \lambda_{\text{full}}$ (in the $\tilde{m}_s > 1$ and $x_s < 1$ region of the parameter space), there is poor agreement between λ_{approx} and λ_{full} across the remainder of the parameter space. In contrast to the quadratically coupled case and for increasingly compact sources, $\lambda_{\text{approx}} > \lambda_{\text{full}}$, such that the degree of screening is *underestimated* by the analytic approximations. In the spherically symmetric case ($d = 3$), there is a transition at small $\tilde{m}_s$, where the equation for r_{shell} (1.28) has no real solutions and, consequently, the approximate screening factor becomes a constant $\lambda_{\text{approx}} = 1$. For $x_s \to 0$, this occurs when $\tilde{m}_s < 2^{3/2} \cdot 4\pi/3 \approx 11.8$. In the cylindrically symmetric case ($d = 2$), we see that the ratio of the screening factors becomes independent of the source radii for suffi-

ciently small source masses (see Tab. 2).

Overall, for the linearly coupled model, the analytic approximations provide a poor estimate of the degree of screening for compact sources. On the other hand, the analytic approximations provide a reasonable reflection of the true degree of screening for the quadratically coupled model. The important exception to this is the region of parameter space where the source nears the critical density $\rho \sim \mu^2 M^2$ and for which the effective mass of the scalar inside the source goes to zero. Interestingly, this is also the region corresponding to more diffuse sources, which may have phenomenological implications for astrophysical objects, such as nebulae. We remark that this more strongly non-linear region of parameter space has previously been identified as interesting in the context of disk galaxies [128–130]. However, we leave its detailed study to future work. This is not least because quantum corrections may play an important role here (see also Sec. 4.3.3), at the very least renormalising the condition that defines the critical density.

4.3.3   Quantum corrections

Throughout this section, we have studied the solutions to the classical equations of motion, implicitly assuming that, as long as we abide by models in which Eq. (2.40) or Eq. (2.43) holds, quantum corrections can be neglected. Nevertheless, not only were those bounds qualified by the assumption that the field does not travel too far from its minimum, we also only considered the impact of corrections to the potential in Sec. 2.2, in effect assuming that gradient terms are negligible, whereas field profiles in the vicinity of point-like sources feature large field gradients and therefore we might still expect quantum corrections to become important. More precisely, if the classical solution is to be valid, we require the quantum fluctuations to be subdominant once smoothed over scales smaller than the characteristic length scale of the classical solution, where the latter is proportional to the Compton wavelength of the field. The arguments that follow are based on those made in Ref. [131] and references therein.

To make the quantum nature of the corrections clear, in this section we will include $\hbar$ explicitly, and to keep λ dimensionless in $d = 3$, we maintain $[\mu] = \text{mass}$ and $[\phi] = \text{mass}^{(d-1)/2}$.

Our aim is to find a smoothing length L that satisfies two criteria:

(i)
$$L \ll \epsilon \hbar \mu^{-1} \ ,$$

i.e., the length L is smaller than the characteristic length scale of variations in the classical configuration. Assuming that the field rolls to the vev in about one Compton wavelength gives $\epsilon \sim 1$. On the other hand, for highly compact sources, we expect $\epsilon \ll 1$, as we will discuss below.

(ii) $$(\Delta\phi_L)_{\text{QM}} \ll (\Delta\phi_L)_{\text{CL}} \ ,$$
 i.e., the quantum fluctuations smoothed over an interval of length L are smaller than the change in the classical solution over the same interval.

Since we will only be considering fields with non-vanishing mass in vacuum, we can always choose L such that (i) is satisfied.

We note that, if the conditions (i) and (ii) are not met, it does not mean that the classical solution is invalid or uninteresting. Instead, this indicates only that one should look more closely at the predictivity of the classical approximation in this regime.

The change in the classical field configuration over the distance L is approximately

$$(\Delta\phi_L)_{\text{CL}} \sim \frac{\mathrm{d}\phi}{\mathrm{d}r}L \sim \frac{\mu^2 L}{\epsilon\hbar\sqrt{\lambda}} \ , \tag{4.17}$$

where we have taken $\bar{\phi}_\infty/(\epsilon\hbar\mu^{-1})$ to approximate the derivative in the vicinity of the source, viz. where the derivative is at its largest.

In order to estimate the quantum mechanical fluctuations, we first smear the quantum field over an interval of length L. This can be done by taking the average of the field over all space, weighted by a Gaussian of width L:

$$\phi_L(\mathbf{x}) = \frac{1}{(2\pi L^2)^{d/2}} \int \mathrm{d}^d\mathbf{y} \ e^{-(\mathbf{y}-\mathbf{x})^2/(2L^2)}\phi(\mathbf{y}) \ . \tag{4.18}$$

Placing x at the origin without loss of generality, we find

$$
\begin{aligned}
(\Delta\phi_L)_{\text{QM}}^2 &= \langle 0| \phi_L(0)^2 |0\rangle \ , \\
&= \frac{1}{(2\pi L^2)^d} \int \mathrm{d}^d\mathbf{y} \ \mathrm{d}^d\mathbf{z} \ e^{-(\mathbf{y}^2+\mathbf{z}^2)/(2L^2)} \langle 0| \phi(\mathbf{y})\phi(\mathbf{z}) |0\rangle \\
&= \frac{\hbar^{d-1}}{(2\pi L^2)^d} \int \mathrm{d}^d\mathbf{y} \ \mathrm{d}^d\mathbf{z} \ e^{-(\mathbf{y}^2+\mathbf{z}^2)/(2L^2)} \int \frac{\mathrm{d}^d\mathbf{k}}{(2\pi)^d} \frac{e^{-i\mathbf{k}\cdot(\mathbf{y}-\mathbf{z})}}{2\sqrt{\mathbf{k}^2+\mu^2/\hbar^2}} \ .
\end{aligned}
\tag{4.19}
$$

After performing the spatial integrals, we are left with

$$(\Delta\phi_L)^2_{\rm QM} = \hbar^{d-1} \int \frac{\mathrm{d}^d\mathbf{k}}{(2\pi)^d} \frac{e^{-\mathbf{k}^2 L^2}}{2\sqrt{\mathbf{k}^2 + \mu^2/\hbar^2}} \tag{4.20}$$

$$\sim \hbar^{d-1} \int \mathrm{d}\Omega_d \int_0^{L^{-1}} dk \, \frac{k^{d-1}}{\sqrt{k^2 + \mu^2/\hbar^2}} \underset{L\mu\ll\hbar}{\sim} \frac{\hbar^{d-1}}{L^{d-1}} \, . \tag{4.21}$$

Hence, in order to satisfy the condition (ii) above, we must be able to find an L such that

$$\hbar^{\frac{d+1}{2}} \frac{\epsilon\sqrt{\lambda}}{\mu^2} \ll L^{\frac{d+1}{2}} \, . \tag{4.22}$$

In other words, we must be able to choose L to be large enough that quantum fluctuations are under control. Combining this with the condition (i), we therefore require that

$$\lambda \ll \frac{\epsilon^{d-1}}{\mu^{d-3}} = \begin{cases} \epsilon^2, & d = 3 \\ \mu\epsilon, & d = 2 \end{cases} \, . \tag{4.23}$$

(We note that λ has dimensions of mass in two spatial dimensions.)

From our analytic and numerical results, we have seen that $\epsilon \ll 1$ for small, dense sources, and our arguments from Derrick's theorem in Sec. 4.1 suggest that $\epsilon \to 0$ for point sources. That is to say, although the classical solution varies rapidly in the vicinity of the point source and goes to zero, the quantum fluctuations are sufficiently large that they swamp the classical behaviour. Notice that this is not the case in $d = 1$, for which we require $\lambda \ll \mu$, independent of ϵ, such that we can always find a coupling small enough that the quantum effects are suppressed. A comprehensive analysis of the quantum corrections to the scalar field profiles presented here is beyond the scope of this work.

4.4   Conclusions

The aim of this section was to study the screening of fifth forces around extremely compact sources that are effectively point-like compared to the Compton wavelength of the scalar fifth-force mediator. To this end, we have derived a generalisation of Derrick's theorem in the presence of external sources, which allowed us to infer the behaviours of the scalar field as the

78

compactness of these sources is increased. These behaviours were confirmed in two and three spatial dimensions by analysing the full numerical solutions for the scalar field in models with a spontaneous symmetry breaking potential and a linear or quadratic coupling to the matter source (at the level of the action). We found that fields with a quadratic coupling are driven to zero in the vicinity of point-like sources, whereas fields with a linear coupling diverge. In addition, the numerically obtained field profiles were compared to novel piecewise analytic solutions that extend the piecewise approximations typically applied in the literature.

By these means, we have been able to establish a set of scaling relationships from which the behaviour of the scalar fields and their boundary conditions at the surface of the source can be extrapolated to other sources. These are shown in Table 2. In addition, we have undertaken a critical assessment of the validity of existing screening conditions extracted from so-called screening factors. For the linearly coupled model, this has provided a refined estimate of screening over a large region of parameter space. On the other hand, for the quadratically coupled model, we find reasonable agreement with existing screening estimates in the screened regime, except in the region of parameter space where the source has the critical density for which the field effectively become massless and the field equation becomes unavoidably nonlinear. Here, we find that existing approximations significantly overestimate the amount of screening, the screening factors obtained numerically differing from those derived analytically by factors of up to $10^{2.4}$. Since this region of parameter space corresponds to diffuse sources, there may be potential implications for astrophysical systems, such as nebulae, which warrant further study. The comparisons between the screening factors extracted from our numerical results and those based on existing approximations are shown in Fig. 11.

5   Conclusions

In this thesis we have looked at theories of scalar fields which mediate screened fifth forces, and the effects of non-minimal couplings to the Ricci scalar, quantum corrections, and non-linearities on the validity of linearised equations of motion as approximations to these theories.

In Sec. 2, we studied the impact of non-minimal couplings and quantum corrections on the physics of scalar fields, with the goal of determining when a minimally-coupled classical equation of motion of the form $\Box\varphi = V'(\varphi)$ is a suitable approximation to the full dynamics of φ. To achieve this, we analysed the transformation between the Jordan frame, in which a non-minimal coupling is explicitly present between the scalar field and the Ricci scalar, and the Einstein frame, in which the non-minimal coupling is obscured when in vacuum, and discovered that the physics of the non-minimal coupling is found in the transformed potential and scalar field. Through this, we were able to quantify the contributions of the non-minimal coupling to the equation of motion, and thereby determine sets of bounds, Eqs. (2.40) and (2.43), for the symmetron model in which these contributions dominate over the quantum corrections while remaining negligible compared to the minimally-coupled classical equation of motion.

In Secs. 3 and 4, we turned our attention to non-linearities in the effective potential and whether or not a linearised equation of motion $\Box\varphi = \mu_\varphi^2 \varphi$ can be a suitable approximation to $\Box\varphi = V'_{\text{eff}}(\varphi)$. This depends on the context and so the two sections study two different scenarios.

In Sec. 3, our focus was on black hole superradiance, an astrophysical phenomenon that relies only on waves being able to feel the gravity of a black hole and can therefore be used to search for a variety of new bosons. We firstly estimated the timescales for single-particle fluctuations in symmetron and chameleon fields to be amplified by superradiance to the point that non-linearities can no longer be neglected, and confirmed that these timescales are small on a cosmological scale. This was followed by our generalisation of a previously established method in which a non-relativistic expression for the energy contained within a superradiating field is derived and used to estimate what happens when the number of particles in the field increases. Contrary to the case of axion-like particles, where a 'bosenova' causes a large and sudden release of potentially detectable gravitational radiation, when we applied this to symmetrons and chameleons we saw hints that non-linearities would hinder the increase in particle number and consequently render the

effects of superradiance less observable.

In Sec. 4, our focus was on the screening of fifth forces around sources that are taken to the limit of zero radius. We derived an extension of Derrick's theorem in the presence of sources, generated full numerical solutions to the symmetron and symmetron-like chameleon equations of motion around spherically and cylindrically symmetric sources, and obtained scaling relationships (Table 2) and screening factors (Fig. 11) for both theories. We found that symmetron field profiles are driven to zero in the vicinity of point-like sources, and a comparison of numerically-obtained screening factors to their previously calculated analytical counterparts shows that the established analytical methods are suitable for dealing with the symmetron except for when the source has a density close to the critical density of the theory, which is when the equation of motion cannot be linearised and so the analytical approximations cease to be valid. When the symmetron's quadratic coupling is exchanged for a linear coupling to produce a chameleon theory, we found that field profiles diverge in the vicinity of point sources, and our numerical methods extend the parameter space beyond that in which analytical methods can provide reliable approximations.

I will conclude by commenting on the possible future directions highlighted by the work on non-linearities in Secs. 3 and 4.

On the topic of black hole superradiance, the most recent research by Baryakhtar *et al.* [95] and Omiya *et al.* [97] has yet to reach a consensus on whether non-perturbative effects, such as those studied in Sec. 3, will in fact occur in realistic systems. If the answer turns out to be positive then further studies, such as numerical calculations, will have to be conducted in order to determine more fully whether black hole superradiance is a useful probe of screened fifth forces or whether its applicability is limited to theories such as those of $\frac{1}{2}\mu_\varphi^2\varphi^2$ potentials and axion-like particles.

In Sec. 4, we have laid the foundations for studying the conditions under which distributions of discrete sources can be treated approximately as continuous density distributions for the purpose of analysing screening. A natural first step towards addressing this question is the extension of this work to systems of two (or more) point-like sources, as were studied analytically in one spatial dimension in Ref. [14]. Additionally, the results of this work should be extended to curved spacetimes and time-dependent settings. For instance, in the linearly coupled model, we identified that the explicit breaking of the $\mathbb{Z}_2$ symmetry ($\phi \to -\phi$) by the matter coupling may give rise to an instability. As such, the increasing compactness of a collapsing matter

source has the potential to induce a transition in the scalar field from one vacuum external to the source to another. Whether this transition is realised, and the phenomenological implications that it might have, warrants further investigation. Finally, we have identified the regions of parameter space in which it may be necessary to account for quantum corrections to the scalar field profiles in the vicinity of compact sources, since the latter induces large spatial gradients in the field. The treatment of these effects requires us to find the quantum corrections to spatially varying classical field profiles, and the relevant self-consistent procedures for dealing with such calculations have been developed in the context of vacuum decay [132, 133].

A Example construction of a piecewise solution

In this appendix, we show the explicit construction of a piecewise analytic field profile, as discussed in Sec. 4.2.1. We consider a spherical source in the quadratically coupled model, where the conditions for smoothly matching the approximations to the scalar field profile can be solved analytically. We will construct here a three-part solution. We make one approximation to the form of the potential inside the source, assuming that the effective potential has the form of Eq. (4.9), and two approximations to the potential outside the source — the lower two approximations in Eq. (4.8). The field profile is then

$$
\phi(x) = \bar{\phi}_\infty \begin{cases} A\frac{\sinh(\nu x)}{x} \ , & x \le x_s \\ -\frac{x^2}{18} + \frac{C_1}{x} + C_2 \ , & x_s \le x \le x_2 \ , \\ 1 - \frac{x_2}{6x} e^{-\sqrt{2}(x-x_2)} \ , & x_2 \le x \end{cases} \qquad \text{(A.1)}
$$

where

$$
A = -\frac{2x_2^3 + 3x_2^2(\sqrt{2} - x_s) - 18x_s + x_s^3 + x_2(3 - 3\sqrt{2}x_s)}{18 \sinh(\nu x_s)} \ , \qquad \text{(A.2a)}
$$

$$
C_1 = -\frac{3x_2 + 3\sqrt{2}x_2^2 + 2x_2^3}{18} \ , \qquad \text{(A.2b)}
$$

$$
C_2 = 1 + \frac{\sqrt{2}x_2}{6} + \frac{x_2^2}{6} \ , \qquad \text{(A.2c)}
$$

and x_2 is the solution to

$$
\frac{(x_s - x_2)(x_s + 2x_2) - 3(1 + \sqrt{2}x_2) + 15x_s}{x_s(x_2 - x_s)^2 + 3(x_2 - 1)(1 + \sqrt{2}x_2) + 15x_s} = \frac{\tanh \nu x_s}{\nu x_s} \ . \qquad \text{(A.3)}
$$

For this solution to be consistent, we must check that $\bar{\phi}_\infty/3 \le \phi(r_s) < 5\bar{\phi}_\infty/6$.

B   The initial guess

At the end of Sec. 4.2.4, we described how the initial guess for the Newton's algorithm is found by numerically solving a series of linearised equations of motion. In this appendix, we give further details of that procedure. We use `FEniCS` to solve the linearised equation of motion

$$\nabla^2\phi - m^2\phi = b + c\rho \tag{B.1}$$

in four spatial regions: one inside the source and three nested shells outside the source. In these regions, the coefficients m^2, b and c in Eq. (B.1) are defined as follows:

	$r < r_s$	$r_s \leq r < r_1$	$r_1 \leq r < r_2$	$r_2 \leq r$
m^2	$\tilde{\nu}^2\mu^2$	$-\mu^2$	0	$2\mu^2$
b	$-s_b\mu^2\bar{\phi}_\infty$	0	$-1/3\,\mu^2\bar{\phi}_\infty$	$-2\mu^2\bar{\phi}_\infty$
c	s_c/M	0	0	0

where the coefficients ν^2, s_b and s_c are assigned the following values depending on the source density:

Linear coupling				Quadratic coupling		
	$\tilde{\rho} > 1$	$1 \geq \tilde{\rho} > \sqrt{12}/9$	$\tilde{\rho} \leq \sqrt{12}/9$		$\tilde{\rho} > 1$	$\tilde{\rho} < 1$
$\tilde{\nu}^2$	-1	2	ν^2	$\tilde{\nu}^2$	$\tilde{\rho}-1$	$2(1-\tilde{\rho})$
s_b	0	2	$-\nu^2\tilde{\rho}^{1/3}$	s_b	0	$2\,(1-\tilde{\rho})^{3/2}$
s_c	1	1	0	s_c	0	0
$\tilde{\rho} = \sqrt{\lambda}\rho/(\mu^3 M)$				$\tilde{\rho} = \rho/(\mu M)^2$		

To determine the matching radii r_1 and r_2, we first establish which of the approximating regimes described in Sec. 4.2.1 is appropriate. After deriving the matching conditions analytically, as outlined for an example solution in Appendix A, we solve them numerically. When a two-part solution is the correct approximation, the columns $r_s \leq r < r_1$ and $r_1 \leq r < r_2$ above are ignored. Similarly, when a three-part solution is the correct approximation, the column $r_s \leq r < r_1$ is ignored.

As we do not use the full form of Eq. (4.11), the linearly coupled sources with $\tilde{\rho} > \sqrt{12}/9$ are split into high-density ($\tilde{\rho} > 1$) and medium-density ($1 \geq \tilde{\rho} > \sqrt{12}/9$) regimes. For the former, we make an approximation that the matter coupling dominates over the non-linear term in the potential, such that $\nabla^2\phi = -\mu^2\phi + \rho/M$ provides us with a suitable initial guess; for the

84

latter, we take the matter coupling to only slightly displace the field from the vev, such that $\nabla^2 \phi = 2\mu^2(\phi - \bar{\phi}_\infty) + \rho/M$ is the equation that we use.

For the quadratically coupled model, when $\tilde{\rho} = 1$, the analytic approximations described in Sec. 4.2.1 fail. In this case, we set $\tilde{\nu} = 10^{-10}$. To obtain the matching radii, we further set $\bar{\phi}(\rho)/m_r = 10^{-10}$, where m_r is a rescaling mass that we use to make the field dimensionless (see Appendix A of Ref. [120]). This choice shifts the initial guess slightly away from the critical density $\rho = (\mu M)^2$, and we find it leads to fast convergence for all the parameter ranges examined in this thesis.

References

[1] R. M. Wald, *General Relativity.* Chicago, USA: Chicago Univ. Pr., 1984.

[2] C. M. Will, "The Confrontation between General Relativity and Experiment," *Living Rev. Rel.*, vol. 17, p. 4, 2014.

[3] N. Aghanim *et al.*, "Planck 2018 results. VI. Cosmological parameters," *Astron. Astrophys.*, vol. 641, p. A6, 2020.

[4] G. Bertone, D. Hooper, and J. Silk, "Particle dark matter: Evidence, candidates and constraints," *Phys. Rept.*, vol. 405, pp. 279–390, 2005.

[5] A. Joyce, B. Jain, J. Khoury, and M. Trodden, "Beyond the Cosmological Standard Model," *Phys. Rept.*, vol. 568, pp. 1–98, 2015.

[6] Y. Akrami *et al.*, "Planck 2018 results. X. Constraints on inflation," *Astron. Astrophys.*, vol. 641, p. A10, 2020.

[7] D. Lovelock, "The Einstein tensor and its generalizations," *J. Math. Phys.*, vol. 12, pp. 498–501, 1971.

[8] D. Lovelock, "The four-dimensionality of space and the einstein tensor," *J. Math. Phys.*, vol. 13, pp. 874–876, 1972.

[9] T. Clifton, P. G. Ferreira, A. Padilla, and C. Skordis, "Modified Gravity and Cosmology," *Phys. Rept.*, vol. 513, pp. 1–189, 2012.

[10] F. Englert and R. Brout, "Broken Symmetry and the Mass of Gauge Vector Mesons," *Phys. Rev. Lett.*, vol. 13, pp. 321–323, 1964. [,157(1964)].

[11] P. W. Higgs, "Broken Symmetries and the Masses of Gauge Bosons," *Phys. Rev. Lett.*, vol. 13, pp. 508–509, 1964. [,160(1964)].

[12] G. S. Guralnik, C. R. Hagen, and T. W. B. Kibble, "Global Conservation Laws and Massless Particles," *Phys. Rev. Lett.*, vol. 13, pp. 585–587, 1964. [,162(1964)].

[13] L. Hui, J. P. Ostriker, S. Tremaine, and E. Witten, "Ultralight scalars as cosmological dark matter," *Phys. Rev. D*, vol. 95, no. 4, p. 043541, 2017.

[14] C. Burrage, B. Elder, and P. Millington, "Particle level screening of scalar forces in 1+1 dimensions," *Phys. Rev.*, vol. D99, no. 2, p. 024045, 2019.

[15] E. G. Adelberger, J. H. Gundlach, B. R. Heckel, S. Hoedl, and S. Schlamminger, "Torsion balance experiments: A low-energy frontier of particle physics," *Prog. Part. Nucl. Phys.*, vol. 62, pp. 102–134, 2009.

[16] G. L. Klimchitskaya, "Constraints on Theoretical Predictions Beyond the Standard Model from the Casimir Effect and Some Other Tabletop Physics," *Universe*, vol. 7, no. 3, p. 47, 2021.

[17] S. M. Merkowitz, "Tests of Gravity Using Lunar Laser Ranging," *Living Rev. Rel.*, vol. 13, p. 7, 2010.

[18] C. Talmadge, J. P. Berthias, R. W. Hellings, and E. M. Standish, "Model Independent Constraints on Possible Modifications of Newtonian Gravity," *Phys. Rev. Lett.*, vol. 61, pp. 1159–1162, 1988.

[19] L. Iorio, "Constraints on the range lambda of Yukawa-like modifications to the Newtonian inverse-square law of gravitation from Solar System planetary motions," *JHEP*, vol. 10, p. 041, 2007.

[20] K. Hinterbichler and J. Khoury, "Screening Long-Range Forces Through Local Symmetry Restoration," *Phys. Rev. Lett.*, vol. 104, p. 231301, 2010.

[21] C. Burrage, E. J. Copeland, and P. Millington, "Radiative Screening of Fifth Forces," *Phys. Rev. Lett.*, vol. 117, no. 21, p. 211102, 2016.

[22] K. Hinterbichler, J. Khoury, A. Levy, and A. Matas, "Symmetron cosmology," *Phys. Rev.*, vol. D84, p. 103521, 2011.

[23] C. Burrage, A. Kuribayashi-Coleman, J. Stevenson, and B. Thrussell, "Constraining symmetron fields with atom interferometry," *JCAP*, vol. 1612, p. 041, 2016.

[24] J. Khoury and A. Weltman, "Chameleon fields: Awaiting surprises for tests of gravity in space," *Phys. Rev. Lett.*, vol. 93, p. 171104, 2004.

[25] C. Burrage and J. Sakstein, "Tests of Chameleon Gravity," *Living Rev. Rel.*, vol. 21, no. 1, p. 1, 2018.

[26] P. Brax, C. van de Bruck, A.-C. Davis, and D. Shaw, "The Dilaton and Modified Gravity," *Phys. Rev.*, vol. D82, p. 063519, 2010.

[27] I. Navarro and K. Van Acoleyen, "f(R) actions, cosmic acceleration and local tests of gravity," *JCAP*, vol. 02, p. 022, 2007.

[28] T. Faulkner, M. Tegmark, E. F. Bunn, and Y. Mao, "Constraining f(R) Gravity as a Scalar Tensor Theory," *Phys. Rev. D*, vol. 76, p. 063505, 2007.

[29] P. Brax, C. van de Bruck, A.-C. Davis, and D. J. Shaw, "f(R) Gravity and Chameleon Theories," *Phys. Rev. D*, vol. 78, p. 104021, 2008.

[30] J. Khoury and A. Weltman, "Chameleon cosmology," *Phys. Rev.*, vol. D69, p. 044026, 2004.

[31] C. Burrage, E. J. Copeland, and E. A. Hinds, "Probing Dark Energy with Atom Interferometry," *JCAP*, vol. 1503, no. 03, p. 042, 2015.

[32] M. Pernot-Borràs, J. Bergé, P. Brax, and J.-P. Uzan, "General study of chameleon fifth force in gravity space experiments," *Phys. Rev. D*, vol. 100, no. 8, p. 084006, 2019.

[33] A. Upadhye, S. S. Gubser, and J. Khoury, "Unveiling chameleon fields in tests of the gravitational inverse-square law," *Phys. Rev. D*, vol. 74, p. 104024, 2006.

[34] A. Upadhye, "Dark energy fifth forces in torsion pendulum experiments," *Phys. Rev. D*, vol. 86, p. 102003, 2012.

[35] P. Brax, C. van de Bruck, A.-C. Davis, D. F. Mota, and D. J. Shaw, "Detecting chameleons through Casimir force measurements," *Phys. Rev. D*, vol. 76, p. 124034, 2007.

[36] P. Brax, C. van de Bruck, A. C. Davis, D. J. Shaw, and D. Iannuzzi, "Tuning the Mass of Chameleon Fields in Casimir Force Experiments," *Phys. Rev. Lett.*, vol. 104, p. 241101, 2010.

[37] A. Almasi, P. Brax, D. Iannuzzi, and R. I. P. Sedmik, "Force sensor for chameleon and Casimir force experiments with parallel-plate configuration," *Phys. Rev. D*, vol. 91, no. 10, p. 102002, 2015.

[38] P. Hamilton, M. Jaffe, P. Haslinger, Q. Simmons, H. Müller, and J. Khoury, "Atom-interferometry constraints on dark energy," *Science*, vol. 349, pp. 849–851, 2015.

[39] B. Elder, J. Khoury, P. Haslinger, M. Jaffe, H. Müller, and P. Hamilton, "Chameleon dark energy and atom interferometry," *Phys. Rev. D*, vol. 94, no. 4, p. 044051, 2016.

[40] M. Jaffe, P. Haslinger, V. Xu, P. Hamilton, A. Upadhye, B. Elder, J. Khoury, and H. Müller, "Testing sub-gravitational forces on atoms from a miniature in-vacuum source mass," *Nature Phys.*, vol. 13, p. 938, 2017.

[41] D. O. Sabulsky, I. Dutta, E. Hinds, B. Elder, C. Burrage, and E. J. Copeland, "Experiment to detect dark energy forces using atom interferometry," *Phys. Rev. Lett.*, vol. 123, no. 6, p. 061102, 2019.

[42] P. Brax, G. Pignol, and D. Roulier, "Probing Strongly Coupled Chameleons with Slow Neutrons," *Phys. Rev. D*, vol. 88, p. 083004, 2013.

[43] H. Lemmel, P. Brax, A. N. Ivanov, T. Jenke, G. Pignol, M. Pitschmann, T. Potocar, M. Wellenzohn, M. Zawisky, and H. Abele, "Neutron interferometry constrains dark energy chameleon fields," *Phys. Lett. B*, vol. 743, pp. 310–314, 2015.

[44] A. D. Rider, D. C. Moore, C. P. Blakemore, M. Louis, M. Lu, and G. Gratta, "Search for screened interactions associated with dark energy below the 100 μm length scale," *Phys. Rev. Lett.*, vol. 117, no. 10, p. 101101, 2016.

[45] J.-P. Uzan, M. Pernot-Borràs, and J. Bergé, "Effects of a scalar fifth force on the dynamics of a charged particle as a new experimental

design to test chameleon theories," *Phys. Rev. D*, vol. 102, no. 4, p. 044059, 2020.

[46] A. Upadhye, "Symmetron dark energy in laboratory experiments," *Phys. Rev. Lett.*, vol. 110, no. 3, p. 031301, 2013.

[47] B. Elder, V. Vardanyan, Y. Akrami, P. Brax, A.-C. Davis, and R. S. Decca, "Classical symmetron force in Casimir experiments," *Phys. Rev. D*, vol. 101, no. 6, p. 064065, 2020.

[48] C. Llinares and P. Brax, "Detecting coupled domain walls in laboratory experiments," *Phys. Rev. Lett.*, vol. 122, no. 9, p. 091102, 2019.

[49] Y. V. Stadnik, "New bounds on macroscopic scalar-field topological defects from nontransient signatures due to environmental dependence and spatial variations of the fundamental constants," *Phys. Rev. D*, vol. 102, p. 115016, Dec. 2020.

[50] P. Brax, A.-C. Davis, B. Elder, and L. K. Wong, "Constraining screened fifth forces with the electron magnetic moment," *Phys. Rev. D*, vol. 97, no. 8, p. 084050, 2018.

[51] G. Cronenberg, P. Brax, H. Filter, P. Geltenbort, T. Jenke, G. Pignol, M. Pitschmann, M. Thalhammer, and H. Abele, "Acoustic Rabi oscillations between gravitational quantum states and impact on symmetron dark energy," *Nature Phys.*, vol. 14, no. 10, pp. 1022–1026, 2018.

[52] S. R. Coleman and E. J. Weinberg, "Radiative Corrections as the Origin of Spontaneous Symmetry Breaking," *Phys. Rev.*, vol. D7, pp. 1888–1910, 1973.

[53] R. Brito, V. Cardoso, and P. Pani, *Superradiance: New Frontiers in Black Hole Physics*, vol. 906. Springer, 2015.

[54] R. Vicente, V. Cardoso, and J. C. Lopes, "Penrose process, superradiance, and ergoregion instabilities," *Phys. Rev. D*, vol. 97, no. 8, p. 084032, 2018.

[55] S. R. Dolan, "Instability of the massive Klein-Gordon field on the Kerr spacetime," *Phys. Rev. D*, vol. 76, p. 084001, 2007.

[56] S. R. Dolan, "Superradiant instabilities of rotating black holes in the time domain," *Phys. Rev. D*, vol. 87, no. 12, p. 124026, 2013.

[57] R. Brito, S. Ghosh, E. Barausse, E. Berti, V. Cardoso, I. Dvorkin, A. Klein, and P. Pani, "Stochastic and resolvable gravitational waves from ultralight bosons," *Phys. Rev. Lett.*, vol. 119, no. 13, p. 131101, 2017.

[58] R. Brito, S. Ghosh, E. Barausse, E. Berti, V. Cardoso, I. Dvorkin, A. Klein, and P. Pani, "Gravitational wave searches for ultralight bosons with LIGO and LISA," *Phys. Rev. D*, vol. 96, no. 6, p. 064050, 2017.

[59] V. Cardoso, O. J. Dias, G. S. Hartnett, M. Middleton, P. Pani, and J. E. Santos, "Constraining the mass of dark photons and axion-like particles through black-hole superradiance," *JCAP*, vol. 03, p. 043, 2018.

[60] M. J. Stott and D. J. Marsh, "Black hole spin constraints on the mass spectrum and number of axionlike fields," *Phys. Rev. D*, vol. 98, no. 8, p. 083006, 2018.

[61] N. Fernandez, A. Ghalsasi, and S. Profumo, "Superradiance and the Spins of Black Holes from LIGO and X-ray binaries," 11 2019.

[62] L. Zu, L. Feng, Q. Yuan, and Y.-Z. Fan, "Stringent constraints on the light boson model with supermassive black hole spin measurements," *Eur. Phys. J. Plus*, vol. 135, p. 709, 2020.

[63] M. J. Stott, "Ultralight Bosonic Field Mass Bounds from Astrophysical Black Hole Spin," 9 2020.

[64] K. K. Y. Ng, S. Vitale, O. A. Hannuksela, and T. G. F. Li, "Constraints on ultralight scalar bosons within black hole spin measurements from LIGO-Virgo's GWTC-2," *Phys. Rev. Lett.*, vol. 126, no. 15, p. 151102, 2021.

[65] V. M. Mehta, M. Demirtas, C. Long, D. J. E. Marsh, L. Mcallister, and M. J. Stott, "Superradiance Exclusions in the Landscape of Type IIB String Theory," 11 2020.

[66] C. Ünal, F. Pacucci, and A. Loeb, "Properties of ultralight bosons from heavy quasar spins via superradiance," *JCAP*, vol. 05, p. 007, 2021.

[67] V. M. Mehta, M. Demirtas, C. Long, D. J. Marsh, L. McAllister, and M. J. Stott, "Superradiance in string theory," *Journal of Cosmology and Astroparticle Physics*, vol. 2021, p. 033, Jul 2021.

[68] C. Palomba *et al.*, "Direct constraints on ultra-light boson mass from searches for continuous gravitational waves," *Phys. Rev. Lett.*, vol. 123, p. 171101, 2019.

[69] L. Sun, R. Brito, and M. Isi, "Search for ultralight bosons in Cygnus X-1 with Advanced LIGO," *Phys. Rev. D*, vol. 101, no. 6, p. 063020, 2020. [Erratum: Phys.Rev.D 102, 089902 (2020)].

[70] R. Brito, V. Cardoso, and P. Pani, "Black holes as particle detectors: evolution of superradiant instabilities," *Class. Quant. Grav.*, vol. 32, no. 13, p. 134001, 2015.

[71] G. Ficarra, P. Pani, and H. Witek, "Impact of multiple modes on the black-hole superradiant instability," *Phys. Rev. D*, vol. 99, no. 10, p. 104019, 2019.

[72] A. Arvanitaki, M. Baryakhtar, S. Dimopoulos, S. Dubovsky, and R. Lasenby, "Black Hole Mergers and the QCD Axion at Advanced LIGO," *Phys. Rev. D*, vol. 95, no. 4, p. 043001, 2017.

[73] J. C. Degollado, C. A. Herdeiro, and E. Radu, "Effective stability against superradiance of Kerr black holes with synchronised hair," *Phys. Lett. B*, vol. 781, pp. 651–655, 2018.

[74] O. A. Hannuksela, K. W. Wong, R. Brito, E. Berti, and T. G. Li, "Probing the existence of ultralight bosons with a single gravitational-wave measurement," *Nature Astron.*, vol. 3, no. 5, pp. 447–451, 2019.

[75] S. D'Antonio *et al.*, "Semicoherent analysis method to search for continuous gravitational waves emitted by ultralight boson clouds around spinning black holes," *Phys. Rev. D*, vol. 98, no. 10, p. 103017, 2018.

[76] S. J. Zhu, M. Baryakhtar, M. A. Papa, D. Tsuna, N. Kawanaka, and H.-B. Eggenstein, "Characterizing the continuous gravitational-wave

signal from boson clouds around Galactic isolated black holes," *Phys. Rev. D*, vol. 102, no. 6, p. 063020, 2020.

[77] K. K. Ng, M. Isi, C.-J. Haster, and S. Vitale, "Multiband gravitational-wave searches for ultralight bosons," *Phys. Rev. D*, vol. 102, no. 8, p. 083020, 2020.

[78] G. Creci, S. Vandoren, and H. Witek, "Evolution of black hole shadows from superradiance," *Phys. Rev. D*, vol. 101, no. 12, p. 124051, 2020.

[79] A. Mathur, S. Rajendran, and E. H. Tanin, "Clockwork mechanism to remove superradiance limits," *Phys. Rev. D*, vol. 102, no. 5, p. 055015, 2020.

[80] V. Cardoso, I. P. Carucci, P. Pani, and T. P. Sotiriou, "Matter around Kerr black holes in scalar-tensor theories: scalarization and superradiant instability," *Phys. Rev. D*, vol. 88, p. 044056, 2013.

[81] C.-Y. Zhang, S.-J. Zhang, and B. Wang, "Superradiant instability of Kerr-de Sitter black holes in scalar-tensor theory," *JHEP*, vol. 08, p. 011, 2014.

[82] M. F. Wondrak, P. Nicolini, and J. W. Moffat, "Superradiance in Modified Gravity (MOG)," *JCAP*, vol. 12, p. 021, 2018.

[83] M. Khodadi, A. Talebian, and H. Firouzjahi, "Black Hole Superradiance in f(R) Gravities," 2 2020.

[84] R. Jiang, R.-H. Lin, and X.-H. Zhai, "Superradiance instability of the Kerr-like black hole in Einstein-bumblebee gravity," 8 2021.

[85] A. Arvanitaki and S. Dubovsky, "Exploring the String Axiverse with Precision Black Hole Physics," *Phys. Rev. D*, vol. 83, p. 044026, 2011.

[86] H. Kodama and H. Yoshino, "Axiverse and Black Hole," *Int. J. Mod. Phys. Conf. Ser.*, vol. 7, pp. 84–115, 2012.

[87] H. Yoshino and H. Kodama, "Bosenova collapse of axion cloud around a rotating black hole," *Prog. Theor. Phys.*, vol. 128, pp. 153–190, 2012.

[88] H. Yoshino and H. Kodama, "The bosenova and axiverse," *Class. Quant. Grav.*, vol. 32, no. 21, p. 214001, 2015.

93

[89] H. Saito and M. Ueda, "Mean-field analysis of collapsing and exploding bose-einstein condensates," *Physical Review A*, vol. 65, Mar 2002.

[90] P. B. Ferraz, T. W. Kephart, and J. a. G. Rosa, "Superradiant pion clouds around primordial black holes," 4 2020.

[91] A. Arvanitaki, M. Baryakhtar, and X. Huang, "Discovering the QCD Axion with Black Holes and Gravitational Waves," *Phys. Rev. D*, vol. 91, no. 8, p. 084011, 2015.

[92] A. D. Plascencia and A. Urbano, "Black hole superradiance and polarization-dependent bending of light," *JCAP*, vol. 04, p. 059, 2018.

[93] M. Isi, L. Sun, R. Brito, and A. Melatos, "Directed searches for gravitational waves from ultralight bosons," *Phys. Rev. D*, vol. 99, no. 8, p. 084042, 2019. [Erratum: Phys.Rev.D 102, 049901 (2020)].

[94] D. Blas and S. J. Witte, "Imprints of Axion Superradiance in the CMB," *Phys. Rev. D*, vol. 102, no. 10, p. 103018, 2020.

[95] M. Baryakhtar, M. Galanis, R. Lasenby, and O. Simon, "Black hole superradiance of self-interacting scalar fields," *Phys. Rev. D*, vol. 103, no. 9, p. 095019, 2021.

[96] H. Fukuda and K. Nakayama, "Aspects of Nonlinear Effect on Black Hole Superradiance," *JHEP*, vol. 01, p. 128, 2020.

[97] H. Omiya, T. Takahashi, and T. Tanaka, "Renormalization group analysis of superradiant growth of self-interacting axion cloud," 12 2020.

[98] R. Abbott *et al.*, "GWTC-2.1: Deep Extended Catalog of Compact Binary Coalescences Observed by LIGO and Virgo During the First Half of the Third Observing Run," 8 2021.

[99] T. Helfer, D. J. E. Marsh, K. Clough, M. Fairbairn, E. A. Lim, and R. Becerril, "Black hole formation from axion stars," *JCAP*, vol. 03, p. 055, 2017.

[100] F. Michel and I. G. Moss, "Relativistic collapse of axion stars," *Phys. Lett. B*, vol. 785, pp. 9–13, 2018.

[101] J. Y. Widdicombe, T. Helfer, D. J. E. Marsh, and E. A. Lim, "Formation of relativistic axion stars," *JCAP*, vol. 10, p. 005, 2018.

[102] C. Llinares, D. F. Mota, and H. A. Winther, "ISIS: a new N-body cosmological code with scalar fields based on RAMSES. Code presentation and application to the shapes of clusters," *Astron. Astrophys.*, vol. 562, p. A78, 2014.

[103] H. A. Winther and P. G. Ferreira, "Fast route to nonlinear clustering statistics in modified gravity theories," *Phys. Rev. D*, vol. 91, no. 12, p. 123507, 2015.

[104] H. A. Winther *et al.*, "Modified gravity N-body code comparison project," *Mon. Not. Roy. Astron. Soc.*, vol. 454, no. 4, pp. 4208–4234, 2015.

[105] S. Bose, B. Li, A. Barreira, J.-h. He, W. A. Hellwing, K. Koyama, C. Llinares, and G.-B. Zhao, "Speeding up N-body simulations of modified gravity: Chameleon screening models," *JCAP*, vol. 02, p. 050, 2017.

[106] C. Llinares, "Simulation techniques for modified gravity," *Int. J. Mod. Phys. D*, vol. 27, no. 15, p. 1848003, 2018.

[107] C. Arnold and B. Li, "Simulating galaxy formation in $f(R)$ modified gravity: Matter, halo, and galaxy-statistics," *Mon. Not. Roy. Astron. Soc.*, vol. 490, no. 2, pp. 2507–2520, 2019.

[108] A.-C. Davis, R. Gregory, R. Jha, and J. Muir, "Astrophysical black holes in screened modified gravity," *JCAP*, vol. 08, p. 033, 2014.

[109] A.-C. Davis, R. Gregory, and R. Jha, "Black hole accretion discs and screened scalar hair," *JCAP*, vol. 10, p. 024, 2016.

[110] L. K. Wong, A.-C. Davis, and R. Gregory, "Effective field theory for black holes with induced scalar charges," *Phys. Rev.*, vol. D100, no. 2, p. 024010, 2019.

[111] M. Lagos and H. Zhu, "Gravitational couplings in chameleon models," *JCAP*, vol. 06, p. 061, 2020.

[112] P. Brax and M. Pitschmann, "Exact solutions to nonlinear symmetron theory: One- and two-mirror systems," *Phys. Rev.*, vol. D97, no. 6, p. 064015, 2018.

[113] M. Pitschmann, "Exact solutions to nonlinear symmetron theory: One- and two-mirror systems. II.," *Phys. Rev. D*, vol. 103, p. 084013, Apr. 2021.

[114] M. Pernot-Borràs, J. Bergé, P. Brax, and J.-P. Uzan, "Fifth force induced by a chameleon field on nested cylinders," *Phys. Rev. D*, vol. 101, no. 12, p. 124056, 2020.

[115] A. Vilenkin and E. P. S. Shellard, *Cosmic Strings and Other Topological Defects*. Cambridge University Press, 2000.

[116] G. H. Derrick, "Comments on nonlinear wave equations as models for elementary particles," *J. Math. Phys.*, vol. 5, pp. 1252–1254, 1964.

[117] W. D. Goldberger and M. B. Wise, "Renormalization group flows for brane couplings," *Phys. Rev.*, vol. D65, p. 025011, 2002.

[118] C. de Rham, "The effective field theory of codimension-two branes," *JHEP*, vol. 01, p. 060, 2008.

[119] C. Burrage, B. Elder, P. Millington, D. Saadeh, and B. Thrussell, "Fifth-force screening around extremely compact sources," *JCAP*, vol. 08, p. 052, 2021.

[120] J. Braden, C. Burrage, B. Elder, and D. Saadeh, "φenics: Vainshtein screening with the finite element method," *JCAP*, vol. 2021, p. 010, Mar. 2021.

[121] M. S. Alnæs, J. Blechta, J. Hake, A. Johansson, B. Kehlet, A. Logg, C. Richardson, J. Ring, M. E. Rognes, and G. N. Wells, "The fenics project version 1.5," *Archive of Numerical Software*, vol. 3, no. 100, 2015.

[122] H. P. Langtangen and A. Logg, *Solving PDEs in Python*. Springer, 2017.

[123] A. Logg, K.-A. Mardal, G. N. Wells, *et al.*, *Automated Solution of Differential Equations by the Finite Element Method*. Springer, 2012.

[124] C. Burrage, E. J. Copeland, A. Moss, and J. A. Stevenson, "The shape dependence of chameleon screening," *JCAP*, vol. 1801, no. 01, p. 056, 2018.

[125] A. Kuntz, "Two-body potential of Vainshtein screened theories," *Phys. Rev. D*, vol. 100, no. 2, p. 024024, 2019.

[126] C. Burrage, B. Coltman, A. Padilla, D. Saadeh, and T. Wilson, "Massive Galileons and Vainshtein screening," *JCAP*, vol. 2021, p. 050, Feb. 2021.

[127] H. Langtangen and K. Mardal, *Introduction to Numerical Methods for Variational Problems*. Texts in Computational Science and Engineering, Springer International Publishing, 2019.

[128] C. Burrage, E. J. Copeland, and P. Millington, "Radial acceleration relation from symmetron fifth forces," *Phys. Rev. D*, vol. 95, no. 6, p. 064050, 2017. [Erratum: Phys.Rev.D 95, 129902 (2017)].

[129] C. A. O'Hare and C. Burrage, "Stellar kinematics from the symmetron fifth force in the Milky Way disk," *Phys. Rev. D*, vol. 98, no. 6, p. 064019, 2018.

[130] C. Burrage, E. J. Copeland, C. Käding, and P. Millington, "Symmetron scalar fields: Modified gravity, dark matter, or both?," *Phys. Rev. D*, vol. 99, no. 4, p. 043539, 2019.

[131] E. J. Weinberg, *Classical Solutions in Quantum Field Theory: Solitons and Instantons in High Energy Physics*. Cambridge: Cambridge University Press, 2012.

[132] B. Garbrecht and P. Millington, "Self-consistent solitons for vacuum decay in radiatively generated potentials," *Phys. Rev. D*, vol. 92, p. 125022, 2015.

[133] B. Garbrecht and P. Millington, "Fluctuations about the Fubini-Lipatov instanton for false vacuum decay in classically scale invariant models," *Phys. Rev. D*, vol. 98, no. 1, p. 016001, 2018.